MARKOV CHAIN STOCHASTIC SEISMIC INVERSION FOR ROCK PROPERTIES ESTIMATION

A Dissertation Presented to

The Faculty of the Department Earth and Atmospheric Sciences

University of Houston

In Partial Fulfillment

of the Requirements for the Degree

Doctor of Philosophy

By

Carlos Cobos

December 2014

MARKOV CHAIN STOCHASTIC SEISMIC INVERSION FOR

ROCK PROPERTIES ESTIMATION

_____

Carlos Cobos

APPROVED:

_____

Dr. John Castagna, Chairman

_____

Dr. Evgeny M. Chesnokov, Member

_____

Dr. Aibing Li, Member

_____

Dr. Franklin Ruiz, Member

_____

Dean, College of Natural Sciences and Mathematics

ACKNOWLEDGMENTS

I would like to express my gratitude to John Castagna for being an outstanding advisor, who has provided assistance, guidance and support. John is much more than an academic advisor; he is truly a “maestro”. I would also like to thank Aibing Li, Evgeny Chesnokov and Franklin Ruiz, for their readiness to serve on my oral exam committee and for their thorough review and constructive comments on my dissertation and for their tremendous help and support to finish it. Special thanks go to Aibing Li for her help and guidance as graduate student advisor in Geophysics.

I want to thank Sylvia Marshal for her patience and help in all these great years. I am also very grateful to Anne Decour and Hua-wei Zhou; without their support I would not have been able to complete this dissertation.

I have enjoyed and learned from many discussions with Igor Escobar, Ezequiel Gonzalez, Andres Mantilla, Per Avseth, Mario Gutierrez, Isao Takahashi, Manuel Gonzalez and Marcelo Benabentos. I am also very grateful to Tapan Mukerji and De-Hua Han; I cannot thank them enough for all the support they have given me all these years.

I have been fortunate to share my personal time with a number of great friends. Among them the most memorable are Carlos Moreno, Javier Villegas, Tony De Lilla, Maria Villegas, Alexandra Marquez, Carlos Lopez, Karen Romero,

Laszlo Benkovics, Ana Paredes, Freddy Obregon Roberto Varade and Noemi Ordonez.

I have infinite gratitude to my parents Gracia and Carlos, my grandfather Carlos Eduardo, my siblings, Gracia, Carlos Jose, Ligia and Francisco Jesus, and the rest of my family for their continued trust and support.

Finally, I dedicate this dissertation to my wife Carmen and my children Alejandra, Carla and Carlos Eduardo. They have been the energy and motivation that made possible the culmination of my Ph.D.

MARKOV CHAIN STOCHASTIC SEISMIC INVERSION FOR ROCK PROPERTIES ESTIMATION

An Abstract Dissertation

Presented to

The Faculty of the Department Earth and Atmospheric Sciences

University of Houston

In Partial Fulfillment

of the Requirements for the Degree

Doctor of Philosophy

By

Carlos Cobos

December 2014

ABSTRACT

Our purpose is to introduce a stochastic seismic inversion algorithm based on the Markov Chain Monte Carlo Simulation. Conventional inversion algorithms generate elastic properties instead of the key rock properties needed to reliably characterize the hydrocarbon potential of a given subsurface interval. In contrast, the inversion scheme presented here generates a set of possible combinations of rock properties that can explain seismic amplitude responses in terms of lithology, pore structure and fluid variations. The result of the probabilistic seismic inversion is a seismic lithofacies catalog that can describe the elastic response of the studied subsurface interval. The main advantage of this technique is that the results consist of many equally probable rock property models as an alternative to multiple elastic property scenarios. Therefore, no *post facto* elastic-to-rock-properties conversion is needed. The method might be used either in exploratory areas or hydrocarbon field development. In exploratory areas, the stochastic rock physics inversion can support the evaluation for hydrocarbon potential considering the effects of reservoir properties on seismic signatures for different geologic scenarios and physical conditions, with the prime goal of minimizing uncertainties and risk. In field development areas, stochastic seismic inversion produces multiple equally probable rock property models that can explain the real 3D seismic response; it can be used to constrain possible reservoir models used for hydrocarbon reserve estimation and reservoir production simulation. The probabilistic inversion algorithm was successfully tested on a set of real seismic

and well-log data to demonstrate the feasibility of the estimation of critical rock properties for hydrocarbon exploration, such as total porosity and reservoir fraction. The real-data test results confirmed the capability of the proposed inversion technique to accurately predict the rock properties of reservoir seismic lithofacies, even for seismically thin layers.

CONTENTS

Acknowledgments....iii
Abstract....vi
List of Tables x
List of Figures xi
1. Introduction 1
1.1. Motivation 1
1.2. Chapter Layout 4
2. Markov Chain Monte Carlo Simulation 7
2.1. Introduction 7
2.2. Random Variables 7
2.3. Markov Process and Markov Chains 12
2.4. Markov Chain Monte Carlo Methods 16
2.5. Metropolis–Hastings Algorithm 18
3. The Statistical Rock Physics Model 22
3.1. Introduction 22
3.2. Rock Physics Models 22
3.3. Deterministic Versus Statistical Models 24
3.4. Probabilistic Rock Physics Models 25
3.5. The multidimensional Non-Parametric Model 27
3.6. Hybrid Rock Physics Model Example 29
3.7. Using MCMCS to Explore Model Space 36
4. 1D Markov chain stochastic seismic inversion 38
4.1. Introduction 38
4.2. Proposed Inversion Algorithm 39
4.3. Possible Scenario Generation 41
4.4. Synthetic Seismic Generation 44
4.5. The Misfit Function 48
5. Synthetic Examples 51
5.1. Introduction 51

5.2. Synthetic Test 1: Cemented Sand 52
5.3. Synthetic Test 2: High Porosity Sands 66
5.4. Conclusions 77
6. 1D Real Data Application 79
6.1. Introduction 79
6.2. Seismic Data Conditioning 81
6.3. The Model Space Generation 83
6.4. The Seismic Stochastic Inversion 85
6.5. Analysis 90
6.6. Conclusions 95
7. 3D Real Data Application 96
7.1. Introduction 96
7.2. The Kriging Estimator 96
7.3. 3D Real Data Application 99
7.4. Convergence Criteria 109
7.5. Algorithm Efficiency 111
6.7. Conclusions 112
References 113

LIST OF TABLES

Table 2.1: Probability associated to the possible outcomes of random process… 9

Table 2.2: Cumulative probability associated to the possible outcomes of the RV *X*. 10

Table 2.3: Markov chain for initial price variation “same”..... 15

Table 2.4: Markov chain for initial price variation “decrease”..... 16

Table 3.1: Vp statistical summary table for seismic lithofacies A and B. 27

Table 3.2: Fluid properties generated using Batzle and Wang (1992) fluid properties empirical relations..... 32

Table 4.1: Example of the Fisher and Yates shuffle algorithm. The permuted interval ranges from 1 to 5. The red cells correspond to the number that is selected in each iteration..... 43

Table 5.1: Comparison between the synthetic data and the depths obtained by the inversion. 75

Table 6.1: Comparison between the real and the estimated lithology top values for probability larger than 0.2..... 91

Table 6.2: Comparison between the real and the estimated fluid contact depths. 93

LIST OF FIGURES

Figure 2.1: Probability density function of the discrete random variable described in Table 2.1. 9

Figure 2.2: Cumulative probability density function of the RV described in Table 2.2. 11

Figure 2.3: Schematic representation of the transition probability matrix. 15

Figure 2.4: Markov Chain evolution after 500, 1,000, 5,000, 10,000, 25,000 and 50,000 steps. The equilibrium distribution is a Gaussian with zero mean and variance of one. 18

Figure 2.5: Two-dimensional RW with 10,000 points. 19

Figure 3.1: Deterministic (left) versus stochastic models (right). The stochastic model generates a set of possible values instead of a simple outcome. 25

Figure 3.2: P-wave velocity histograms for two different lithofacies. 26

Figure 3.3: Three-dimensional projections of a ten-dimensional Gaussian PDF sampled with 1,000 (upper left), 10,000 (upper right), 100,000 (lower left) and 1,000,000 (lower right). 29

Figure 3.4: 2D Projections of the multivariate probability distribution function. A) Bivariate P-wave velocity versus S-wave velocity PDF; B) Bivariate P-wave velocity versus bulk density PDF; C) Bivariate S-wave velocity versus bulk density PDF; and D) Bivariate Porosity versus bulk density PDF. 31

Figure 3.5: 2D Projections of the modeled multivariate probability distribution function. A) Bivariate P-wave velocity versus Vs PDF; B) Bivariate P-wave velocity versus bulk density PDF; C) Bivariate S-wave velocity versus bulk density PDF; and D) Bivariate Porosity versus bulk density PDF. 33

Figure 3.6: Elastic properties comparison between original saturation (left) and gas replaced saturation (right). 34

Figure 3.7: Example of theoretical rock physics models application to measured P-wave velocity samples. The fluid replacement, cement modeling and porosity perturbation effects are shown by red, green and black arrows. 35

Figure 3.8: Example of theoretical rock physics models application to measured P-wave velocity samples. The probability distribution functions for the fluid replacement, cement modeling and porosity perturbation effects are in red, green and black, respectively. 35

Figure 3.9: Comparison of an original bivariate distribution (left) and the MCMCS distribution (right). 37

Figure 3.10: Mean square error plot for the MCMCS of the example shown in Figure 3.9. 37

Figure 4.1: The inverse and forward problems are complementary mathematical problems. 38

Figure 4.2: Simplified 1D stochastic inversion workflow. 41

Figure 4.3: Schematic representation of the possible scenario generation. 43

Figure 4.4: Comparison among the depth, time and regularized time 1-D P-wave velocity arrays. The black circles show how the regularization in the time domain can affect the elastic properties of the modeled subsurface. 46

Figure 4.5: Schematic representation of the synthetic traces generation algorithm. 48

Figure 4.6: Misfit calculation example. In this synthetic example the cumulative L^2-norm shows the intervals with larger misfit. 49

Figure 5.1: Model 1 synthetic well logs showing (from left to right) facies indicator, shale volume, P-wave velocity, bulk density, S-wave velocity, porosity, P-wave impedance and S-wave impedance. 52

Figure 5.2: Synthetic model 1 pore fluids velocity and density profiles. 54

Figure 5.3: Final seismic lithofacies multivariate PDF projections for the Vp-Vs (Upper), Vp-Rhob (Center), and PhiT-Vp (Lower) spaces. Green, blue, brown and red contours denote shales, brine sands, oil sands and gas sands, correspondingly. Some empirical models are plotted for comparison including Castagna's mudrock line, Castagna's 1993, Han's 1986, Gardner's sand, Gardner's shale, Voigt bound, Reuss bound and Nu's modified Voigt bound for quartz mixture. 55

Figure 5.4: Model 1 angle dependent reflectivity profiles. 56

Figure 5.5: Ricker wavelet with a central frequency of 25 Hz. 57

Figure 5.6: Synthetic angle gather generated from the synthetic model 1. 57

Figure 5.7: 2D Projections of the multivariate probability distribution function for sands (left) and shales (right) calculated from the synthetic model 1. 58

Figure 5.8: Real seismic trace (left) and possible models traces (right) comparison. The selected traces have L^2-norms smaller than 0.9. 59

Figure 5.9: Synthetic versus modeled waveform comparison for four possible models with $\alpha<0.9$. 60

Figure 5.10: Probable models with $\alpha<0.9$. The black, red, yellow and green lines represent the top of upper sand, base of upper sand, top of lower sand and base of lower sand, respectively. 61

Figure 5.11: Sandstone fraction for probable models with $\alpha< 0.9$ 62

Figure 5.12: Total porosity of the probable models with α<0.9. The black, red, yellow and green lines represent the top of upper sand, base of upper sand, top of lower sand and base of lower sand, respectively. 63

Figure 5.13: Volume of shale probable models with α<0.9. The black, red, yellow and green lines represent the top of upper sand, base of upper sand, top of lower sand and base of lower sand, respectively. 63

Figure 5.14: Effective porosity probable models with α<0.9. The black, red, yellow and green lines represent the top of upper sand, base of upper sand, top of lower sand and base of lower sand, respectively. 64

Figure 5.15: Elastic models with α<0.9. The black, red, yellow and green lines represent the top of upper sand, base of upper sand, top of lower sand and base of lower sand respectively. 64

Figure 5.16: Normalized histograms comparison between the rock properties of the synthetic model and the probable solutions, for sand's shale volume (upper left), sand's total porosity (lower left), shale's shale volume (upper right) and shale's total porosity (lower right). Red and blue bars correspond to synthetic model and solutions, respectively. 65

Figure 5.17: Probable models with α<0.045. The black, red, yellow and green lines represent the top of upper sand, base of upper sand, top of lower sand and base of lower sand, respectively. 66

Figure 5.18: Model 2 synthetic well logs showing (from left to right) facie indicator, shale volume, porosity, P-wave velocity, bulk density and S-wave velocity. Black, blue and red lines correspond to *in situ*, brine and gas saturations. 68

Figure 5.19: Synthetic model 2 pore fluids velocity (left) and density profiles (right). Blue and red lines correspond to brine and gas, respectively. 68

Figure 5.20: Final seismic lithofacies multivariate PDF projections for the Vp-Vs (Upper), Vp-Rhob (Center), and PhiT-Vp (Lower) spaces. Grey, blue, and red contours denote shales, brine sands and gas sands, correspondingly. Some empirical models are plotted for comparison, including Castagna's Mudrock line, Castagna's 1993, Han's 1986, Gardner's sand, Gardner's shale, Voigt bound, Reuss bound and Nu's modified Voigt bound for quartz mixture. 69

Figure 5.21: Model 2 angle-dependent reflectivity profiles. 70

Figure 5.22: Synthetic angle gather generated from synthetic model 2. 71

Figure 5.23: 2D Projections of the multivariate probability distribution function for gas sands (left), shales (center) and brine sands (right), calculated from synthetic model 2. 71

Figure 5.24: Real seismic trace (left) and possible models traces (right) comparison. The selected traces have L^2-norms smaller than 0.88. 72

Figure 5.25: Synthetic versus modeled waveform comparison for four possible models with α<0.88. 73

Figure 5.26: Probable models with α<0.88. The green, black and white represent the shales, gas sands and brine sandstone seismic lithofacies, respectively. 74

Figure 5.27: Depth of top of the sand (left), gas-water contact (center) and base of the sand (right) histograms. 74

Figure 5.28: Total porosity of the probable models with α<0.88. 75

Figure 5.29: Volume of shale probable models with α<0.88. 76

Figure 5.30: Effective porosity probable models with α<0.88 calculated from the total porosity and shale volume properties. 76

Figure 5.31: Elastic models with α<0.88. 77

Figure 6.1: Well 1 logs for *in situ* saturation. 80

Figure 6.2: Near angle stack; the top of the upper and lower sands are located at 72 ms and 104 ms, respectively. 80

Figure 6.3: Angle gather at the Well-1 location (Upper). The amplitude extraction at the top of the upper sand shows a strong AVO effect (Lower). 81

Figure 6.4: Well logs converted to time showing the well to seismic tie (right track); the black line corresponds to the measured seismic trace and blue the synthetic seismogram. 82

Figure 6.5: Angle-dependent extracted wavelets. 83

Figure 6.6: Well 1 logs after fluid substitution. Black, red and blue lines correspond to *in situ*, 90% gas and 100% brine-saturated sands. 84

Figure 6.7: 2D Projections of the multivariate probability distribution function generated from Well 1 log data and Gassmann fluid substitution. 84

Figure 6.8: Comparison between real angle traces (upper and lower left) and the 320 solutions for 0° (upper right) and 32° (lower right) incident angles. 86

Figure 6.9: Probable models with α≤0.88. Grey, black and white represent shales, gas sands and low saturation gas sands, respectively. 87

Figure 6.10: Total porosity of the 320 probable models. 88

Figure 6.11: Volume of shale of the 320 probable models. 88

Figure 6.12: Effective porosity of the 320 probable models. 89

Figure 6.13: Possible elastic models with α≤0.88. 89

Figure 6.14: Probability of sand vertical plot. 91

Figure 6.15: Total porosity and effective porosity comparison. The black lines correspond to the well log information and the blue lines to the inverted rock properties. 92

Figure 6.16: Most expected fluid seismic lithofacies (left) and probability of fluid type (right). 93

Figure 6.17: Comparison between the most expected elastic models (blue line) against well logs (black lines). 94

Figure 7.1: Simplified 3D stochastic inversion workflow. 100

Figure 7.2: Anisotropic semivariogram model with a 0.1 nugget, a sill of 0.9 and ranges of 500 meters and 50 meters. 100

Figure 7.3: Variance model evolution for one of the stochastic simulation outcomes. 102

Figure 7.4: Three possible stochastic models. Shales are represented by facies 1, gas sands by facies 2, LSGS by facies 3 and brine sands by facies 4. 102

Figure 7.5: Three possible stochastic total porosity models. 103

Figure 7.6: Three possible stochastic volume of shale models. 103

Figure 7.7: Three possible stochastic P-wave impedance models. 104

Figure 7.8: Three possible stochastic bulk density models. 104

Figure 7.9: Three possible stochastic S-wave velocity models. 105

Figure 7.10: Most expected total porosity model generated from 400 stochastic models. 106

Figure 7.11: Most expected volume of shale model generated from 400 stochastic models. 107

Figure 7.12: Most expected volume of P-wave velocity generated from 400 stochastic models. 107

Figure 7.13: Most expected volume of density generated from 400 stochastic models. 108

Figure 7.14: Most expected volume of S-wave velocity generated from 400 stochastic models. 108

Figure 7.15: Models randomly selected from the real dataset inversion. 109

Figure 7.16: Comparison between real angle trace (right) and 150,000 solutions (left) randomly selected from the five million realizations performed for the real example inversion 110

Figure 7.17: Algorithm efficiency, the proposed algorithm increase linearly with the number of tested models. 111

1. INTRODUCTION

1.1. Motivation

Conventional seismic reservoir characterization (SRC) techniques were developed more than forty years ago for exploration plays where hydrocarbon seismic responses were relatively easy to identify. Early reservoir characterization workflows were usually based on direct hydrocarbon indicator (DHI) identification techniques centered on poststack seismic amplitude analysis and amplitude versus offset (AVO) inversion. DHIs plays are usually related to shallow high porosity reservoirs with significantly lower acoustic impedance compared to the surrounding rocks. The associated seismic signatures of these hydrocarbon-filled high porosity reservoirs can be anomalous high amplitude reflections called “bright spots”.

Nowadays, conventional seismic-reservoir-characterization techniques are becoming obsolete, since the oil industry is moving to explore areas in which the hydrocarbons are located in deeper and more-complex reservoirs. These new hydrocarbon plays are characterized by low-porosity and low-permeability reservoirs with nearly undetectable pore fluid response. This means that the future seismic-reservoir characterization goal is to predict rock properties, such as the porosity, lithology and rock fabric of compacted and cemented porous rock.

The second-most important SRC challenge is to improve seismic vertical resolution. Currently, seismic inversion resolution is still low in new exploration/development challenges and the improvement of seismic derived elastic parameters is paramount for the application of reservoir properties prediction. Techniques such as stochastic inversion have been initially developed in an attempt to obtain from seismic data quantitative information about subsurface rock properties on a very detailed scale.

The main limitation of current seismic-inversion algorithms is that the solutions are usually limited to the acoustic (P-wave impedance) or elastic (P-wave impedance, S-wave impedance, and bulk density) properties of the studied subsurface intervals. However, these properties are not directly useful for characterizing hydrocarbon potential. To accurately characterize the oil potential of a possible of subsurface reservoir, we need to know key rock properties, such as lithology, porosity and fluid type.

The goal of this dissertation is to introduce an inversion technique based on the Markov Chain Monte Carlo Simulation (MCMCS) that can be implemented in a stochastic petrophysical inversion scheme. Our proposed stochastic seismic inversion's objective is to produce a set of probable rock property volumes that can describe the elastic seismic response of the studied interval and its associated uncertainties.

The main advantage of this petrophysical inversion technique is that the results are multiple-probable-rock-property models instead of multiple-elastic-property scenarios. Therefore, no *post facto* elastic-to-rock properties conversion is needed. The method might be used either in exploratory areas or hydrocarbon-field development. In exploratory areas, the proposed stochastic inversion algorithm can support the evaluation for hydrocarbon potential considering the effects of reservoir properties on seismic signatures for different geologic scenarios and physical conditions, with the prime goal of minimizing uncertainties and risk. In field development areas, the stochastic inversion produces many equally probable rock property models that can explain the real 3D seismic response; it can be used to constrain possible reservoir models used for hydrocarbon reserve estimation and reservoir production simulation.

In this dissertation we selected a probabilistic solution to tackle the problem of estimating the physical properties of subsurface rocks based on surface seismic data. According to Tarantola (2005), most probabilistic inverse problems can be resolved using the following equation:

$$\sigma_M(m) = K\rho_M(m)\rho_D(g(m)\,), \tag{1.1}$$

where $\sigma_M(m)$ is the *a posteriori* probability density function in the model space, K is a normalizing constant, $\rho_M(m)$ is the *a priori* probability density function in the model space, $\rho_D(d)$ is the data probability density function and $g(m)$ is the forward modeling operator that relates the model space to the data

space. The operator $g(m)$ is usually non-linear and its role is to predict the values of the observable parameters d that would correspond to a given model m. This theoretical prediction can be described as follows:

$$m \rightarrow d = g(m). \tag{1.2}$$

The main contributions of this dissertation are: 1) the introduction of the Metropolis–Hastings MCMCS algorithm to explore multivariate non-parametric statistical rock physics models; and, 2) the introduction of an inversion technique that directly produces rock property volumes instead of elastic property volumes; hence, the inversion results can be directly introduced into the geological model of the studied area.

1.2. Chapter Layout

Chapter 2 introduces the basis of the Markov Chain Monte Carlo Simulation (MCMCS) and its application to the proposed stochastic inversion. First, we introduce some basic concepts of descriptive statistics. Then we define Markov Chains and their application to Monte Carlo simulations. Finally, it is shown how the Metropolis–Hastings MCMCS algorithm is used to explore the multidimensional solution space in a much more effective way than systematic sampling algorithms.

Chapter 3 focuses on the probabilistic rock physics model used as model space for the proposed inversion scheme. We show how probability density

functions are generated from the integration of the available well and geological data, and are supported by theoretical rock physics models. Second we describe how the MCMCS is used to populate the model space for the proposed stochastic seismic inversion.

Chapter 4 presents our novel 1D stochastic seismic inversion algorithm based on the Metropolis–Hastings MCMCS algorithm. The inversion workflow and its three main steps are explained: the rock properties scenario generation, the synthetic data generation and the comparison between the real and the synthetic traces. We illustrate how the Metropolis–Hastings MCMCS algorithm is used to populate the rock properties of the tested models.

Chapter 5 presents two synthetic examples to illustrate the proposed inversion technique. We show the results of the application of the proposed inversion scheme on two different sets of synthetic data. The synthetic data sets were generated based on real well data, with the goal of testing the inversion in two different geological environments. The first synthetic example represents a geological setting where the sands have larger impedance than that of the surrounded shales. In the second example, we tested the algorithm in a high porosity environment where the fluid property variations have a very strong effect on the elastic properties of the studied reservoirs.

In Chapter 6, we present the first 1D application of the proposed inversion scheme on a real set of data that include seismic and well log information. The

target interval is made up of four seismic lithofacies: shales, gas-filled sands, low saturation gas sands (LSGS) and brine sands. The objective of this inversion is to predict total porosity, volume of shale, effective porosity and fluid type distribution in the studied interval.

Chapter 7 presents the 3D inversion of the real data set introduced in Chapter 6. The 3D algorithm integrates the 1D stochastic inversion procedure with a Kriging engine to produce a lateral constraint rock property model. We analyzed the same data set used in Chapter 6 that corresponds to tertiary marine sediments deposited on a platform margin.

2. MARKOV CHAIN MONTE CARLO SIMULATION

2.1.Introduction

This chapter introduces basic concepts of statistics and the Metropolis–Hastings Monte Carlo Markov Chain Simulation (MCMCS) algorithm. This theoretical introduction is the foundation of the seismic inversion technique based on stochastic simulation proposed in this dissertation. The MCMCS algorithm is used to explore the multidimensional solution space in a much more effective way than systematic sampling algorithms. Its application is especially appropriate in inverse Earth science problems, in which the number of variables tends to be very large. Before introducing the MCMCS algorithm we define some basic statistical concepts in Section 2.2. These basic concepts are random variables, probability density functions, cumulative density functions and the most important descriptive statistical parameters.

2.2. Random Variables

A random variable (RV) is a mathematical variable whose possible values are the numerical outcomes of a random process. According to Papoulis (Papoulis 1984), any function *g(x)* of real variables can be a RV if *g(x)* has the following properties:

a) Its domain must include all the range of RV *x,*

b) The set {*X*<=*x*} is an event for any real number *x,* and

c) The probability of the events $\{X=\pm\infty\}$ must be zero.

Random variables can be discrete or continuous. RVs that are continuous can assume any value within a given range. For instance, if we randomly select several individuals from a population and measure their height, the results can take on any value within a given range, maybe from 2 to 7 feet. In contrast, discrete variables can only assume certain values within a defined range. For example, when we flip a coin and count the possible outcomes, no matter the number of flips, the possible outcomes can only be heads or tails. Because the number of heads or tails results from a random process flipping a coin is a discrete RV.

Random variables are defined by their probability density function (PDF) that describes the likelihood for a given RV to take on a given value. The probability of an RV taking a particular range of values is defined by the integral its PDF taking over the analyzed range.

The following example will illustrate some concepts related to the random variables. Assume an RV X that can only take the values 1, 2, 3, 4 or 5. The probabilities associated with the possible outcomes are shown in Table 2.1.

Table 2.1: Probability associated to the possible outcomes of random process.

Outcome	Probability
1	0.05
2	0.25
3	0.4
4	0.25
5	0.05

The probability that *X* is equal to 1 or 2 is the sum of two probabilities: *P(X = 1* or *X = 2) = P(X = 1) + P(X = 2) = 0.05 + 0.25 = 0.3*. Correspondingly, the probability that *X* is greater than 1 is equal to *1 - P(X = 1) = 1 - 0.05 = 0.95*. The set of possible outcomes and their associated probabilities shown in Table 2.1 are the PDF of the RV *X* (Isaaks and Srivastava, 1989); Figure 2.1 shows the PDF plot of the RV shown in Table 2.1.

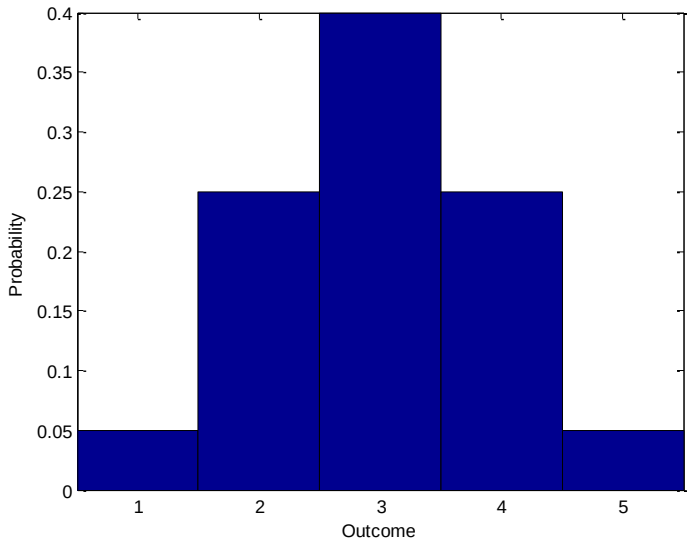

Figure 2.1: Probability density function of the discrete random variable described in Table 2.1.

Suppose the random variable *X* may take *N* different values; the PDF of the discrete RV *X* is then defined as:

$$P(X = xi) = Pi. \tag{2.1}$$

The PDF of a discrete RV must satisfy the following:

a) $0 < Pi < 1$ for each *i*
b) $\sum_{i=1}^{N} Pi = 1.$

By definition, the integral of the PDF (the sum of discrete RVs) is called the cumulative distribution function (CDF). As mentioned, the CDF is defined as the probability that a RV *X* has a value less than or equal to *x*. The CDF of a discrete random variable *X* is related to the PDF by the following expression:

$$CDF\{X\} = \sum_{i=1}^{N} Pi. \tag{2.2}$$

Table 2.2 shows the CDF of the RV X shown in Table 2.1. The CDF of the RV *X* is displayed in Figure 2.2.

Table 2.2: Cumulative probability associated to the possible outcomes of the RV *X*.

Outcome	CDF
1	0.05
2	0.3
3	0.7
4	0.95
5	1

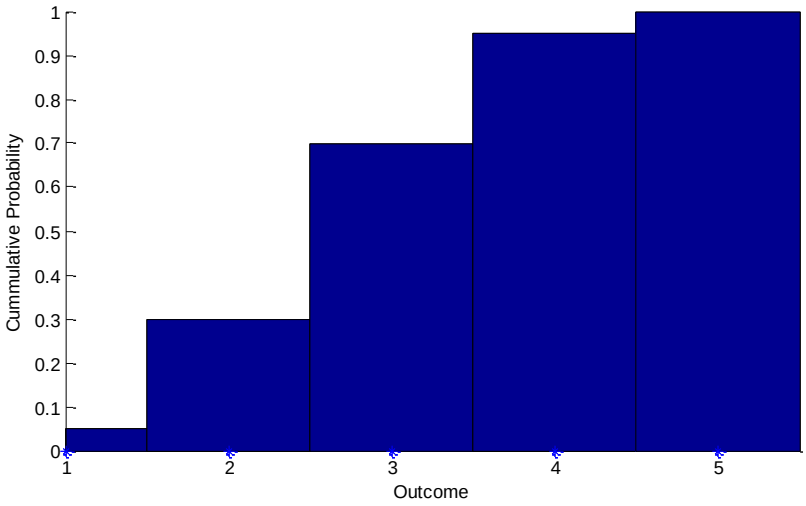

Figure 2.2: Cumulative probability density function of the RV described in Table 2.2.

When the PDF of an RV is known, we can calculate many parameters that are useful to describe the statistics of the analyzed random variable. These parameters include expected value and standard deviation of the RV. The expected value of an RV *X* is defined as the weighted average of all the outcomes; each one is weighted by the probability of occurrence of that outcome:

$$E\{X\} = \sum_{i=1}^{N} Pixi. \tag{2.3}$$

Based on the information shown in Table 2.1 we can calculate the expected value of the RV *X* as:

$$E\{X\} = 1 \times 0.05 + 2 \times 0.25 + 3 \times 0.4 + 4 \times 0.25 + 5 \times 0.05 = 3.$$

Another useful parameter to describe the statistics of a RV *X* is variance. The variance of a RV is a measure of the distance from the outcomes to the

expected value, more commonly known as dispersion. A small variance indicates that the outcomes are very close to the expected value. In contrast, a large variance indicates that the data is very spread out around the mean. Variance can be estimated as:

$$V\{X\} = \sum_{i=1}^{N} Pixi^2 - (\sum_{i=1}^{N} Pixi)^2. \quad (2.4)$$

2.3. Markov Process and Markov Chains

As we introduced in the previous section, a random or stochastic process is a sequence of outcomes that depend on some probability. A Markov process is a stochastic “memory-less” process in which predictions of future outcomes of the stochastic process are based only on its present state. A random variable is defined as a Markov process if the RV has the following properties:

a) The number of possible outcomes or states is finite;
b) The outcome at any stage depends only on the outcome of the previous stage; and
c) The probabilities are constant over time.

Consequently a Markov process can be defined as follows:

$$P(X_{n+1} = x_{n+1} | X_n = x_n, X_{n-1} = x_{n-1}, \dots, X_0 = x_0) = P(X_n = x_n | X_{n-1} = x_{n-1}) \quad (2.5)$$

A sequence of random variables generated by a Markov process is called a Markov Chain. Any Markov Chain is defined by the transition probability to

move from one stage to another. The probability that an RV in state *xi* will change to a state *xj* in a single step is defined as:

$$P(i,j) = P(X_{n+1} = x_i | X_n = x_j). \quad (2.6)$$

The probability that the chain is in state *xi* at step *n* can be calculated using the Chapman-Kolmogorov equation that is the sum of the probability of being in a particular state at the current step and the transition probability from the current state to *xj*:

$$P(X_{n+1} = x_i) = \sum_k P(X_{n+1} = x_i | X_n = x_k) \cdot P(X_n = x_k). \quad (2.7)$$

A more convenient way to express the Chapman-Kolmogorov equation is the matrix form:

$$S(n) = S(0)P^n, \quad (2.8)$$

where *S(n)* is the probability vector at the nth step, *S(0)* is the probability vector at the initial step, and *P* is the probability transition matrix.

A Markov Chain can be illustrated using a simple example. Suppose that the price variation of a particular share in the stock market can be predicted using a Markov process and the possible price states are: “decrease”, “same” or “increase”. Therefore, the price of the share tomorrow only depends on today’s

share price. Assuming that today the price variation is “same”, the transition probability matrix (Figure 2.3) can be written as follows:

$$P = \begin{pmatrix} 0.40 & 0.30 & 0.30 \\ 0.25 & 0.50 & 025 \\ 0.30 & 0.30 & 0.40 \end{pmatrix}.$$

The initial state vector is:

$$S(0) = (0 \quad 1 \quad 0).$$

Tomorrow’s price variation will be:

$$S(1) = (0 \quad 1 \quad 0)\begin{pmatrix} 0.40 & 0.30 & 0.30 \\ 0.25 & 0.50 & 025 \\ 0.30 & 0.30 & 0.40 \end{pmatrix}^{1} = (0.3000 \quad 0.4000 \quad 0.3000).$$

The sixth day’s price variation will be:

$$S(6) = (0 \quad 1 \quad 0)\begin{pmatrix} 0.40 & 0.30 & 0.30 \\ 0.25 & 0.50 & 025 \\ 0.30 & 0.30 & 0.40 \end{pmatrix}^{6} = (0.3125 \;\; 0.3750 \;\; 0.3125).$$

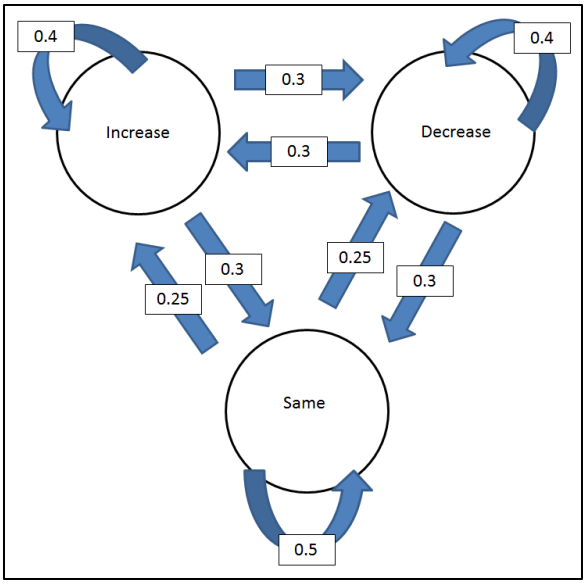

Figure 2.3: Schematic representation of the transition probability matrix.

The summary of the Markov Chain for the first six days is shown in Table 2.3. However, if the initial price variation is “decrease” instead of “same” (see Table 2.4), the Markov Chain reaches the same probability values at the sixth day. Hence, on the sixth day, the Markov Chain reaches its stationary distribution, where the probability values are independent of the initial state.

Table 2.3: Markov chain for initial price variation “same”.

Day	Decrease	Same	Increase
1	0.2500	0.5000	0.2500
2	0.3000	0.4000	0.3000
3	0.3100	0.3800	0.3100
4	0.3120	0.3760	0.3120
5	0.3124	0.3752	0.3124
6	0.3125	0.3750	0.3125

Table 2.4: Markov chain for initial price variation “decrease”.

Day	Decrease	Same	Increase
1	0.4000	0.3000	0.3000
2	0.3250	0.3600	0.3150
3	0.3145	0.3720	0.3135
4	0.3129	0.3744	0.3128
5	0.3126	0.3749	0.3126
6	0.3125	0.3750	0.3125

2.4. Markov Chain Monte Carlo Methods

Monte Carlo Simulation (MCS) methods are a set of computational algorithms used to solve numerical problems based on random numbers. One of the most common applications of MCS is to calculate the probability of a specific outcome by randomly sampling a large number of scenarios. MCS methods have many applications in physics, finance, engineering, and mathematics. In this dissertation we use the MCS to explore the space of possible solutions used in the proposed seismic inversion algorithm.

Markov Chain Monte Carlo (MCMC) is a family of algorithms for sampling desired probability distributions based on Markov processes. The shape of the desired distribution has to be similar to the MCMC equilibrium distribution; this means that the quality of the MCMC distribution improves with the number of steps. A Markov Chain is an ideal method for Monte Carlo simulations due to the

memoreless nature of Markov stochastic processes. This Monte Carlo method combines all the desired features for stochastic simulation:

a) It is simple and easy to construct a Markov Chain with the desired properties;
b) It generates statistically consistent samples from the target distribution; and
c) The samples drawn are dependent and follow a Markovian framework which allows more robust convergence.

Markov Chain mixing time is by definition the number of steps needed to reach the equilibrium with tolerable error. The better the Morkov Chain, the faster the mixing time. Figure 2.4 shows an example of a Markov Chain with a Gaussian as steady distribution; in this example, the desired distribution is reached after 50,000 steps.

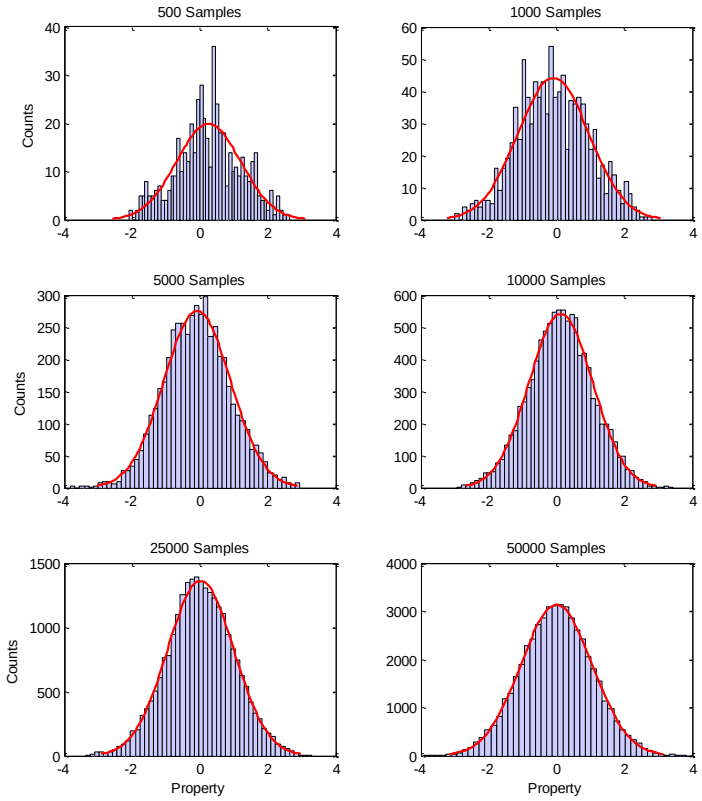

Figure 2.4: Markov Chain evolution after 500, 1,000, 5,000, 10,000, 25,000 and 50,000 steps. The equilibrium distribution is a Gaussian with zero mean and variance of one**.**

2.5. Metropolis–Hastings Algorithm

A random walk (RW) is a mathematical stochastic path that is generated from a series of random steps. RW theory plays an important role in physics, statistics and engineering, since many physical phenomena can be modeled using a stochastic method; coin tosses, Brownian motion and stock prices are examples of processes that can be modeled as RWs. These methods are particularly useful as sampling technique since RW sampling methods are least

biased compared to systematic sampling algorithms. However, RWs can lead to poor representation of the real distribution in very-large-dimension problems.

Figure 2.5 shows a two-dimensional RW with 5,000 steps. In a simple RW, the location can only jump to neighboring sites of the lattice. In a simple symmetric RW on a locally finite lattice (Figure 2.5), the probabilities of the location jumping to each one of its immediate neighbors are the same.

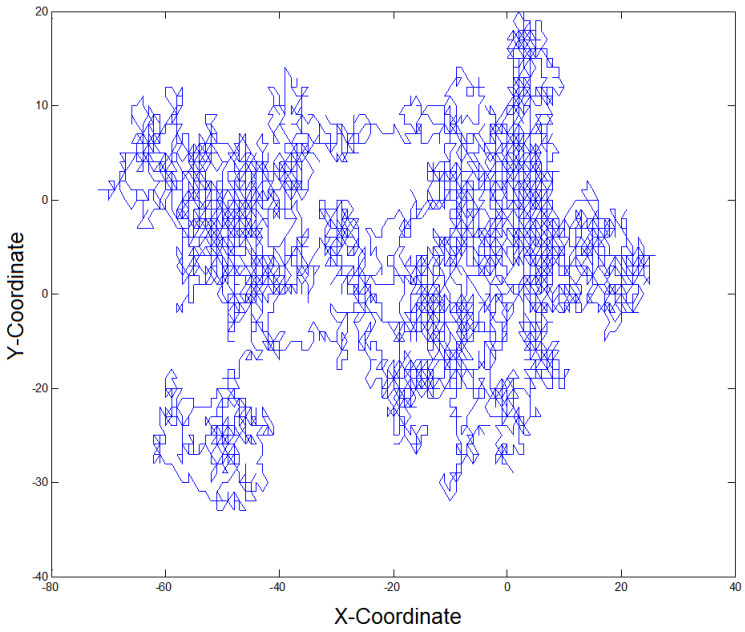

Figure 2.5: Two-dimensional RW with 10,000 points.

RW algorithms are generally based on Markov Chain processes. In this dissertation, we implemented a Markov Chain Monte Carlo method called the Metropolis–Hastings algorithm. The Metropolis–Hastings algorithm was originally introduced in 1953 by a group of scientists (Metropolis *et. al.*, 1953) from Los

Alamos National Laboratory, and extended to its general form by W. K Hasting in 1970 (Hastings, 1970). The idea of the Metropolis–Hastings Monte Carlo algorithm is to compute values of the function *P(x)* that are proportional to a known probability distribution *F(x) P(x)=K*F(x),* where the proportional constant K is unknown and very difficult to estimate. The Metropolis algorithm generates a sequence of draws as follows:

1. Randomly select an initial value x_0 that satisfied the relation $F(X_0)>0$.

2. Using the current value (x_t) draw, generate the candidate value (x_{t+1}) from a proposed transition probabilistic function $q(x_t,x_{t+1})$.

3. From the candidate (x_{t+1}) and the current (x_t) points, calculate the ratio of the density at the candidate and current points:

$$\alpha = \frac{F(x_{t+1})q(x_{t+1}, x_t)}{F(x_t)q(x_t, x_{t+1})}; \tag{2.9}$$

If α≥1 accept the candidate point (x_{t+1}) as current value and return to step 2; otherwise, accept the candidate with probability α, else reject it and return to step 2.

Finally, the Metropolis–Hastings algorithm can be written as follows:

$$\alpha = min\left(\frac{F(x_{t+1})q(x_{t+1}, x_t)}{F(x_t)q(x_t, x_{t+1})}, 1\right). \tag{2.10}$$

As with any MCMC methods, the Metropolis–Hastings algorithm approaches the desired distribution as the number of steps increases. A key issue in the successful implementation of the Metropolis-Hastings or any other MCMC sampler is the number of runs (steps) until the chain approaches stationarity (the length of the burn-in period). Typically, the first 1,000 to 5,000 elements are thrown out, and then one of the various convergence tests is used to assess whether stationarity has indeed been reached.

A poor choice of starting values and/or proposal distribution can greatly increase the required burn-in time, and an area of much current research is whether an optimal starting point and proposal distribution can be found. One suggestion for a starting value is to start the chain as close to the center of the distribution as possible, for example by taking a value close to the distribution's mode. A chain is said to be poorly mixing if it stays in small regions of the parameter space for long periods of time, as opposed to a well-mixed chain that seems to effortlessly explore the space.

3. THE STATISTICAL ROCK PHYSICS MODEL

3.1.Introduction

This chapter introduces the concept of the statistical rock-physics model and illustrates how well-log data and theoretical rock-physics models are used to populate the model space of the proposed seismic-inversion algorithm.

Sedimentary rocks are aggregates of compacted crystalline grains and organic matter that are often amalgamated by cement minerals. The free space between the mineral grains is often called intergranular space or porosity. In *in situ* conditions, the intergranular space is filled by liquid or gaseous fluids. The solid portion of the rock is known as the rock's matrix, or more commonly, "the matrix". The rock's matrix geometry or how the crystalline grains are arranged in a sedimentary rock is usually extremely complex and depends on many variables, such as provenance, sorting, burial history, diagenesis, etc. We need to define an enormous number of parameters to accurately relate the geometry of most sedimentary rocks and their elastic moduli; among these parameters, we have volume fractions of minerals, nature of boding on the grain interface, type and volume fraction of cements, etc. (Ruiz, 2009).

3.2. Rock Physics Models

Rock-physics models are mathematical models that are related to rock properties (e.g., porosity, mineral and cement composition pore geometry, elastic

moduli, etc.). Rock-physics models are used to estimate rock properties that have not been sampled. Most rock-physics models can be classified into three groups: theoretical, empirical, and heuristic (Avseth *et al.*, 2005).

According to Avseth (2005), theoretical models are continuum mechanics approximations of the elastic, viscoelastic, or poroelastic properties of rocks. Biot theory (Biot, 1956) is one of the first to model the coupled mechanical behavior of a porous rock filled with a linearly viscous fluid. At zero frequency, the Biot relations turn into the Gassmann equation (Gassmann, 1951).

Empirical models are based on the statistical regression analysis of experimental observations. Most empirical models are only valid for the specific data sets and physical conditions where the data was measured. Empirical rock physics models are widely used to predict the properties of rock for which measured data is not available. Examples of empirical models are Castagna's mudrock line (Castagna *et. al.*, 1985), Gardner's density relation (Gardner *et. al*, 1974) and Han's Gulf of Mexico relations (Han, 1986).

Heuristic rock-physics models are mathematical relations based on the experience-based techniques for problem solving. Since these models are non-mathematically rigorous, they are not optimal. Popular examples of heuristic models are the Wyllie time-average equation (Wyllie *et. al,.* 1956) and the Greenberg and Castagna relations (Greenberg and Castagna, 1992).

3.3. Deterministic Versus Statistical Models

A deterministic model is a mathematical relation in which outcomes are precisely determined through known relationships among variables. In such models, a given input will always produce the same output. In deterministic models the estimation error is assumed to be zero or negligible. Unfortunately, in Earth science it is impossible to gather the required knowledge to create a deterministic model that accurately relates the physical properties of most sedimentary rocks. In contrast, statistical models generate a set of possible values with their associated probability of occurrence (Figure 3.1). Therefore, theoretical and empirical rock physics models can be considered deterministic and statistical models respectively. While deterministic models rely on the physics of the phenomenon, probabilistic models trust in an adequate statistical sampling of the analyzed set of data. It is important to emphasize that a poor sampling of the data space will lead to the formulation of an inaccurate or incorrect probabilistic model.

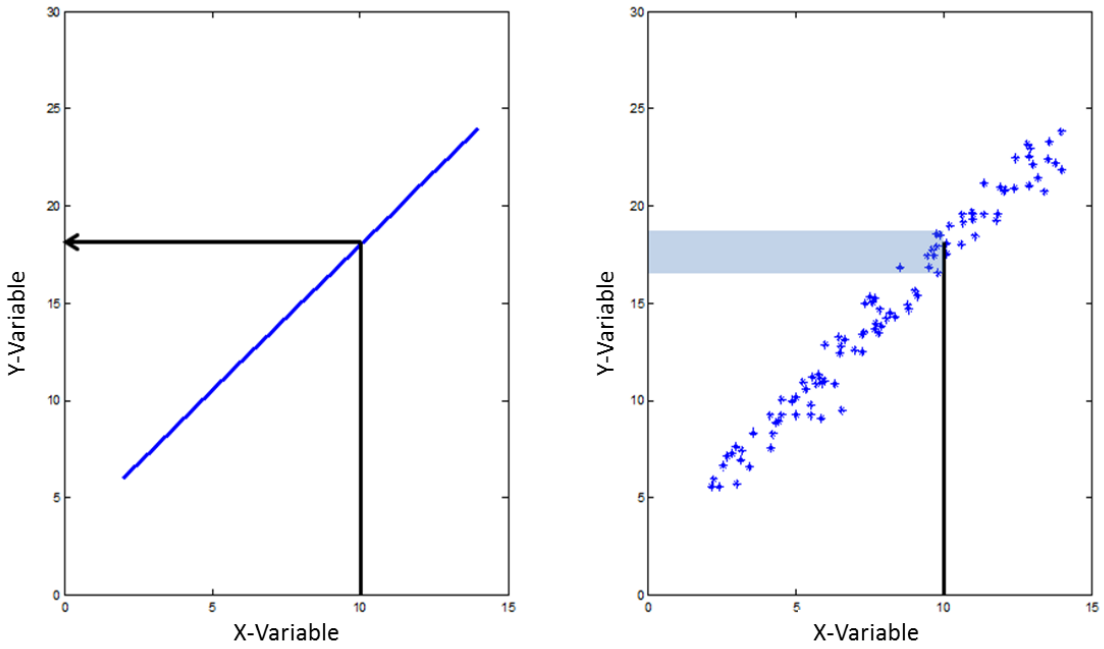

Figure 3.1: Deterministic (left) versus stochastic models (right). The stochastic model generates a set of possible values instead of a simple outcome.

3.4. Probabilistic Rock-Physics Models

Probabilistic rock physics models are physical models that relate the rock properties of a given seismic lithofacies using probabilistic techniques. Avseth (2000) defined a seismic lithofacies as a seismic-scale sedimentary unit that is characterized by its lithology, bedding configuration, petrography and elastic properties. Seismic lithofacies can be used to estimate the statistical parameters of the rocks that constitute the sedimentary unit. Since these rocks have similar depositional and diagenesis history, we can assume the stationarity of the statistics of the rock's properties for any particular seismic lithofacies (Avseth, 2000).

We usually observe data scatter when we plot elastic properties against rock properties for a given seismic lithofacies. Due to data scatter, descriptive statistics are often used to summarize the elastic properties of a given seismic lithofacies. The descriptive statistics is useful to define the most important properties of the statistical populations. Figure 3.2 shows the P-wave velocity histograms of two different lithofacies; the histograms clearly show that lithofacies A has a lower most expecting value and larger velocity dispersion than lithofacies B. Descriptive statistical measurements are normally used to define the tendency of the data (Table 3.1), for example, when most of the data is gathered or gives an idea of the data dispersion.

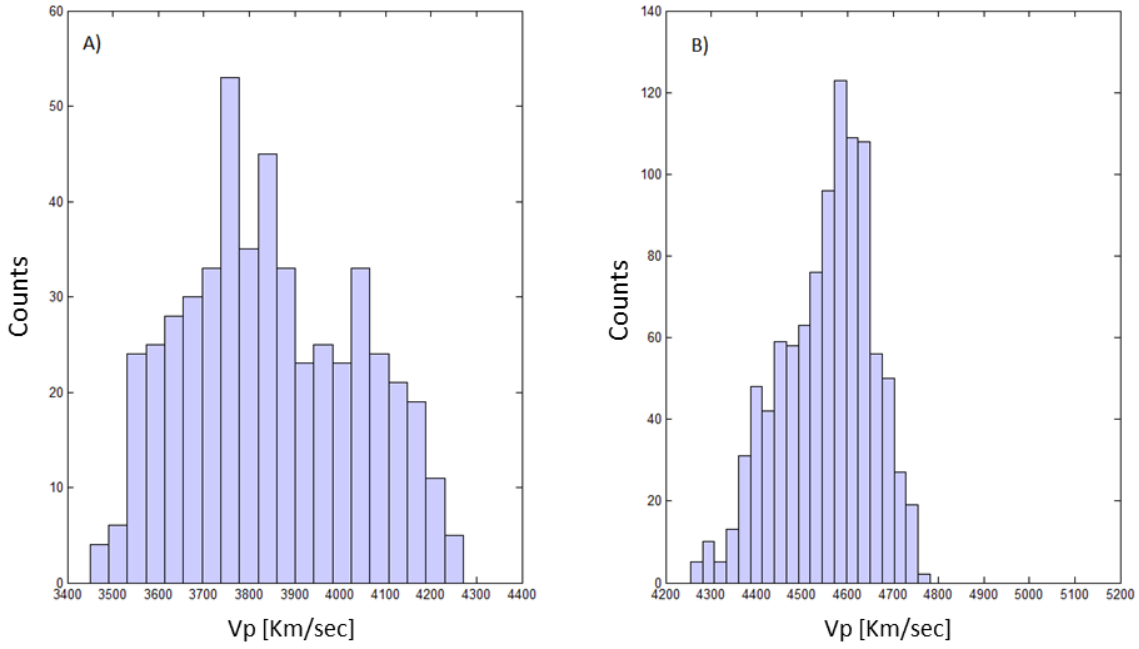

Figure 3.2: P-wave velocity histograms for two different lithofacies.

Table 3.1: Vp statistical summary table for seismic lithofacies A and B.

	Seismic Lithofacies A	Seismic Lithofacies B
Mean	3849.9	4553.2
Median	3831.4	4568.4
Standard Deviation	187.85	100.31
Variance	35288	10063

For most practical applications, descriptive statistics is not enough to represent the complexity of the relations among rock properties, since the definition of central estimators (like the mean or the median) and the dispersion estimators (like the variance and standard deviation) generally do not have clear meaning in multidimensional non-parametric spaces. Hence, to avoid the limitations of descriptive statistics, non-parametric probability density functions (PDFs) are introduced to better describe the dependence among rock properties, including its non-uniqueness and non-linearity (Takahashi, 2000). Usually, PDFs are generated from the integration of the available well and geological data and are supported by theoretical rock physics models. In fact, multivariate PDFs are usually hybrid rock physics models that can describe measured rock samples and scenarios not sampled by measured data.

3.5. The multidimensional Non-Parametric Model

A poorly mixed chain can arise because the target distribution is complex (multi-modal) and our choice of starting values traps the Markov Chain to one of

the modes. An approach to solve this problem is to transform the complex target distribution to a simpler parametric distribution like a Gaussian distribution, and then proceed with the MCMCS. This process is called normal scoring and is commonly used in many statistical applications. Normal scoring processes can be applied to any number of dimensions. However, it is easy to underestimate the sampling (leaving many empty zones) of large-dimensional inverse problems. To solve this issue, the number of samples has to be largely increased with the number of dimensions. Figure 3.3 shows four three-dimensional projections of a ten-dimensional Gaussian distribution sampled with 1,000, 10,000, 100,000 and 1,000,000 draws. We can see that the distribution sampled with 1,000 draws does not represent the shape of the target Gaussian distribution. The modeled distribution approaches the target distribution when the number of samples exceeds 100,000 draws. After the MCMCS is performed, the resulting normal Gaussian distribution is converted back to its original shape, applying reverse normal scoring.

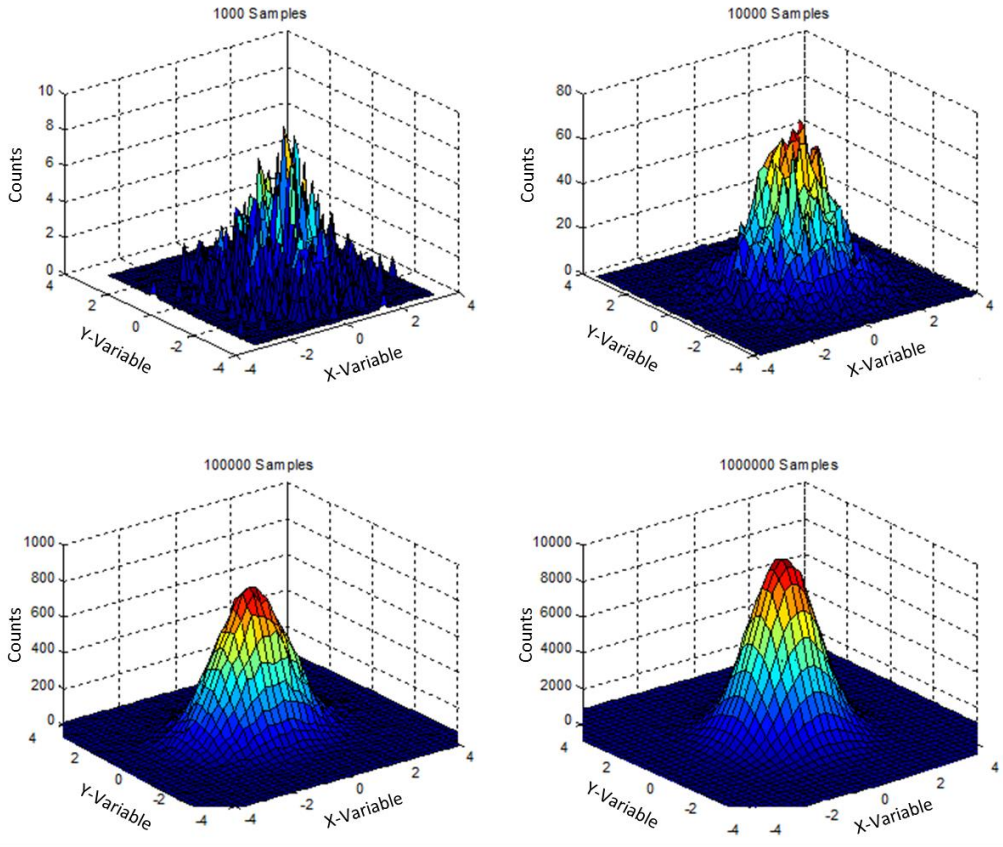

Figure 3.3: Three-dimensional projections of a ten-dimensional Gaussian PDF sampled with 1,000 (upper left), 10,000 (upper right), 100,000 (lower left) and 1,000,000 (lower right).

3.6. Hybrid Rock-Physics Model Example

In hydrocarbon exploratory areas where the availability of well log data is usually limited, rock physics modeling is used to populate the multivariate PDFs with data or seismic lithofacies that are not sampled by the existing wells, but are probable in the studied area (Gonzalez, 2006). An example of a hybrid rock physics model can be made by the application of Gassmann's equation (Gassmann, 1951) to a set of well log data. Gassmann's equation allows us to

estimate the effective bulk modulus of a fluid filled porous rock when the original fluid is replaced by a second fluid. This is a very important problem in hydrocarbon exploration, where fluid replacement is commonly used to sample different fluids and saturations scenarios in potential reservoir rocks. Gassmann's equation is written as follows:

$$\frac{K_{sat}}{K_0 - K_{sat}} = \frac{K_{dry}}{K_0 - K_{dry}} + \frac{K_{fl}}{\emptyset(K_0 - K_{fl})}; \tag{3.1}$$

$$\mu_{sat} = \mu_{dry}, \tag{3.2}$$

where:

K_{sat} = Effective bulk modulus of the rock with pore fluid,

K_{dry} = Effective bulk modulus of the dry rock,

K_0 = Bulk modulus of the pore grain material,

K_{fl} = Effective bulk modulus of the fluid,

$\emptyset$= Porosity,

μ_{sat} = Effective shear modulus of the rock with pore fluid,

μ_{sat} = Effective shear modulus of the dry rock.

Some of the projections of a multivariable probability density function are shown in Figure 3.4. The shown PDF was generated from well log data and it defines the relations among the rock properties for clean sandstone. This sandstone represents a lithofacies whose intergranular space is filled by brine.

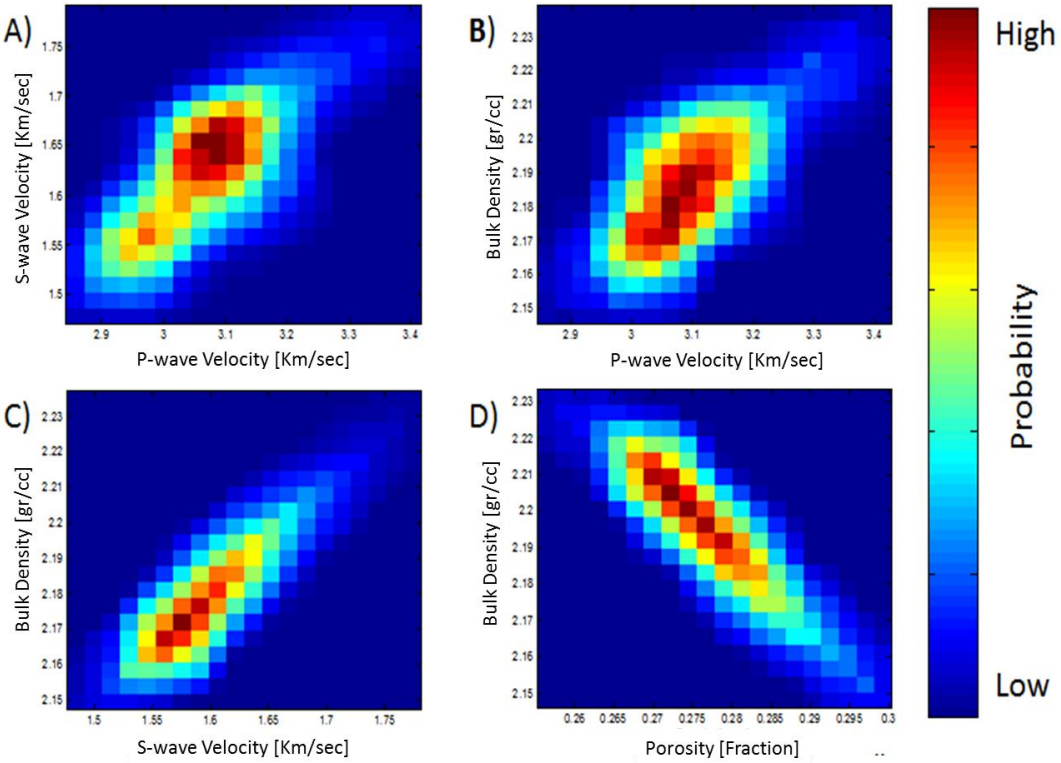

Figure 3.4: 2D Projections of the multivariate probability distribution function. A) Bivariate P-wave velocity versus S-wave velocity PDF; B) Bivariate P-wave velocity versus bulk density PDF; C) Bivariate S-wave velocity versus bulk density PDF; and D) Bivariate Porosity versus bulk density PDF.

We applied the Gassmann relations to predict the sandstone elastic properties when the pores are filled with gas. We estimated the acoustic properties of the brine and gas using the Batzle and Wang empirical model (Batzle and Wang, 1992) and assuming salinity of 15,000 ppm, temperature of 84°C, pore pressure of 25 MPa and gas specific gravity of 0.6. The irreducible water saturation of the modeled sandstone was assumed 8%; hence the fluid properties were calculated for a saturation of 92% gas and 8% brine using the

homogeneous saturation model (Mavko *et al.,* 1998). The fluid properties at the specified temperature and pressure are displayed in Table 3.2.

Table 3.2: Fluid properties generated using Batzle and Wang (1992) fluid properties empirical relations.

	Brine	**Gas**	**90% Gas and 10% Brine**
Bulk Modulus [GPa]	2.59	0.05	0.06
Density [g/cc]	0.99	0.126	0.21
Vp [km/sec]	1.61	0.63	0.53

The three-dimensional projection of the multivariate probability distribution function of the modeled gas saturated sandstone is shown in Figure 3.5. As is expected, the replacement of the original fluid with less dense and more compressible fluid will decrease the density and bulk modulus. In contrast, the S-wave velocity slightly increases due to the density effect on the S-wave velocity expression. The comparison of the elastic properties histograms for the original and fluid replaced sands shows that the fluid substitution introduces more uncertainty in the gas filled rock in comparison with the brine-filled rock (see Figure 3.6). A similar observation was made done by Sengupta (2000) in her sensitivity analysis of fluid replacement.

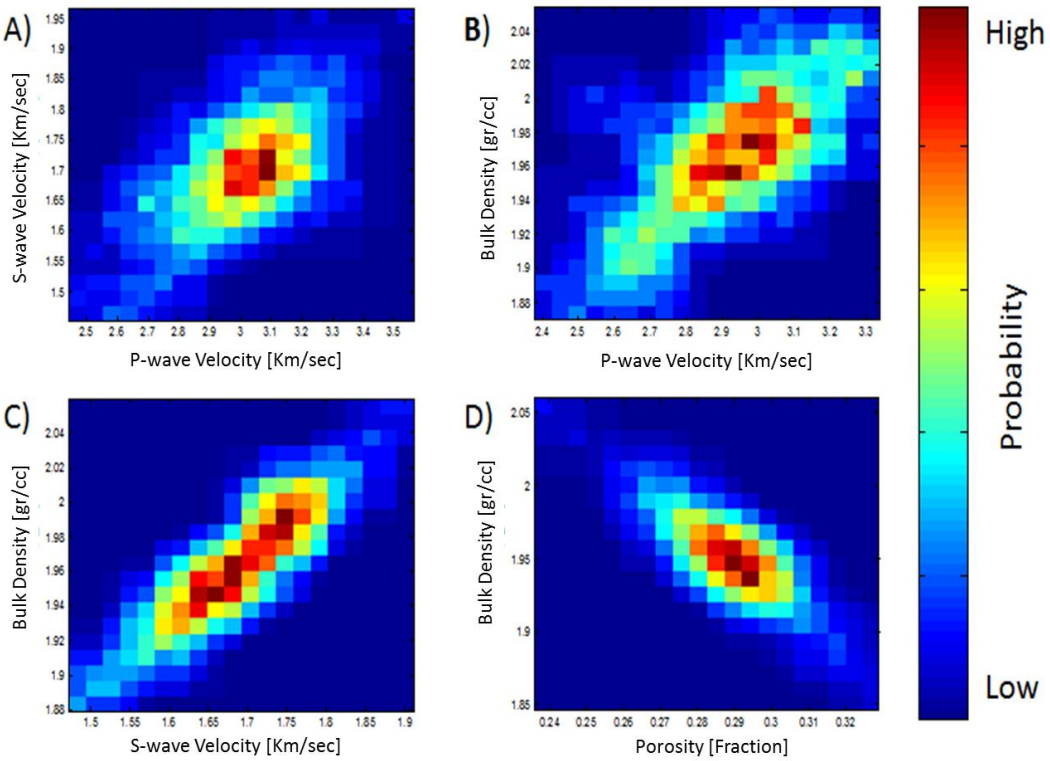

Figure 3.5: 2D Projections of the modeled multivariate probability distribution function. A) Bivariate P-wave velocity versus Vs PDF; B) Bivariate P-wave velocity versus bulk density PDF; C) Bivariate S-wave velocity versus bulk density PDF; and D) Bivariate Porosity versus bulk density PDF.

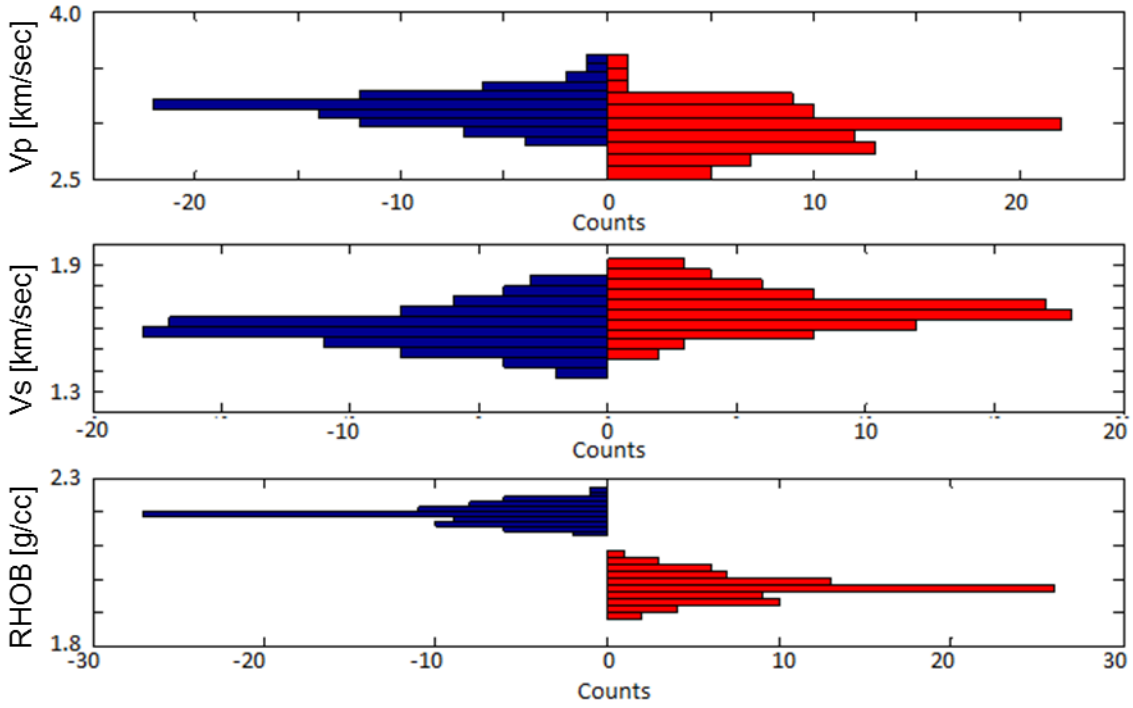

Figure 3.6: Elastic properties comparison between original saturation (left) and gas replaced saturation (right).

This probabilistic rock physics modeling process can include any simple or complex rock physics model as long as the rock property can be defined in the multivariate PDF. For instance, the Dvorkin cemented sand model (Dvorkin and Nur, 1996) can be used to theoretically add cement to sand measurements. Other applications of theoretical rock physics models are shown in Figure 3.7. The effect of fluid replacement, adding cement or reducing porosity over the P-wave velocity (Vp) are displayed in the porosity-Vp space. Figure 3.8 shows the probability functions for the modeled seismic lithofacies.

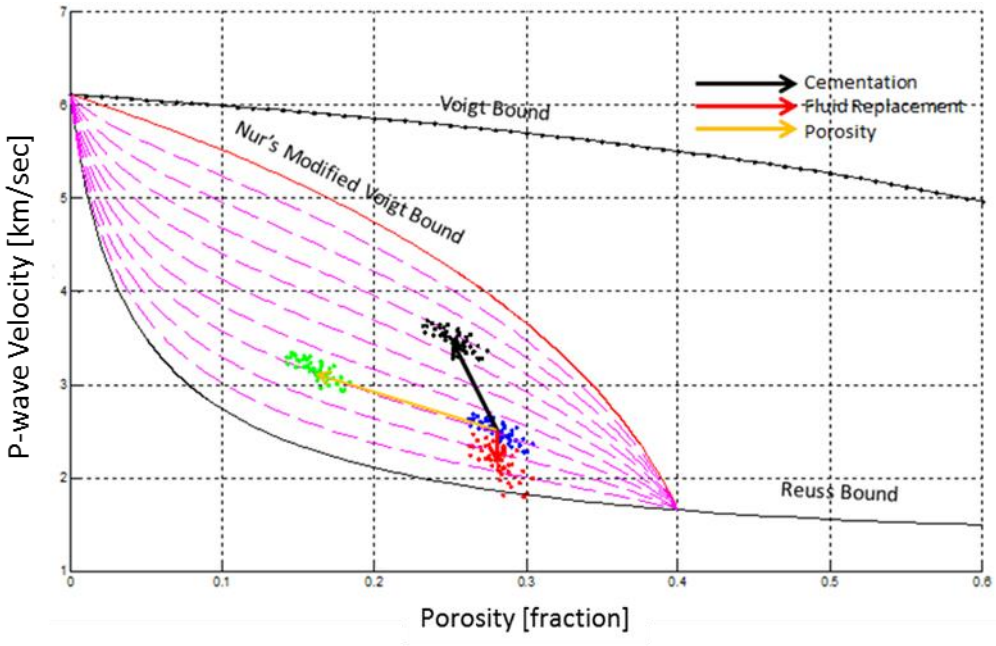

Figure 3.7: Example of theoretical rock physics models application to measured P-wave velocity samples. The fluid replacement, cement modeling and porosity perturbation effects are shown by red, green and black arrows.

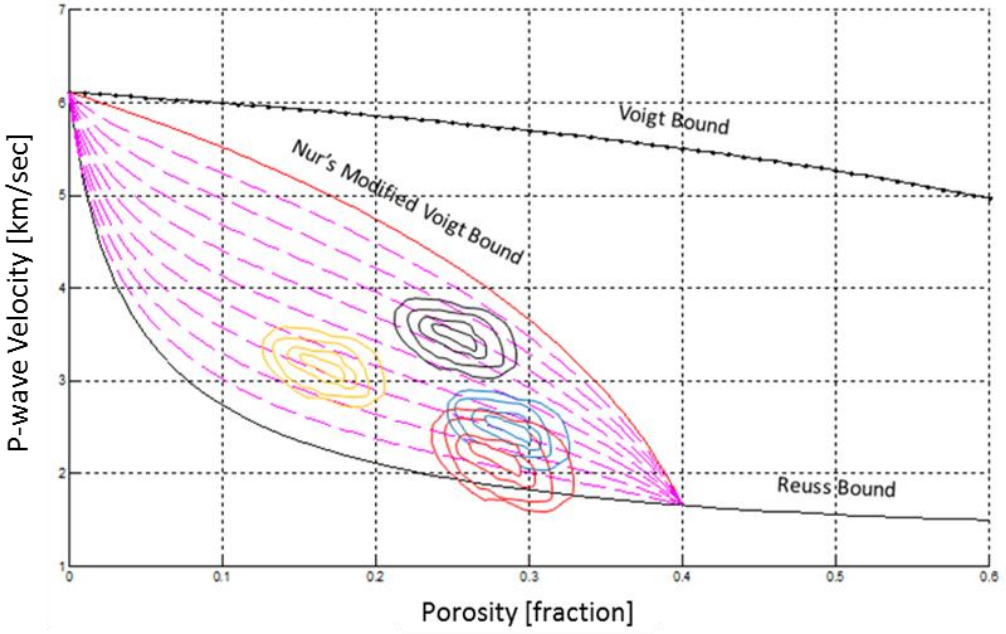

Figure 3.8: Example of theoretical rock physics models application to measured P-wave velocity samples. The probability distribution functions for the fluid replacement, cement modeling and porosity perturbation effects are in red, green and black, respectively.

3.7. Using MCMCS to Explore Model Space

As we have mentioned, our proposed stochastic inversion scheme relies on a Markov Chain Monte Carlo Simulation (MCMCS) engine to explore the model space represented by a non-parametric multivariate probability density function. The use of Monte Carlo simulation is central to the resolution of inverse problems with large-dimensional model spaces for which systematic evaluation of model spaces on a regular grid is not feasible (since the required number of points to evaluate is too large).

When the MCMCS algorithm is well implemented, the shape of the target PDF does not change with the number of simulated samples; this means that the MCMCS is really random and unbiased. An example of the MMCMCS implementation is shown in Figure 3.9. The shape of the simulated distribution is very similar to the original PDF, even though the number of simulated points is more than one hundred times the number of original data points. We use the Mean Squared Error (MSE) between the simulated and target distributions to estimate the optimum number of steps to reach MCMCS equilibrium.

Figure 3.10 shows the MSE plot for the MCMCS example shown in Figure 3.9. For this particular MCMCS implementation the equilibrium is reached after 8,000 steps. The MSE is estimated as follows:

$$MSE = E[(T_D - S_D)^2],$$

Where T_D= Target Distribution and S_D=Simulated Distribution.

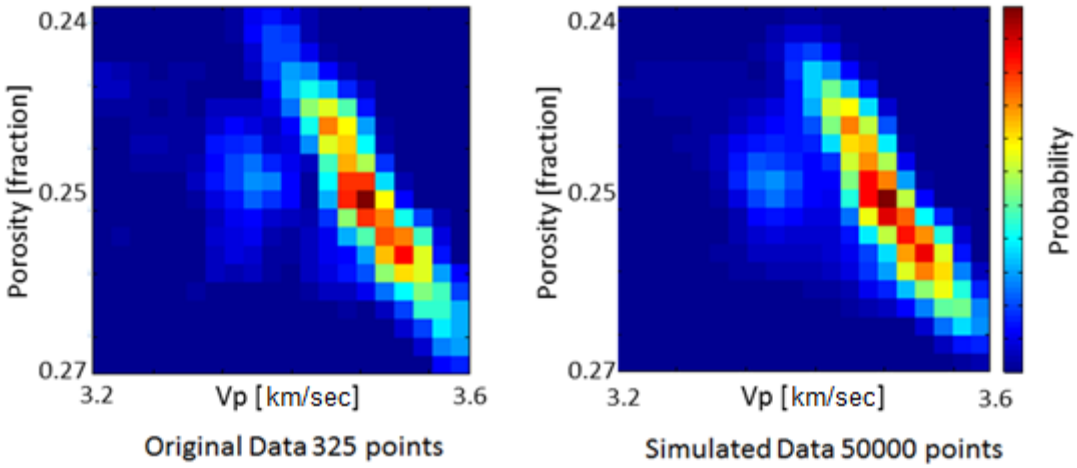

Figure 3.9: Comparison of an original bivariate distribution (left) and the MCMCS distribution (right).

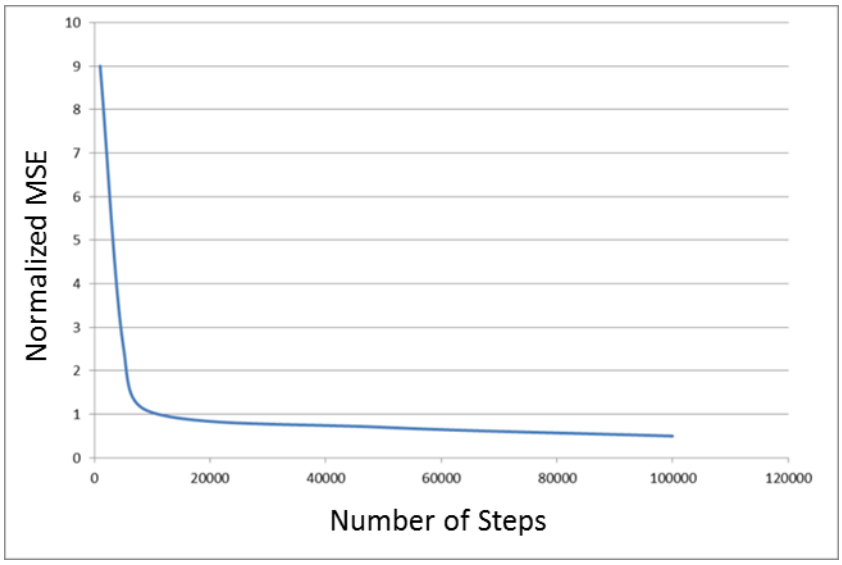

Figure 3.10: Mean-square-error plot for the MCMCS of the example shown in Figure 3.9.

4. 1D MARKOV CHAIN STOCHASTIC SEISMIC INVERSION

4.1. Introduction

This chapter presents the 1D Markov Chain stochastic inversion algorithm. First, it shows the general workflow for the 1D inversion scheme. Second, it describes in detail all the steps of the general 1D workflow.

In physics the *inverse problem* consists of using measurements to infer the parameters that describe a system (Tarantola, 2005). In contrast, the forward problem involves the prediction of the measurements given the parameters that describe the studied system (Figure 4.1). In Earth science the goal of the inverse problem is to estimate the earth's properties from a series of geophysical observations.

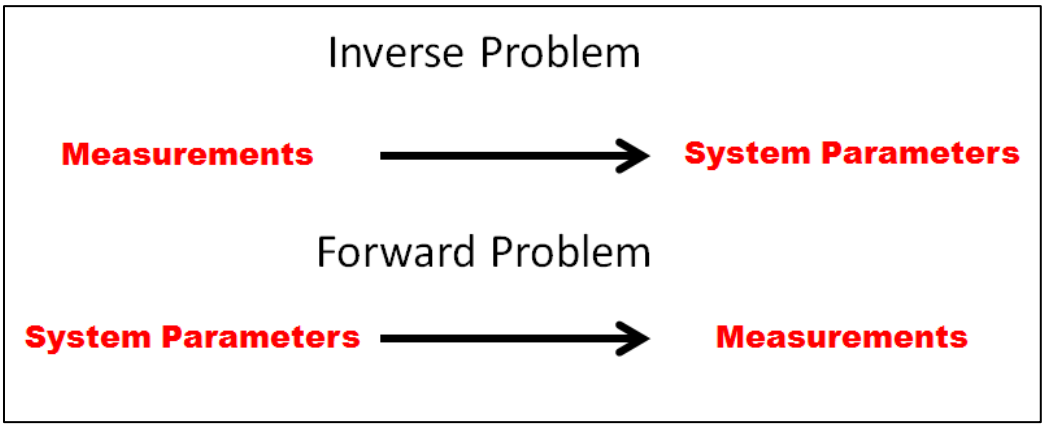

Figure 4.1: The inverse and forward problems are complementary mathematical problems.

The content of this chapter was partially presented in the paper IPTC-18040 of the 2014 International Petroleum Technology Conference in Kuala Lumpur.

This dissertation is focused on the specific problem of estimating the earth's parameters from surface seismic data. As with any inverse problem in earth science, seismic inversion does not have a unique solution. Hence, we proposed a novel inversion scheme that is based on a probabilistic method instead of a deterministic approach. When the inverse problem is solved using a probabilistic approach the system parameters are represented by a PDF generated from the available data and model. The probabilistic theory applied to this dissertation can be applied in any kind of inverse problem, including nonlinear problems. To solve most probabilistic inverse problems, we need to implement an extensive exploration of the system space. Due to the multidimensional nature of the Earth science problems, we cannot perform a systematic system space exploration. Instead, we perform possible solution space exploration using Markov Chain Monte Carlo methods.

4.2. Proposed Inversion Algorithm

The proposed 1D stochastic inversion algorithm is based on a Markov Chain stochastic simulation that uses statistical rock physics to constrain the space of possible solutions. Mukerji *et al.* (2001) introduced the statistical rock-physics methods as a way to combine rock physics, information theory, and geostatistics to reduce uncertainty in reservoir property estimation. Our fundamental contribution is using the Metropolis–Hastings MCMCS algorithm to generate multivariate non-parametric statistical rock physics models and introducing the inversion technique that directly produces rock property volumes

instead of elastic property volumes; using our methods, inversion results can be directly introduced into the geological model of the studied area.

Figure 4.2 shows an idealized scheme for a 1D inversion algorithm. The inversion technique consists of four main steps: the rock properties scenario generation, the synthetic data calculation and the comparison between the real and synthetic traces. In each realization, a model of the subsurface properties is generated, and the model properties are calculated from the previously defined multivariate PDF. After the subsurface model is generated, a synthetic trace is produced using the elastic properties from the subsurface model. Finally, the synthetic trace is compared to the real seismic trace; if the similarity between both traces is larger than a given threshold, the model is accepted as a possible solution and stored. In contrast, if the likeness between the real and the synthetic traces is smaller than the mentioned threshold, the model is erased and a new model is generated.

An important characteristic of this proposed inversion scheme is that the model is generated in a depth domain, so there is no need to convert the model to depth after a probable subsurface model has been accepted. A detailed description of each inversion step is shown in the Chapter 5. The proposed algorithm produces rock property traces instead of elastic property traces. Therefore, the inversion outcome can be directly introduced into the geological model of the studied area.

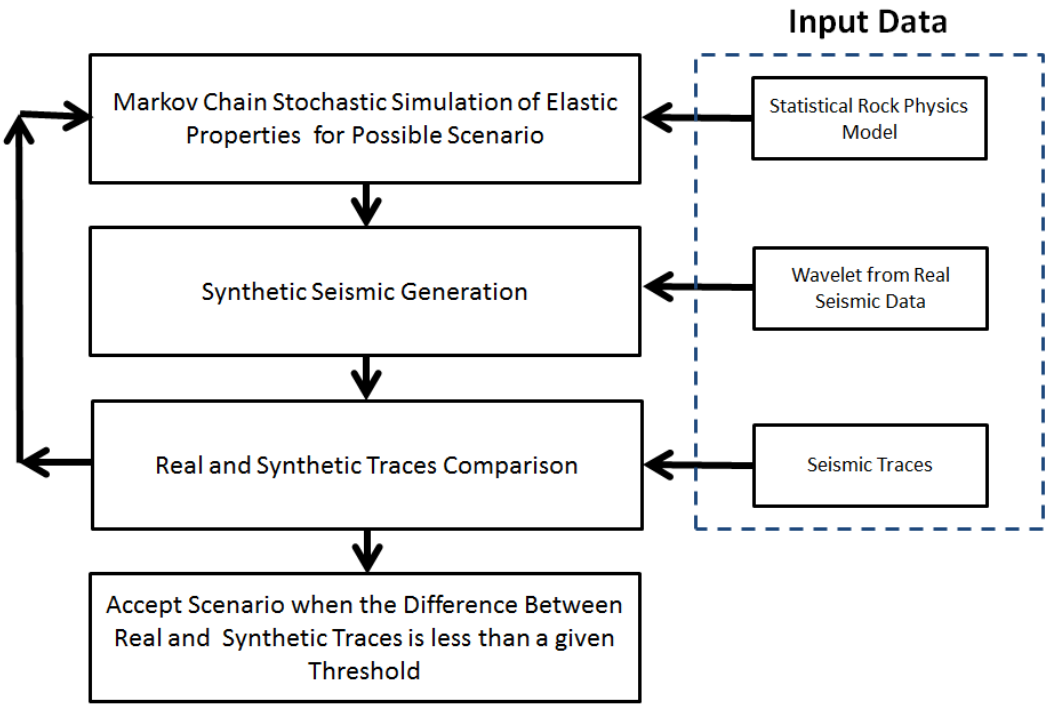

Figure 4.2: Simplified 1D stochastic inversion workflow.

4.3. Possible Scenario Generation

Every 1D model is represented by two main attributes. The first is the layers geometry or how the seismic lithofacies are arranged within the studied interval. Each seismic lithofacies is defined as a discrete variable with a related rock property distribution. The second is the rock properties of the analyzed lithofacies. The scenario generator algorithm works on two levels. First the routine generates the geometry of the probable earth models. Once the geometry

is built, we assign rock properties to each layer. The rock properties are assigned by using a Markov Chain-based stochastic simulation algorithm. This process is illustrated in Figure 4.3. First, the fraction of the seismic lithofacies that constitute the analyzed interval is generated. Once the 1D array with the fractions of the seismic lithofacies that constitute the study interval are generated, the 1D array with the distribution of these lithofacies is produced using the Fisher-Yates shuffle algorithm. This algorithm was originally described by Ronald A. Fisher and Frank Yates in 1938 (Fisher *et al.,* 1938). The Fisher-Yates shuffle algorithm is a numerical method for generating random permutations of a finite number of groups. The most important property of the Fisher–Yates shuffle is that it is unbiased; consequently, every permutation is equally probable. The algorithm to generate a random permutation of the numbers one through N goes as follows:

a) Write down the numbers from one through N;
b) Pick a random number X between 1 and the number of remaining unchosen numbers;
c) Counting from the low end, strike out the Xth number not yet selected and store it;
d) Repeat from step 2 until all the numbers have been selected.

The 1D array of numbers stored after all the numbers are selected is now a random permutation of the original numbers. If the random number generator is truly random and unbiased, the resulting permutation will be also.

An example of the application of the Fisher and Yates method, for an interval that ranges from 1 to 5, is illustrated in Table 4.1.

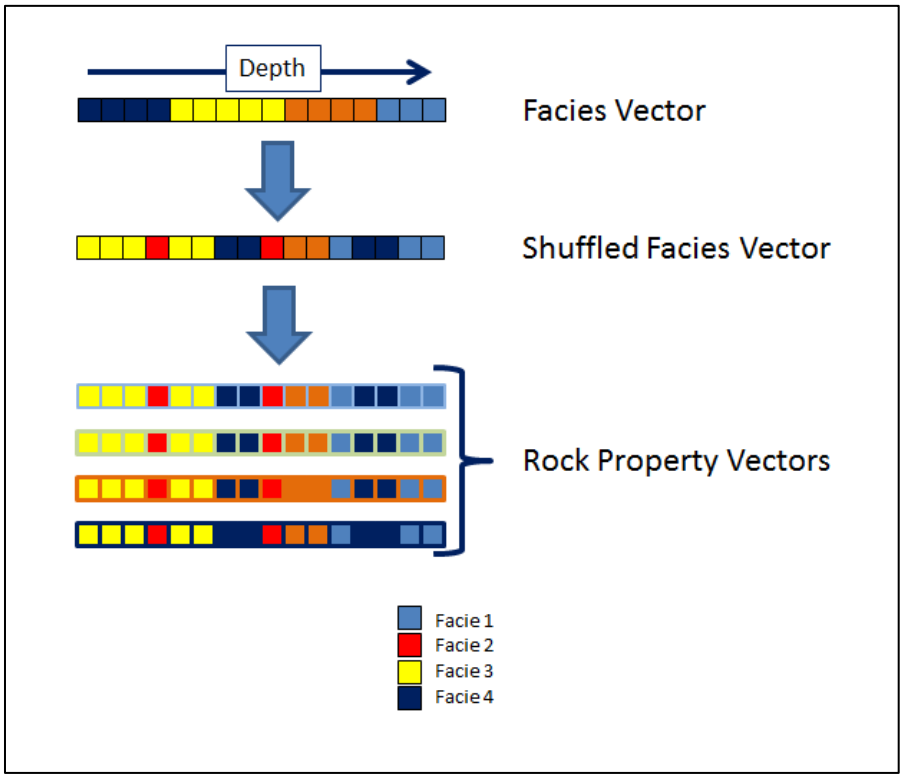

Figure 4.3: Schematic representation of the possible scenario generation.

Table 4.1: Example of the Fisher and Yates shuffle algorithm. The permuted interval ranges from 1 to 5. The red cells correspond to the number that is selected in each iteration.

Step	Random Number	Sequence					Result
1	4	1	2	3	4	5	4
2	1	1	2	3	4	5	4 1
3	3	1	2	3	4	5	4 1 5
4	2	1	2	3	4	5	4 1 5 3
4	1	1	2	3	4	5	4 1 5 3 2

The generated seismic lithofacies indicator 1D array is the template used for the rock property 1D arrays generation. The property 1D arrays are produced in an order that starts with the lithology and porosity, and finishes with the elastic properties. Each cell in the property 1D array is filled with the property information calculated from the multivariate PDF and defined by the Markov Chain. The accuracy of the rock properties model relies on the idea that the multivariable PDF truly represents the statistics of the target lithofacies.

We have also included some additional constraints for our inversion:

a) Fluid contacts: For geological models with local fluid contacts, all samples of gas reservoirs should be above the oil samples and all samples with oil should be above the water samples.

b) Geological age: The seismic lithofacies geometry can be constrained in a given order that follows a stratigraphic column.

c) Layer thickness: The thickness of the layers can be constrained to any given range.

4.4. Synthetic Seismic Generation

The probabilistic inverse problem defined by Equation 1.1 estimates the *a posteriori* PDF ($\sigma_M(m)$) from the *a priori* PDF of the data ($\rho_D(d)$) and the model ($\rho_M(m)$). Equation 1.1 is valid when the information in the space of measured parameters (data) has been obtained independently of the prior information in the model space (Tarantola, 2005). In section 1.1, we introduced forward modeling operator ($g(m)$) that predicts data (Equation 1.2) from the model. The predicted

values are not necessary identical to the observations since there are uncertainties related to the measurements and the proposed model.

In the present study the forward modeling operator is implemented as a convolutional model for the synthetic trace generation. This model is expressed as follows:

$$S(t,\theta) = Rpp(t,\theta) * W(t,\theta), \tag{4.1}$$

where:

$S(t,\theta)$= Synthetic seismic trace,

$Rpp(t,\theta)$= Angle dependent reflection coefficients in time domain,

$W(t,\theta)$= Angle dependent extracted wavelet, and

'*' = Convolution operator.

The convolutional model of the seismic trace assumes that the latter is the superposition of the reflection coefficients filtered by the bandwidth of the recorded wavelet (Sheriff, 1989). Since the elastic property 1D arrays are generated in the depth domain, they have to be stretched to two-way time using a depth-to-time function. We assumed here that the depth-to-time conversion function is part of the input data. Another important part of the input data is the set of seismic wavelets. Seismic wavelets have to be previously extracted from the measured seismic data at the same angle ranges at which the synthetic data have been generated.

After the elastic properties arrays are converted to two-way travel time, they are interpolated to the same regular sampling as the input seismic data. This is a very important process since the time sampling acts as a frequency operator that defines the maximum vertical resolution of the inverted earth model (see Figure 4.4). Finally, a Nyquist filter is applied to the time-stretched elastic models to avoid any possible aliasing in the time domain.

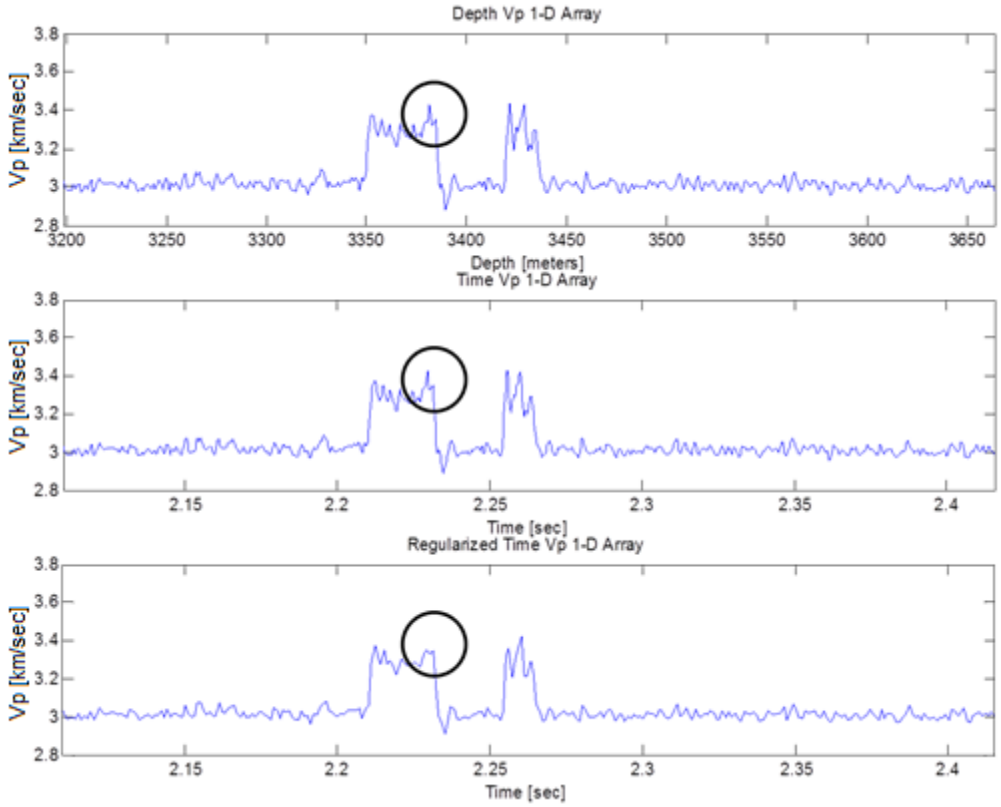

Figure 4.4: Comparison among the depth, time and regularized time 1-D P-wave velocity arrays. The black circles show how the regularization in the time domain can affect the elastic properties of the modeled subsurface.

Once the elastic properties arrays in time have been generated, the angle-dependent reflectivity profiles are produced using the Aki and Richards linear approximation (Aki and Richards, 1980) of the Zoeppritz equation. The Aki and

Richards linear approximation can be expressed in terms of P-wave velocity, S-wave velocity and bulk density (ρ) as follows:

$$Rpp(\theta) = \frac{1}{2}\left(\frac{\Delta Vp}{Vp} + \frac{\Delta \rho}{\rho}\right) + \left[\frac{1}{2}\frac{\Delta Vp}{Vp} - 2\frac{Vs^2}{Vp^2}\left(\frac{\Delta \rho}{\rho} + 2\frac{\Delta Vs}{Vs}\right)\right] sin^2\theta + \frac{1}{2}\frac{\Delta Vp}{Vp}(tan^2\theta - sin^2\theta), \quad (4.1)$$

where:

$\Delta Vp = Vp_2 - Vp_1$ $\qquad$ $Vp = 0.5(Vp_1 + Vp_2)$

$\Delta Vs = Vs_2 - Vs_1$ $\qquad$ $Vs = 0.5(Vs_1 + Vs_2)$

$\Delta \rho = \rho_2 - \rho_1$ $\qquad$ $\rho = 0.5(\rho_1 + \rho_2)$

$\Theta = 0.5(\Theta_1 + \Theta_2);$

Vp, Vs, ρ and Θ are the P-wave velocity, S-wave velocity, bulk density and incidence angle, respectively. The sub-indexes 1 and 2 refer to the upper and lower layers correspondingly. Equation 4.1 can be rewritten as:

$$Rpp(\theta) = A + Bsin^2\theta + C(tan^2\theta - sin^2\theta), \quad (4.2)$$

where *A*, *B* and *C* are the AVO intercept, AVO gradient and AVO curvature. We used the first two terms of AVO Equation 4.2 for the estimation of the angle-dependent reflectivity arrays. The two-term Aki and Richards AVO equation is valid for a maximum incident angle of about 36°.

Finally, the synthetic trace is calculated by the convolution of angle-dependent reflectivity converted to two-way time and the angle-dependent wavelet. Figure 4.5 shows a schematic representation of the synthetic traces generation step.

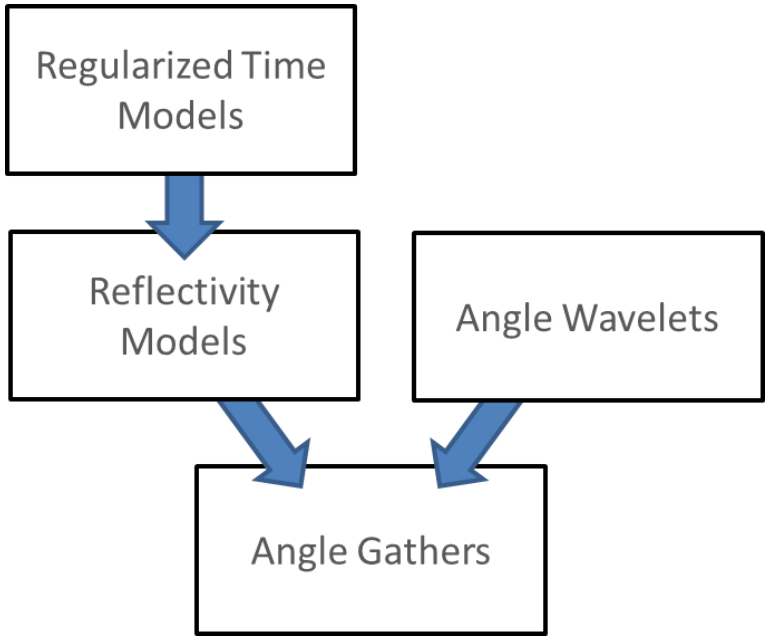

Figure 4.5: Schematic representation of the synthetic traces generation algorithm.

4.5. The Misfit Function

The final step in the 1D stochastic inversion scheme is the estimation of the misfit function between the real and synthetic seismic traces. The synthetic trace is compared to the real seismic trace and if the difference between them is less than a given threshold the model is accepted; otherwise, the model is erased and a new one is generated.

In the proposed algorithm, the similarity analysis is performed in a cascade sequence that starts with the nearest and finished, with the farthest angle-stacked traces. Once a trace is accepted the algorithm analyzes the next angle trace until all the angle-dependent reflectivity traces are accepted. There are many criteria to estimate the degree of similarity between the synthetic and

real traces; we used L^2-norm to measure the similarity between the real and synthetic traces. The L^2-norm can be expressed as follows:

$$\alpha = L^2 - norm = \sqrt{\sum_1^i \left(T_i^{Syn} - T_i^{Real}\right)^2}, \tag{4.2}$$

where: T_i^{Syn}= Synthetic trace, T_i^{Real}= Real trace, and i= ith Element of the 1-D trace array.

An example of one trace misfit analysis is shown in Figure 4.6. The top graph shows the real (black) and synthetic (blue) traces. The difference between the synthetic and real traces is displayed in the center graph. Finally, the cumulative L^2-norm is plotted in the bottom graph. In our proposed algorithm, we select the models that minimize the L^2-norm.

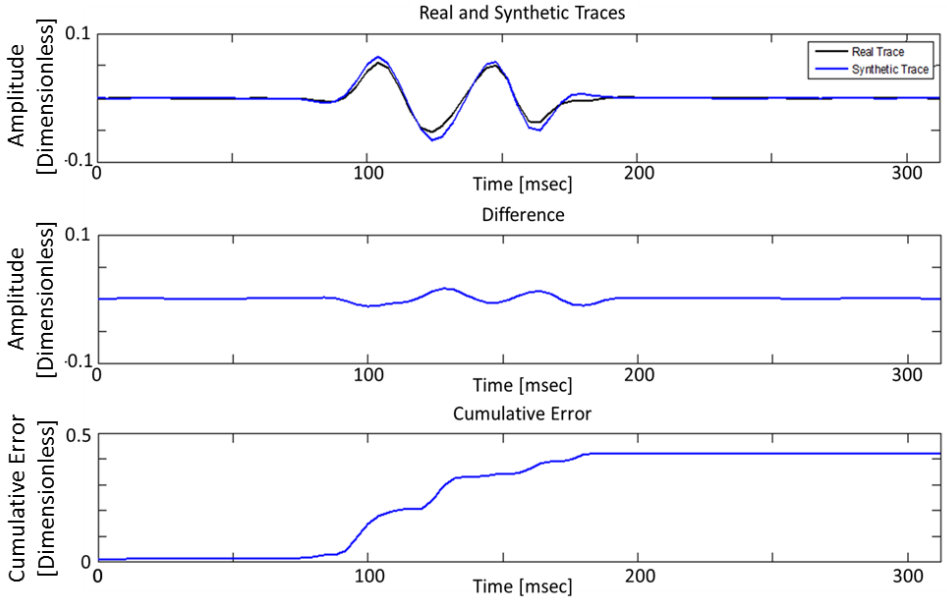

Figure 4.6: Misfit calculation example. In this synthetic example the cumulative L^2-norm shows the intervals with larger misfit.

The probable models generated by the proposed inversion scheme are a valid solution to the studied inverse problem; all of them honor the input rock physics model as well as the measured seismic data.

5. SYNTHETIC EXAMPLES

5.1. Introduction

The central problem in seismic reservoir characterization is the prediction of lithology and saturation from seismic and well log data. In this chapter we present the results of the application of our proposed inversion scheme on two different sets of synthetic data. The synthetic data sets were generated based on real well data with the goal of testing the inversion in two different geological environments. The first synthetic data set is composed of low porosity high impedance sand. The goal of the second example is to replicate a high porosity low impedance clastic environment. In this example, the target reservoir rock is characterized by weakly compacted uncemented sandstones.

In both synthetic tests, the model data space is represented by the multivariate PDFs that were generated from the synthetic log and extended by theoretical models. For instance, changes in pore fluid properties were modeled using Gassmann fluid replacement theory. The rock's properties in both synthetic log data sets were based on real measured data. Next, the data space was generated using synthetic seismic data modeled from synthetic elastic well logs. As discussed in Section 4.4, the forward modeling operator was based on the convolutional model of the seismic trace.

The content of this chapter was partially presented in the paper IPTC-18040 of the 2014 International Petroleum Technology Conference in Kuala Lumpur.

5.2. Synthetic Test 1: Cemented Sand

The first synthetic data set was based on real well log data measured in a Cretaceous interval; the *in situ* well logs are displayed in Figure 5.1. The synthetic model was formed by two sands encapsulated into a shale sequence. The top upper sand is located at 3,347 meters depth with a thickness of 40 meters. The lower sand is thinner with a thickness of 20 meters and located just 32 meter bellow the base of the upper sand. The target reservoirs are cemented sand with average porosity of 16%. The background P-wave impedance is about 10 km*kg/sec*cc. The average P-impedance corroborates that the sands are well compacted and cemented.

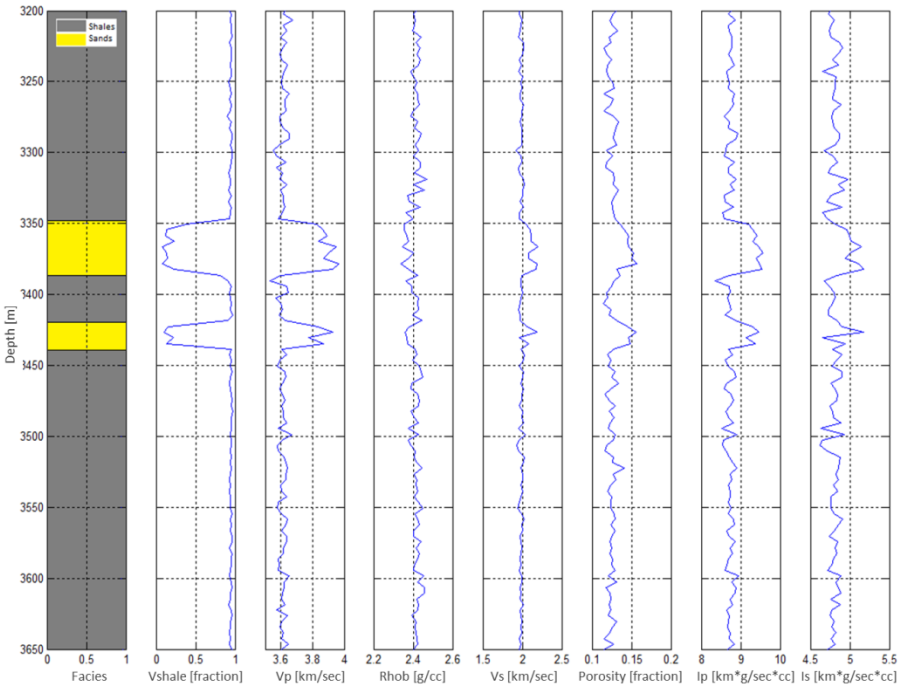

Figure 5.1: Model 1 synthetic well logs showing (from left to right) facies indicator, shale volume, P-wave velocity, bulk density, S-wave velocity, porosity, P-wave impedance and S-wave impedance.

In this kind of elastic scenario, fluid variations have very small influence on the elastic properties of the target reservoirs. In high-impedance reservoir settings, the goal of quantitative interpretation is usually the prediction of gross reservoir thickness and reservoir quality. In our study here, the gross reservoir thickness is expressed by the fraction of the potential reservoir rock in the inverted interval. The reservoir quality is defined by two properties, which are the fraction of shale (shale volume) and the total porosity of the sandstone. The study reservoir properties are described by non-parametric histograms and descriptive statistical estimators.

The elastic fluid properties profiles for brine, oil and gas were estimated using the Batzle and Wang (1992) equations and assuming pressure and temperature gradients of 9.72 MPa/km and 22.3 °C/km. Oil gravity, gas gravity and salinity were 36° API, 0.6 and 8,000 ppm respectively. Figure 5.2 shows the P-wave and density profiles for three possible pore fluids. Once the fluid properties are estimated, the fluid replacement is performed using the Gassmann relations. The fluid substitution was performed from brine to 90% hydrocarbon saturated sands.

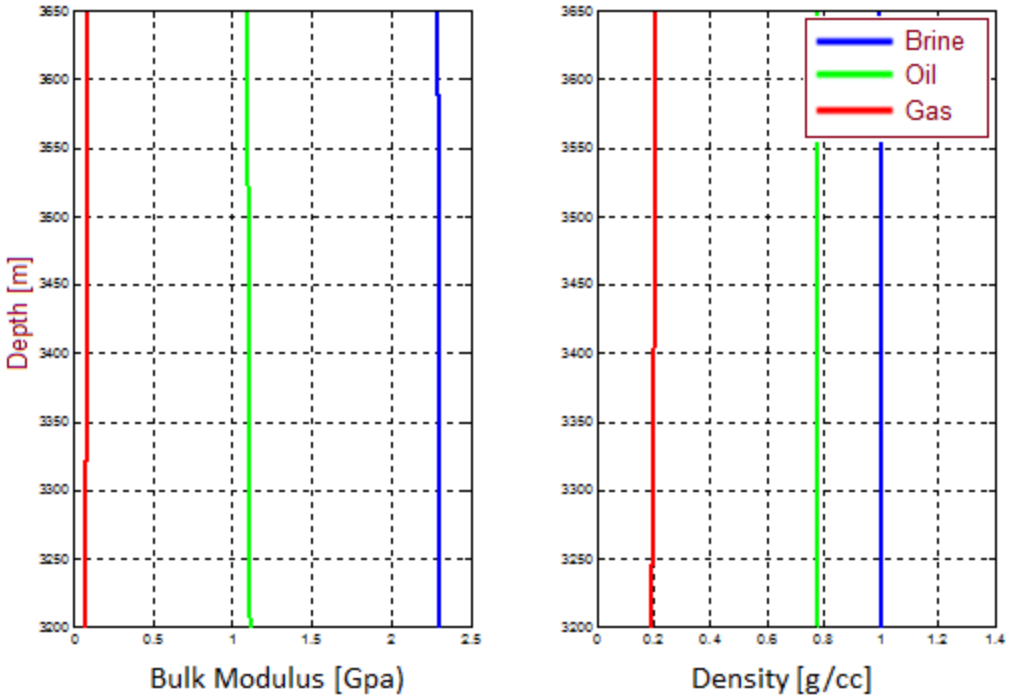

Figure 5.2: Synthetic model 1 pore fluids velocity and density profiles.

The final seismic lithofacies multivariate PDF projections for the Vp-Vs, Vp-Rhob, and PhiT-Vp spaces are shown in Figure 5.3. The effect of the fluid variations on the elastic properties of the permeable rocks is negligible. However, there was good lithology discrimination in all projected spaces. Hence, the test was planned focus on the prediction of gross reservoir thickness and reservoir quality.

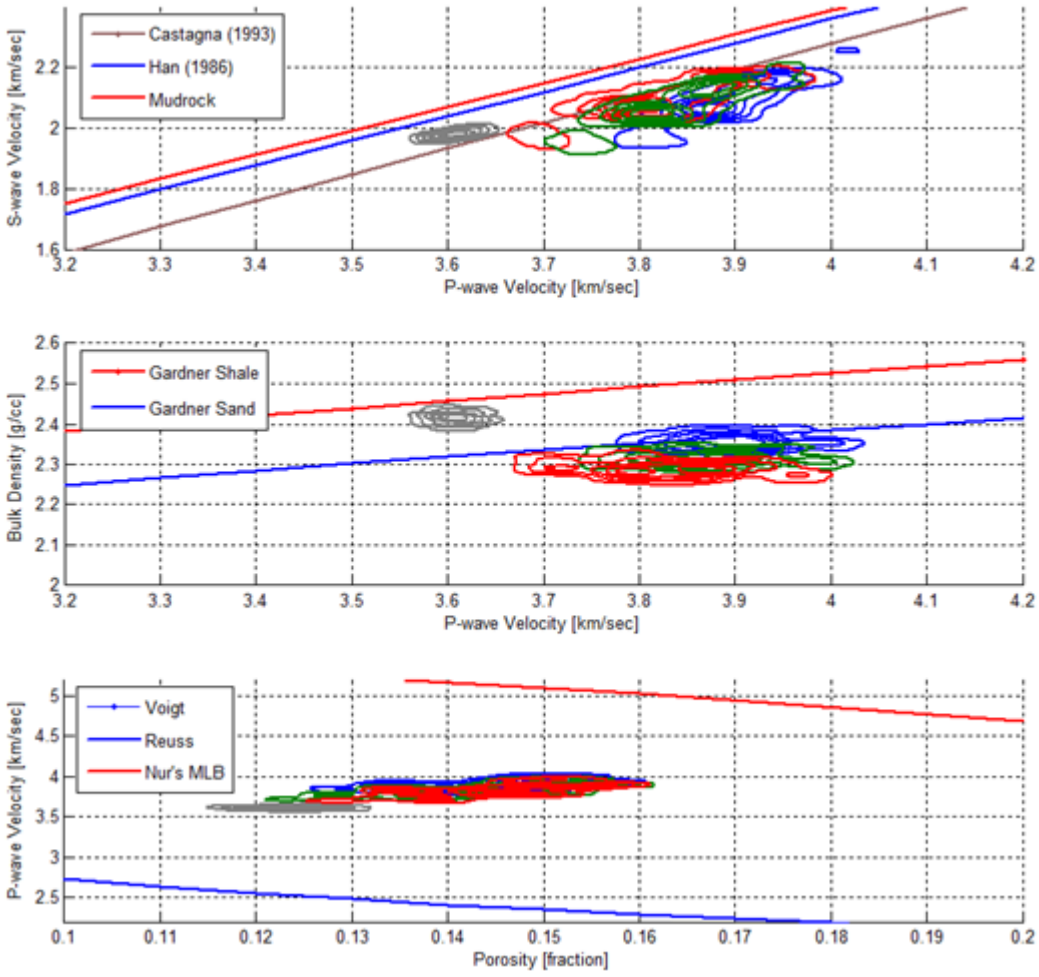

Figure 5.3: Final seismic lithofacies multivariate PDF projections for the Vp-Vs (Upper), Vp-Rhob (Center), and PhiT-Vp (Lower) spaces. Green, blue, brown and red contours denote shales, brine sands, oil sands and gas sands, correspondingly. Some empirical models are plotted for comparison including Castagna's mudrock line, Castagna's 1993, Han's 1986, Gardner's sand, Gardner's shale, Voigt bound, Reuss bound and Nu's modified Voigt bound for quartz mixture.

The angle-dependent reflectivity curves were generated from the synthetic logs converted to time. They showed strong positive reflection coefficients at the top of both sands. It was clearly evident that one of the challenges in this test was to accurately predict the reservoir geometry in the target interval. Figure 5.4

shows the model 1 angle dependent reflectivity profiles. It can be observed how the reflectivity of the top and base of the sands decrease with the angle of incidence. This is typical reflectivity response of high impedance sands.

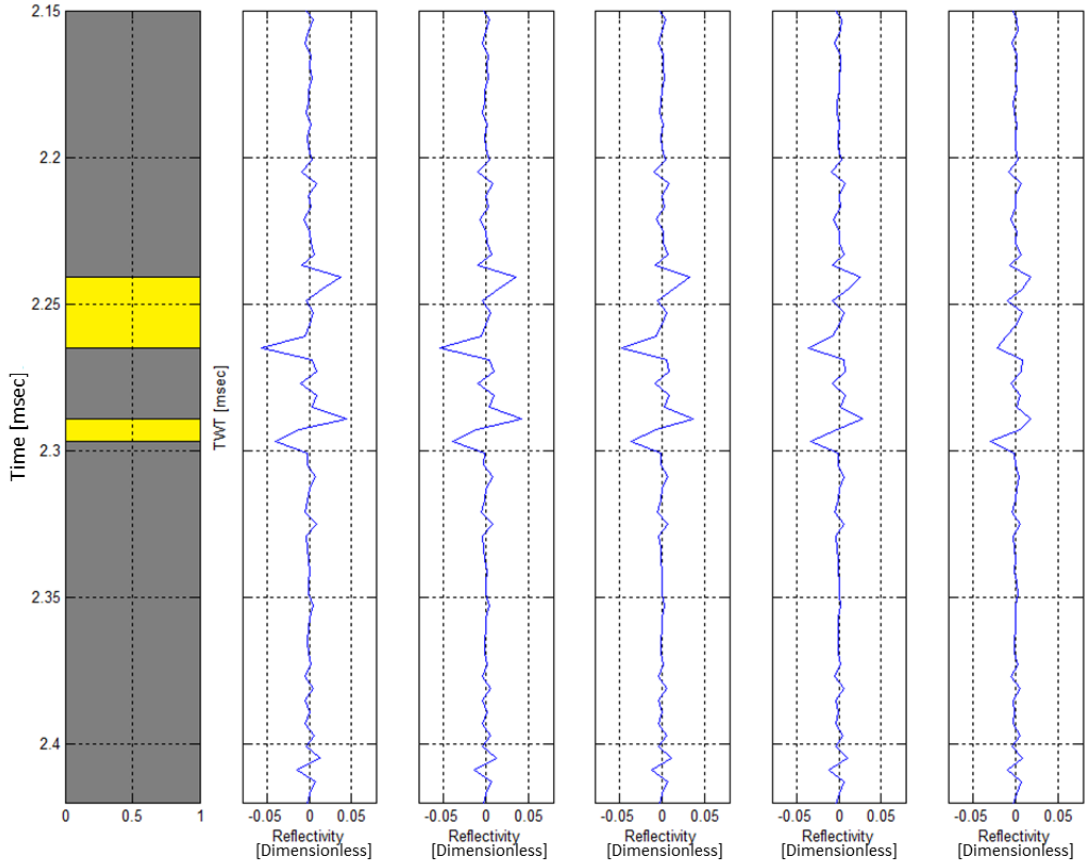

Figure 5.4: Model 1 angle dependent reflectivity profiles.

Next, we generated the synthetic angle stack traces by convolving the angle-dependent reflectivity with a Ricker wavelet with a central frequency of 25 Hz (Figure 5.5).

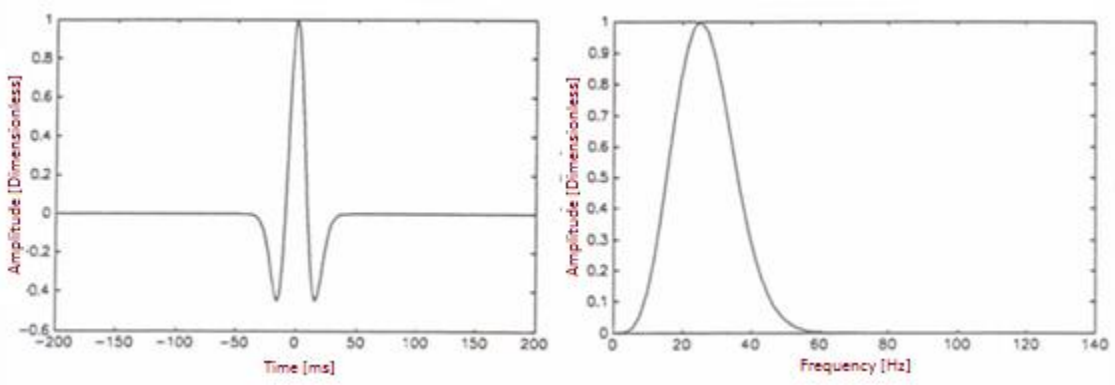

Figure 5.5: Ricker wavelet with a central frequency of 25 Hz.

For this test we assumed the stationarity of the wavelet, meaning that wavelet did not vary with incident angle or propagation time. The results of this forward modeling are shown in Figure 5.6. A set of five angle traces were generated equally spaced in an interval that ranged from 0° to 32°. This angle gather was used as the measured seismic data for this synthetic test.

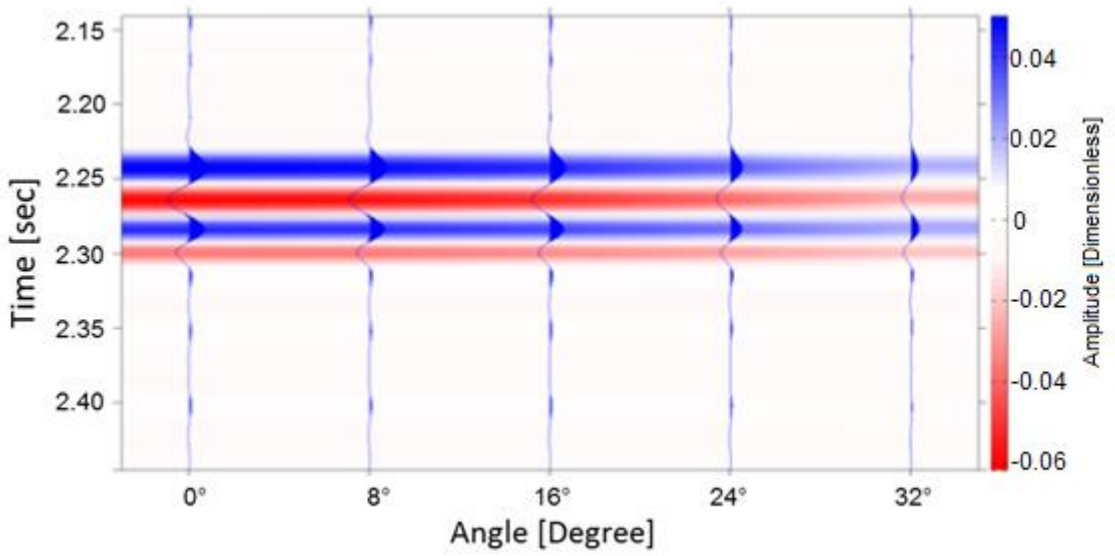

Figure 5.6: Synthetic angle gather generated from the synthetic model 1.

Once the “real traces” were generated the next step was to produce the multivariate PDF for each of the analyzed lithofacies. The 2D projections of the multivariate PDF (Figure 5.6) show that the sands have larger p-wave velocity, lower Vp/Vs ratio and larger density than the surrounding shales. The observations in Figure 5.7 indicate that there is an excellent lithofacies discrimination based on the elastic properties of the analyzed statistical populations.

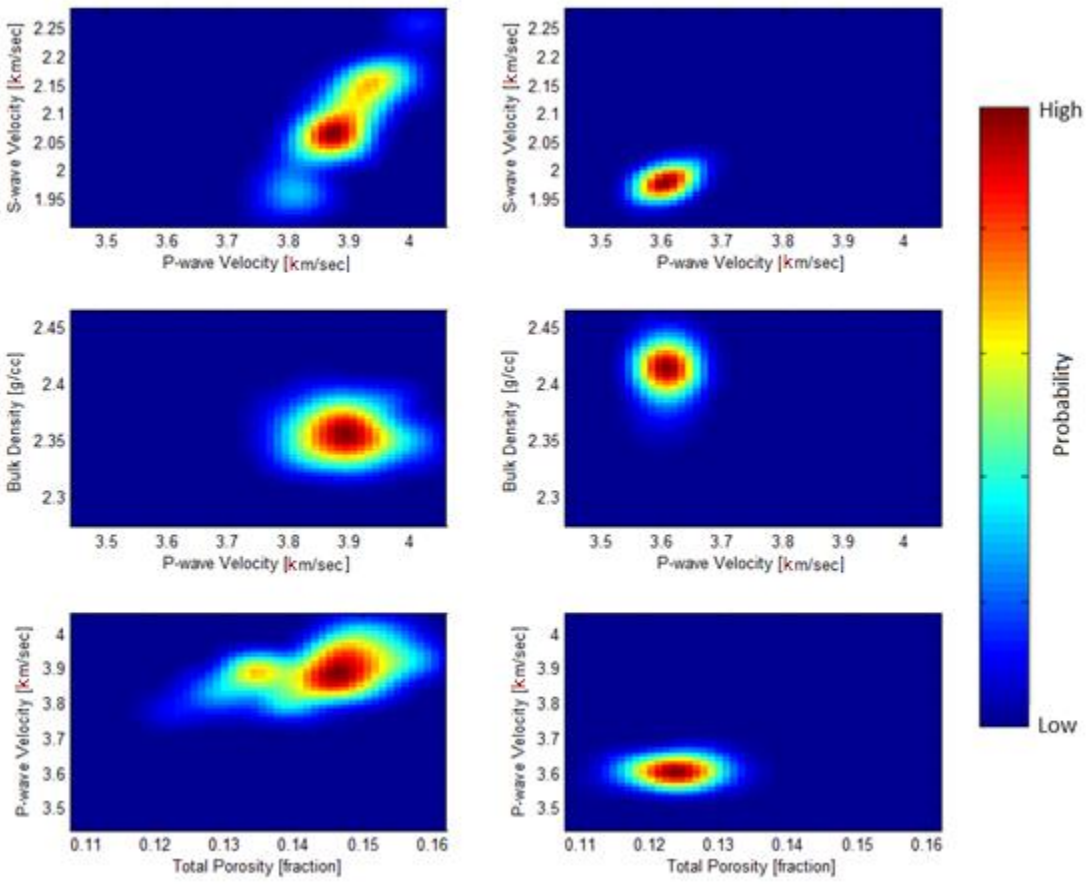

Figure 5.7: 2D Projections of the multivariate probability distribution function for sands (left) and shales (right) calculated from the synthetic model 1.

The inversion was performed for one million realizations using the model shown in Figure 5.6 as the measured data and the multivariate PDFs shown in figure 5.7 as the rock physics models. Modeled traces with similarity factor (α) smaller than 0.9 were selected as possible solutions for the stochastic inversion of the synthetic data. The comparison between the synthetic seismic data and the 1,112 possible solutions revealed the close similarity between the synthetic measured data and the probable models seismic traces. The residuals were small, the time arrivals (Figures 5.8) and waveforms (Figures 5.9) similar.

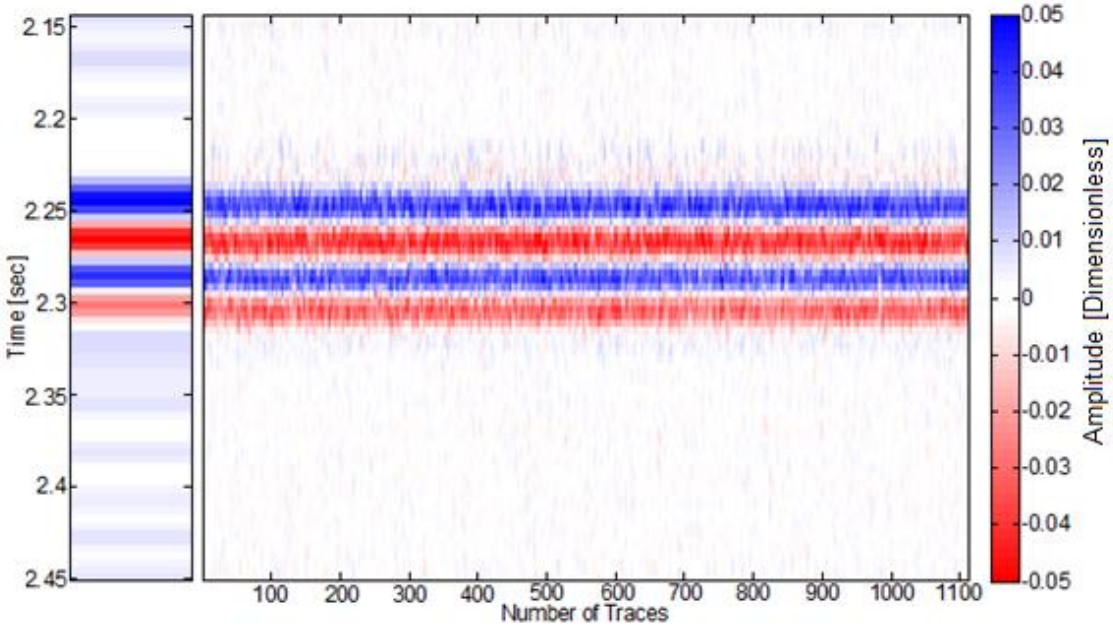

Figure 5.8: Real seismic trace (left) and possible models traces (right) comparison. The selected traces have L^2-norms smaller than 0.9.

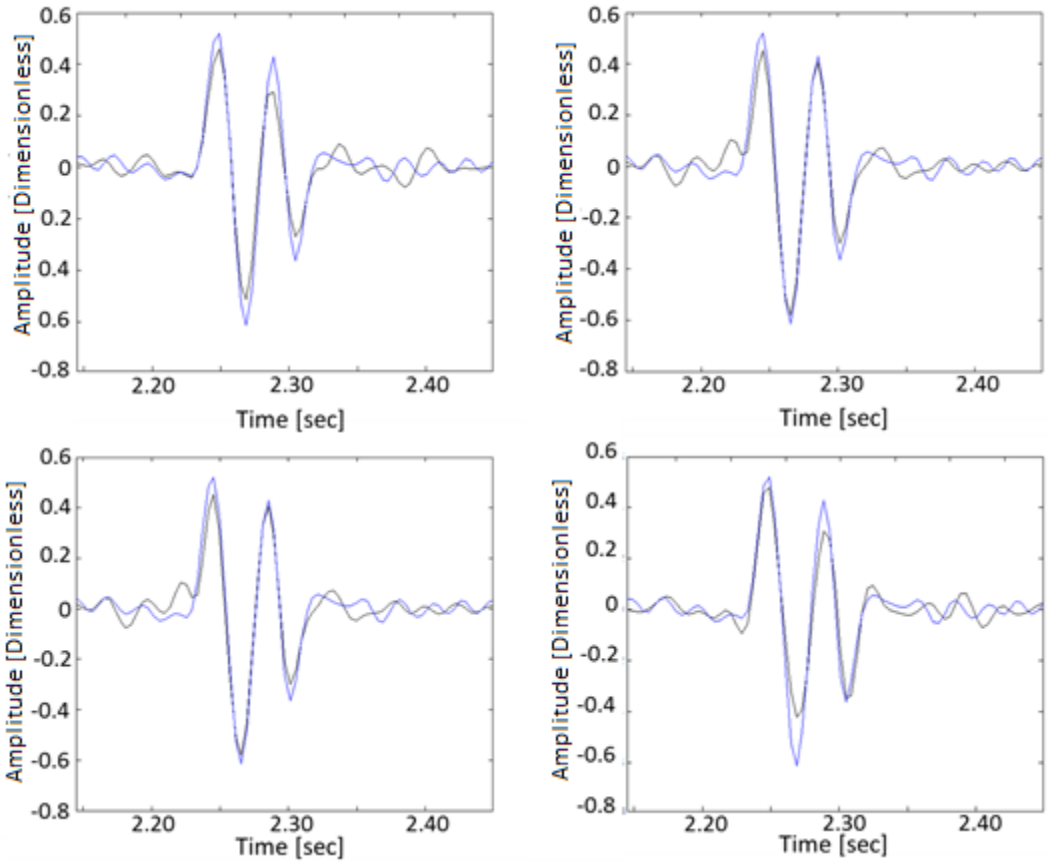

Figure 5.9: Synthetic versus modeled waveform comparison for four possible models with α<0.9.

The seismic lithofacies possible models with α<0.9 are displayed in Figure 5.10. It can be observed that most of the sand samples are located inside the limits of the upper and lower sands. In fact, these sands are well-delimited by most of the probable inversion solutions. As discussed Section 5.1 we are interested in the prediction of gross reservoir thickness and reservoir quality. Gross reservoir thickness is defined by the fraction of sand in the target interval. Figure 5.11 shows the PDF of the sand fraction for all probable models with

α<0.9. The most expecting value of the sand fraction is 0.13, which is the same fraction defined in the synthetic model. However, there is not a sole solution, since the inversion produces a range of likely solutions that are constrained by the rock-physics model.

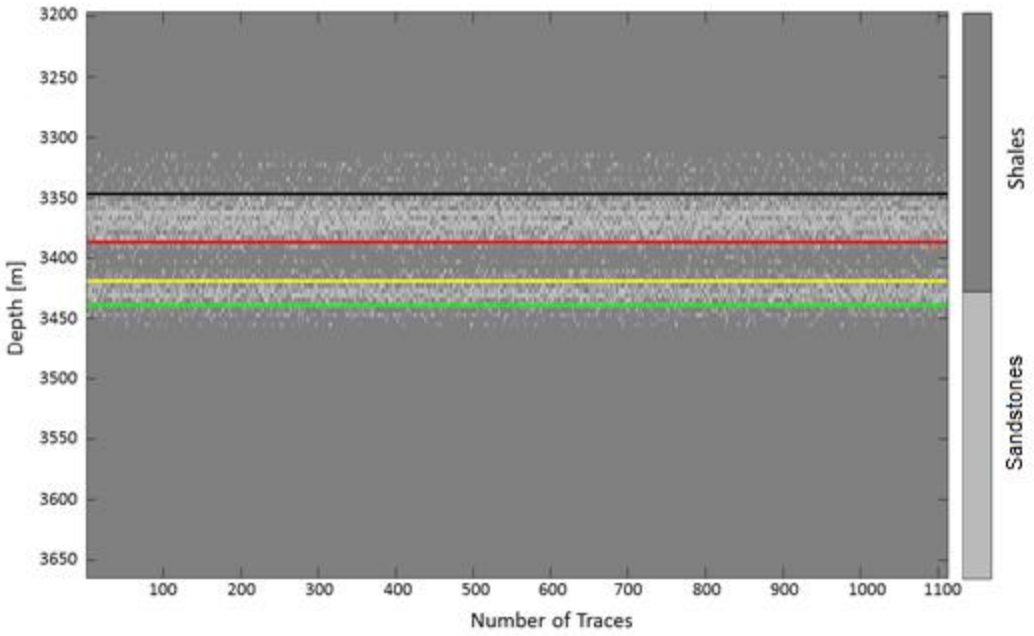

Figure 5.10: Probable models with α<0.9. The black, red, yellow and green lines represent the top of upper sand, base of upper sand, top of lower sand and base of lower sand, respectively.

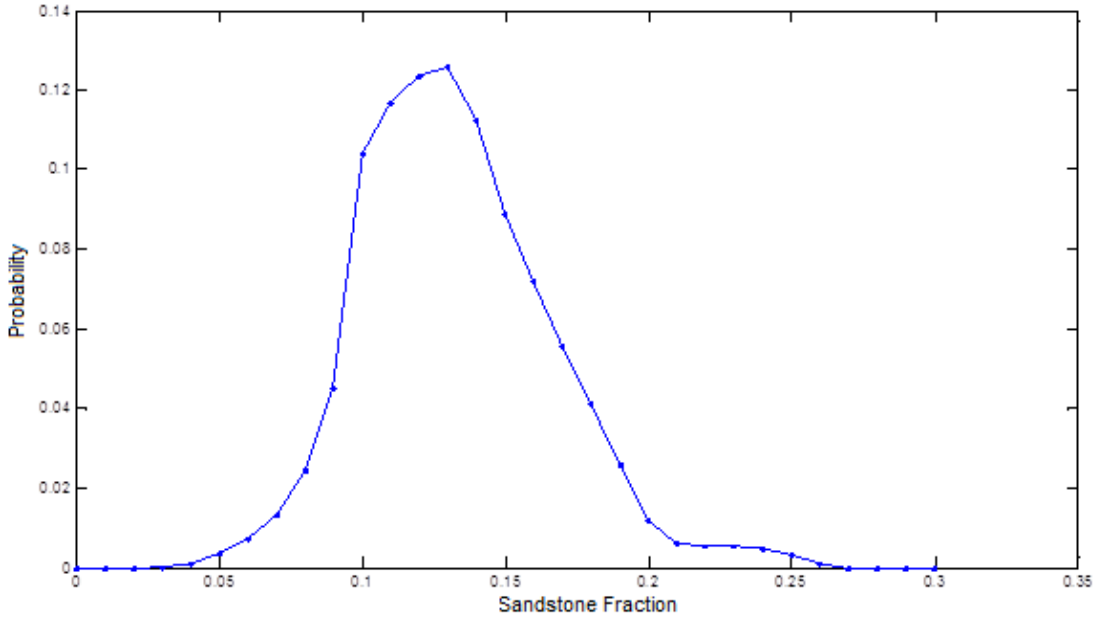

Figure 5.11: Sandstone fraction for probable models with α< 0.9.

Once the geometrical distribution of the two seismic lithofacies was calculated from the probable models, we were able to define the key rock properties for each lithofacies, and especially for the sandstones. For this particular case, total porosity was a very important property for the definition of reservoir quality. From the total-porosity models in Figure 5.12 we were able to calculate some descriptive statistical coefficients; for this particular test, the most likely sand total porosity was about 0.15, with a standard deviation of 0.7. From the total porosity and volume of shale probable models (Figure 5.13), it was possible to estimate the effective porosity of the target reservoir (Figure 5.14). Finally, the elastic property solutions are shown in Figure 5.15.

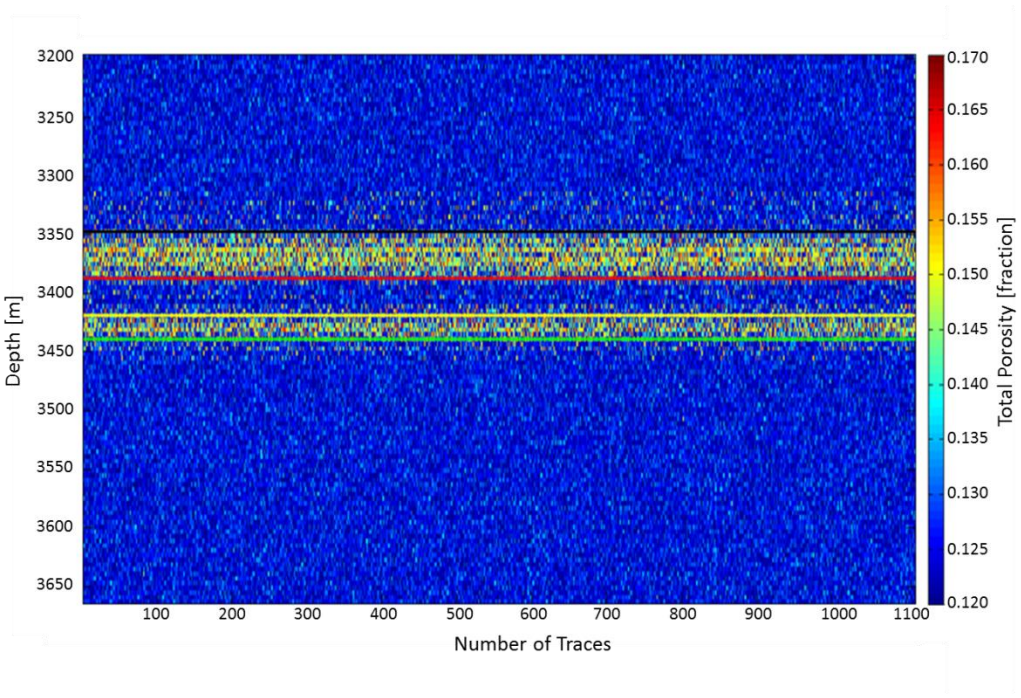

Figure 5.12: Total porosity of the probable models with α<0.9. The black, red, yellow and green lines represent the top of upper sand, base of upper sand, top of lower sand and base of lower sand, respectively.

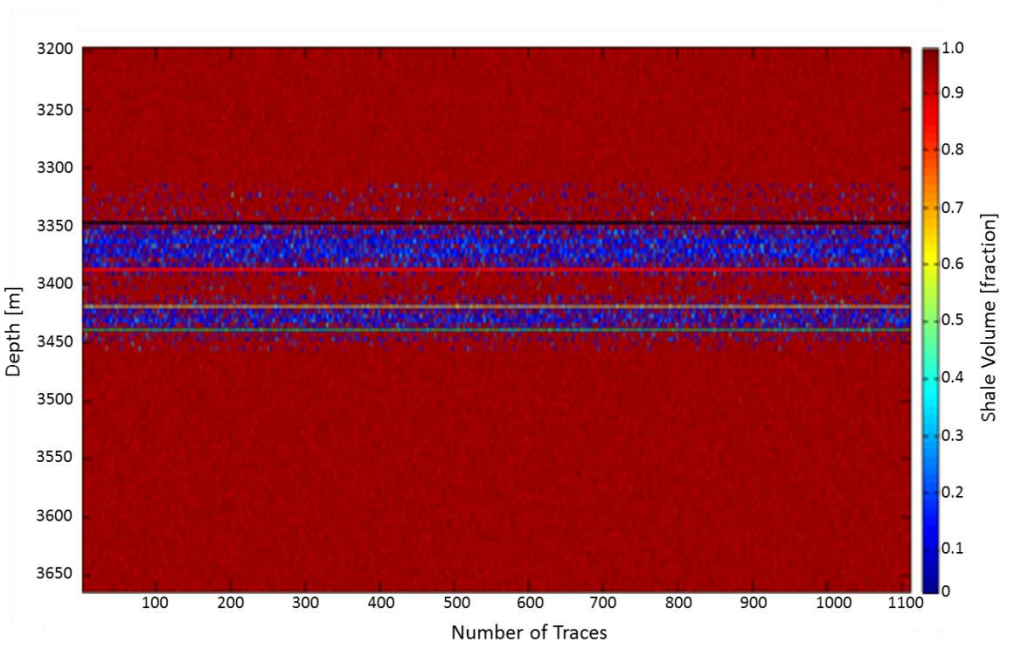

Figure 5.13: Volume of shale probable models with α<0.9. The black, red, yellow and green lines represent the top of upper sand, base of upper sand, top of lower sand and base of lower sand, respectively.

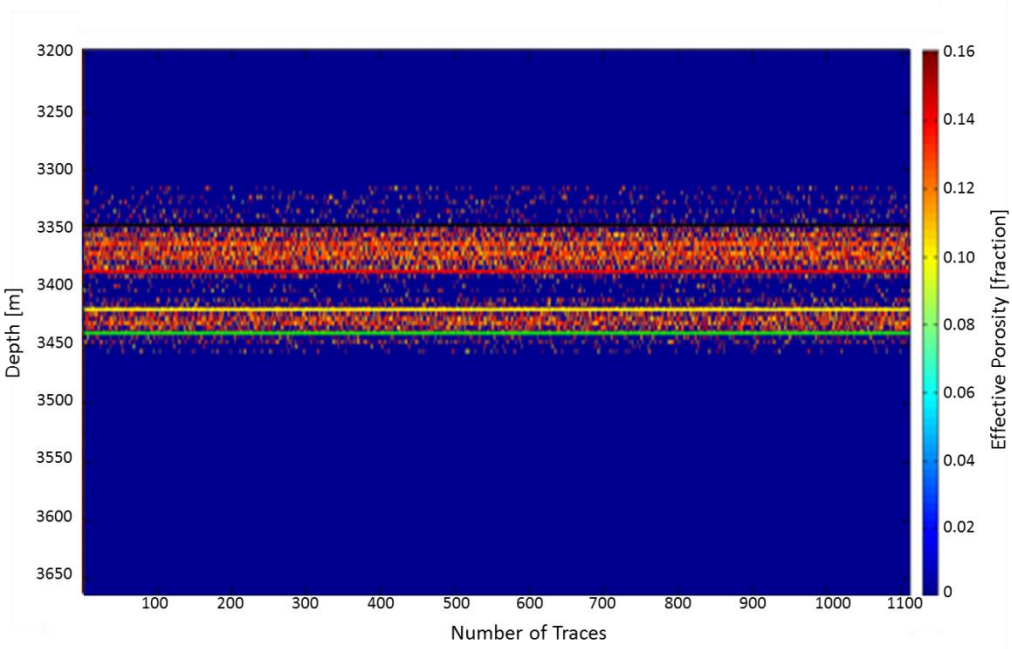

Figure 5.14: Effective porosity probable models with α<0.9. The black, red, yellow and green lines represent the top of upper sand, base of upper sand, top of lower sand and base of lower sand, respectively.

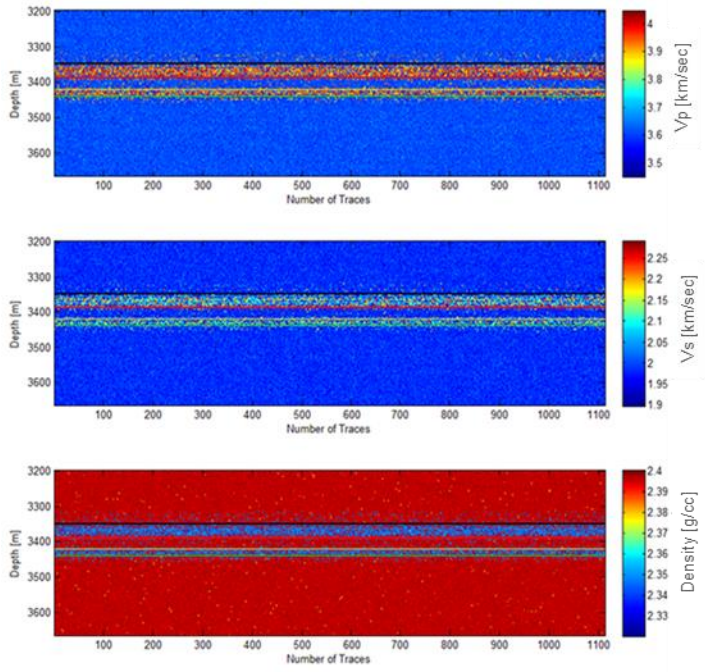

Figure 5.15: Elastic models with α<0.9. The black, red, yellow and green lines represent the top of upper sand, base of upper sand, top of lower sand and base of lower sand respectively.

As has been mentioned before, all the solutions generated by the proposed seismic inversion scheme are probable answers to the analyzed seismic inverse problem. Therefore, the statistics of the solutions have more significant relevance than the models themselves. The comparison between the rock properties of the synthetic model and the solutions (Figure 5.16) shows a very close similarity between the synthetic data and the inversion solutions. The synthetic model used in this exercise is realistic and it is based on measured well log information.

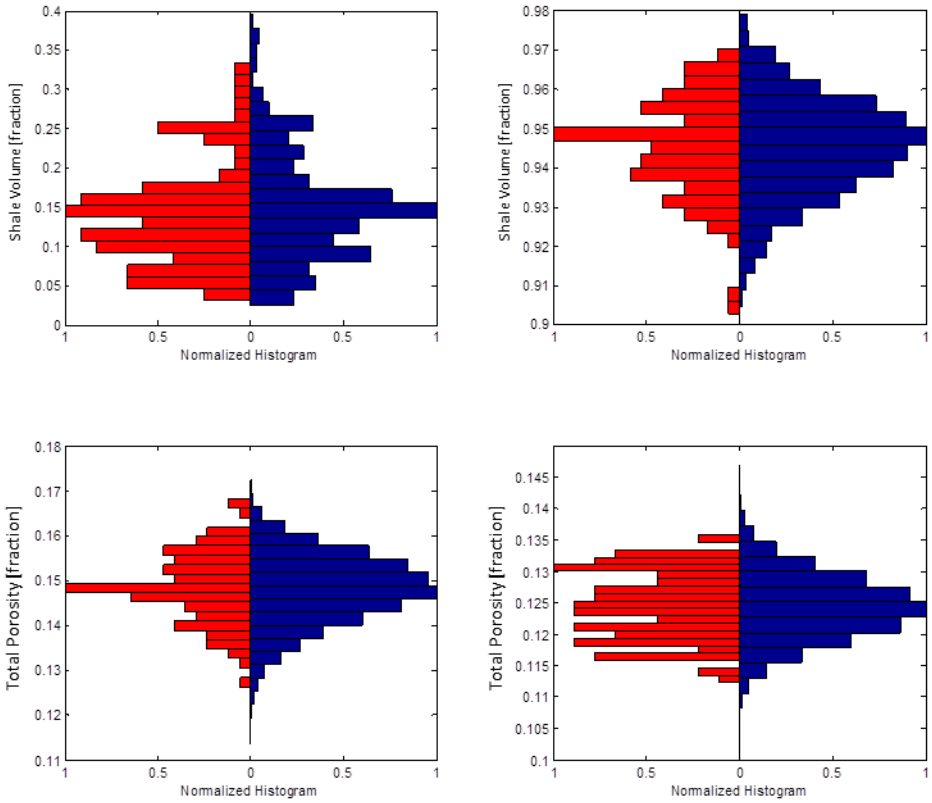

Figure 5.16: Normalized histograms comparison between the rock properties of the synthetic model and the probable solutions, for sand's shale volume (upper left), sand's total porosity (lower left), shale's shale volume (upper right) and shale's total porosity (lower right). Red and blue bars correspond to synthetic model and solutions, respectively.

It is clear that if α decreases the similarity of the possible models will increase. However, the number of possible models will decline as well. Figure 5.17 shows the possible solution models for α<0.045; in this particular case, we obtained 78 possible models instead of the 1,112 calculated with α<0.9. This is an important characteristic of the proposed inversion scheme; this is further discussed in Section 7.4.

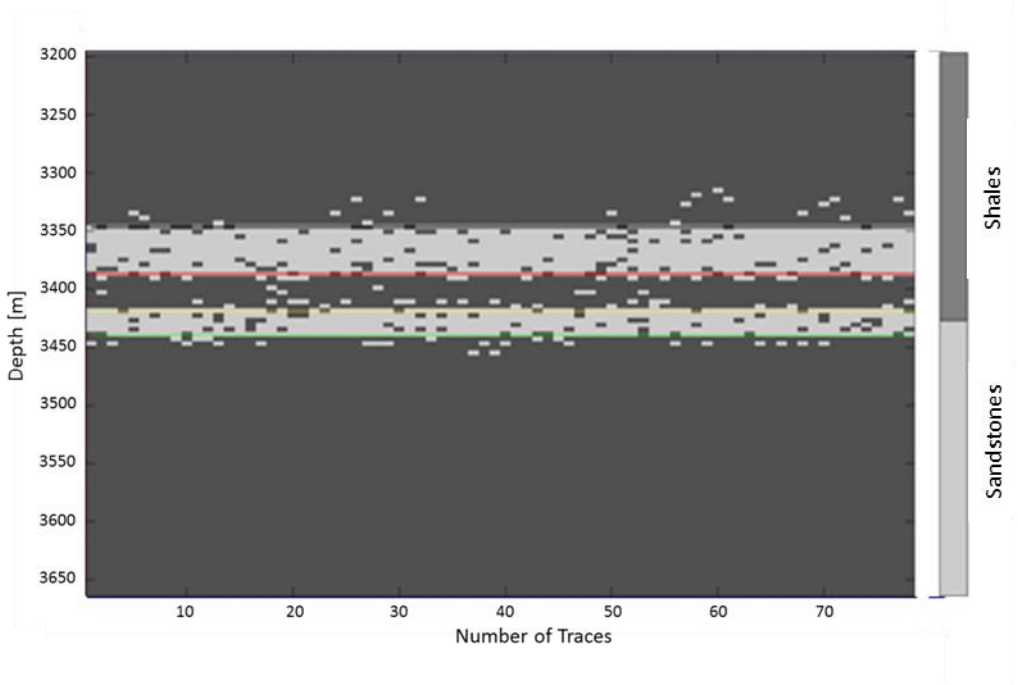

Figure 5.17: Probable models with α<0.045. The black, red, yellow and green lines represent the top of upper sand, base of upper sand, top of lower sand and base of lower sand, respectively.

5.3. Synthetic Test 2: High Porosity Sands

The first synthetic test proved the viability of the application of the proposed inversion scheme to predict the geometry and quality of the reservoir of

the target formation. The goal of the second synthetic test is to replicate a high-porosity, low-impedance clastic environment. In this example, the target reservoir rock was characterized by uncemented sandstone with an average porosity of 31%. In this geological setting, fluid properties variations have very strong effect on the elastic properties of the studied sands. The associated hydrocarbon seismic signatures of these high-porosity reservoirs are usually anomalous high amplitude reflections called “bright spots”. In this test, the objective was to define the fraction of sand, the fraction of hydrocarbon sand, the fluid contact, the volume of shale and the effective porosity of the analyzed sand.

The synthetic well logs, displayed in Figure 5.18, show the *in situ* case in black line, brine case in blue and the gas case in red. The fluid replacement was performed using the Gassmann relations. The elastic fluid properties profiles for brine, oil and gas (Figure 5.19) were estimated using the Batzle and Wang (1992) equations and assumed pressure and temperature gradients of 9.72 MPa/Km and 20 °C/Km. The gas gravity and salinity were 0.6 and 10,000 ppm respectively. The well logs indicated that the brine-saturated sandstone had larger impedance than the surrounding shale. However, when the pore fluid was substituted from brine to a mixture of 90% gas and 10% brine, the sandstone’s impedance became lesser than the shale’s acoustic impedance. Again, the rock-physics diagnostic plot (Figure 5.20) shows the most important rock properties for the three analyzed seismic lithofacies; in general, the elastic discrimination among the seismic groups was good.

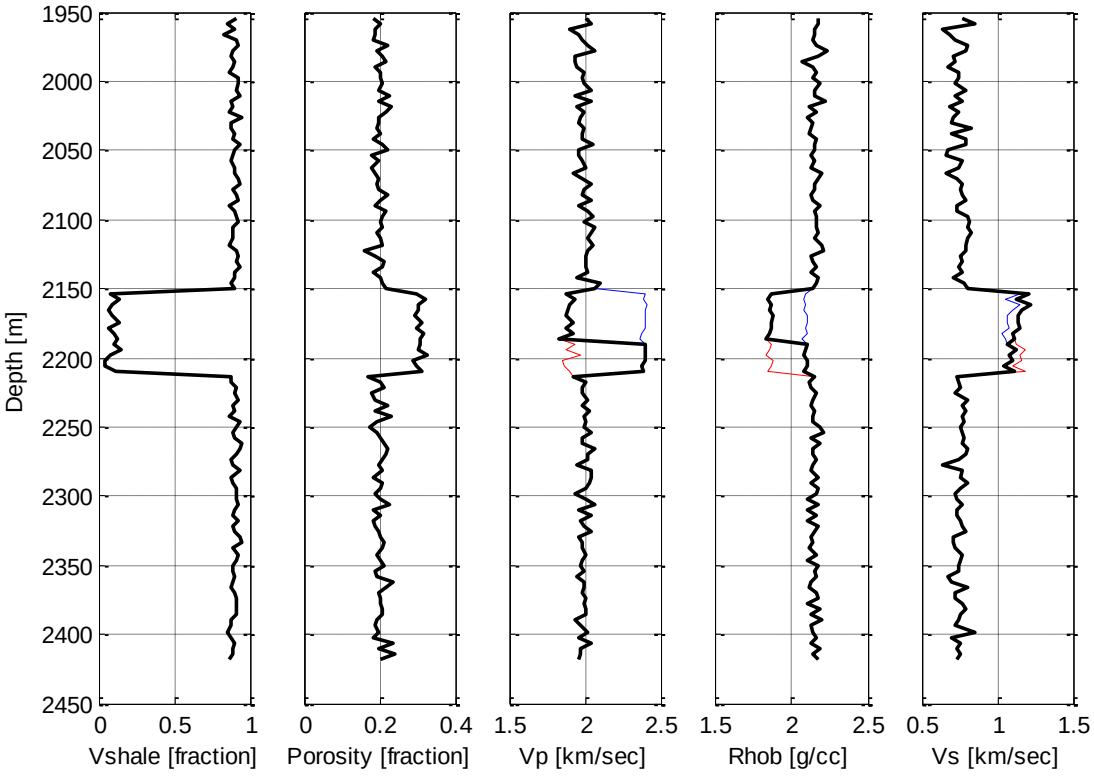

Figure 5.18: Model 2 synthetic well logs showing (from left to right) facie indicator, shale volume, porosity, P-wave velocity, bulk density and S-wave velocity. Black, blue and red lines correspond to *in situ*, brine and gas saturations.

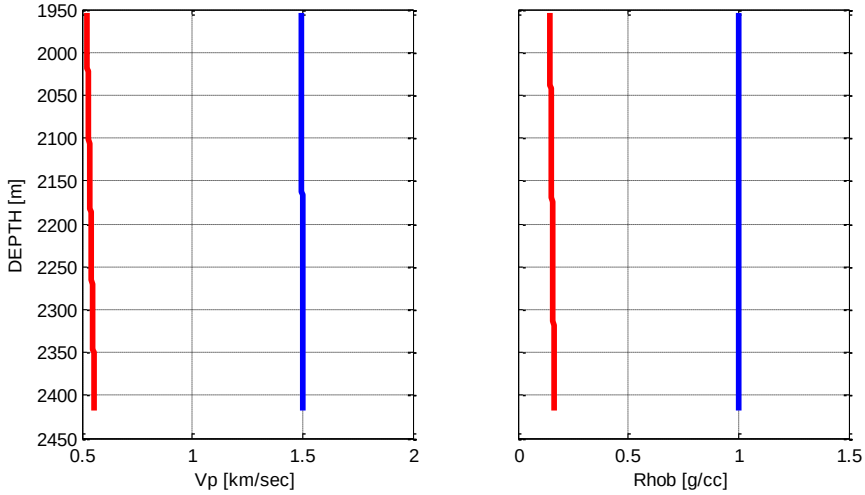

Figure 5.19: Synthetic model 2 pore fluids velocity (left) and density profiles (right). Blue and red lines correspond to brine and gas, respectively.

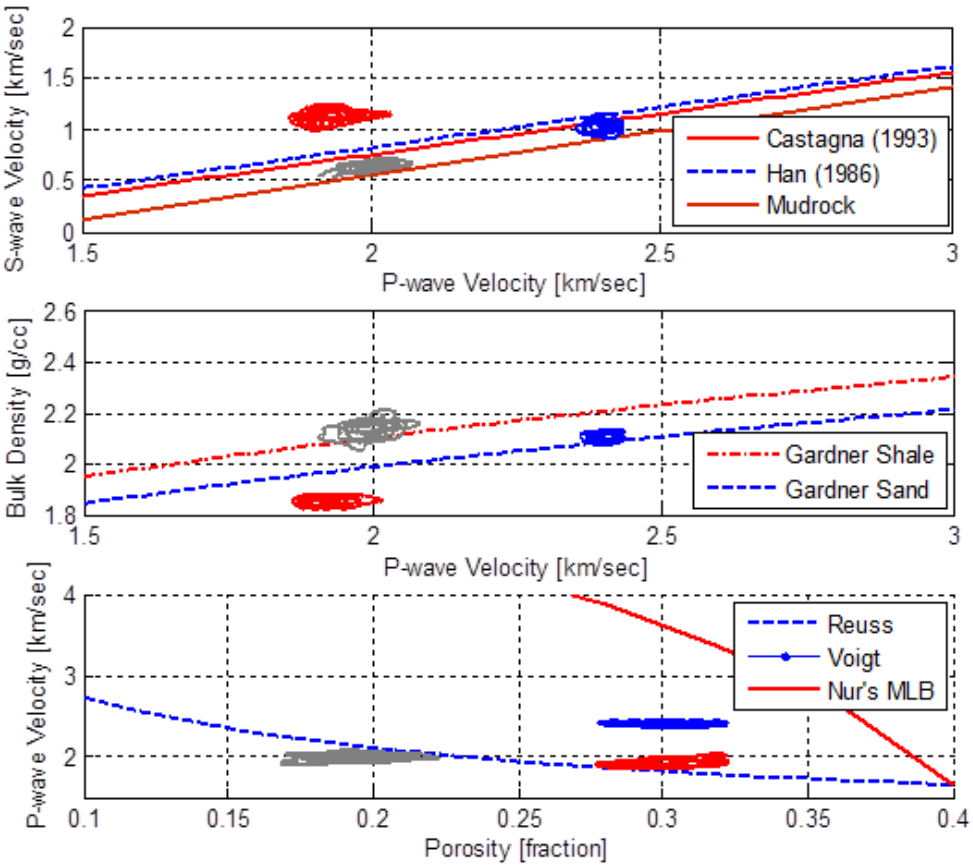

Figure 5.20: Final seismic lithofacies multivariate PDF projections for the Vp-Vs (Upper), Vp-Rhob (Center), and PhiT-Vp (Lower) spaces. Grey, blue, and red contours denote shales, brine sands and gas sands, correspondingly. Some empirical models are plotted for comparison, including Castagna's Mudrock line, Castagna's 1993, Han's 1986, Gardner's sand, Gardner's shale, Voigt bound, Reuss bound and Nu's modified Voigt bound for quartz mixture.

The angle-dependent reflectivity plot (Figure 5.21) shows the main impedance contrasts in the studied interval; the top of the gas sand is delineated by a negative reflection coefficient with strong negative gradient. The largest positive reflection coefficient corresponds to the gas-brine fluid contact within the sandstone. This seismic interface has a relative small positive AVO gradient.

Finally, the base of the brine-saturated sand is defined by a negative reflectivity with a strong negative gradient.

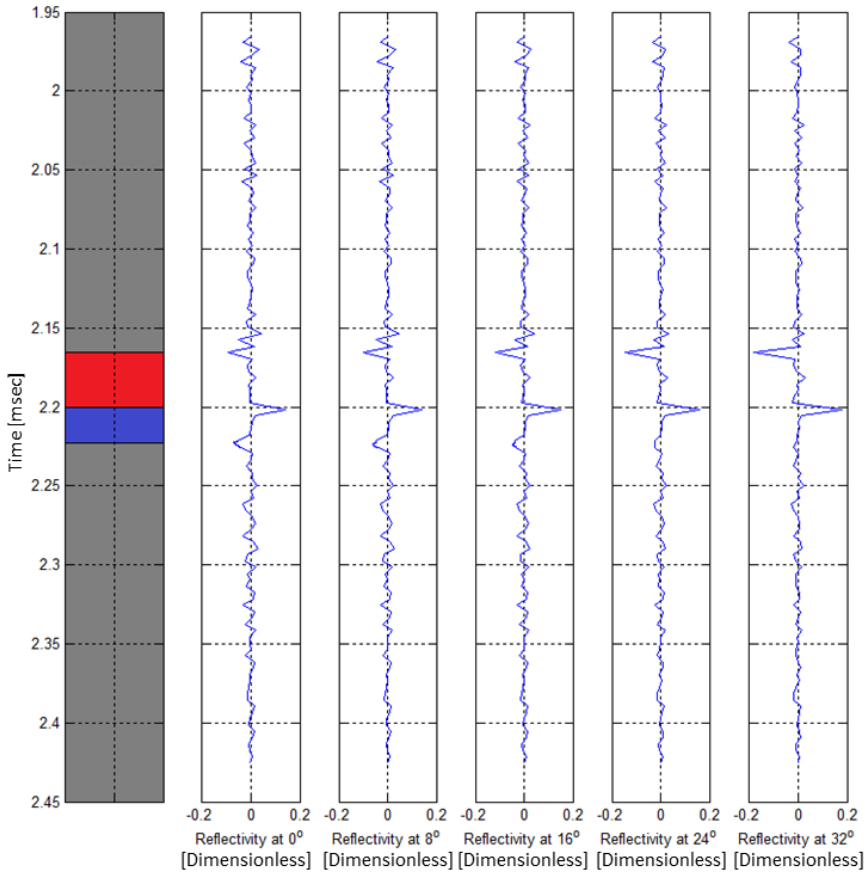

Figure 5.21: Model 2 angle-dependent reflectivity profiles.

The synthetic angle gather (Figure 5.22) was generated by convolving a 25 Hz Ricker wavelet (Figure 5.5) with the reflectivity logs displayed in Figure 5.22. As was expected, the most important reflection is the gas-brine fluid contact situated at approximately 2.200 seconds. Next, the multivariate probability functions were generated for the shale, the brine sand and the gas sandstone seismic lithofacies (Figure 5.23).

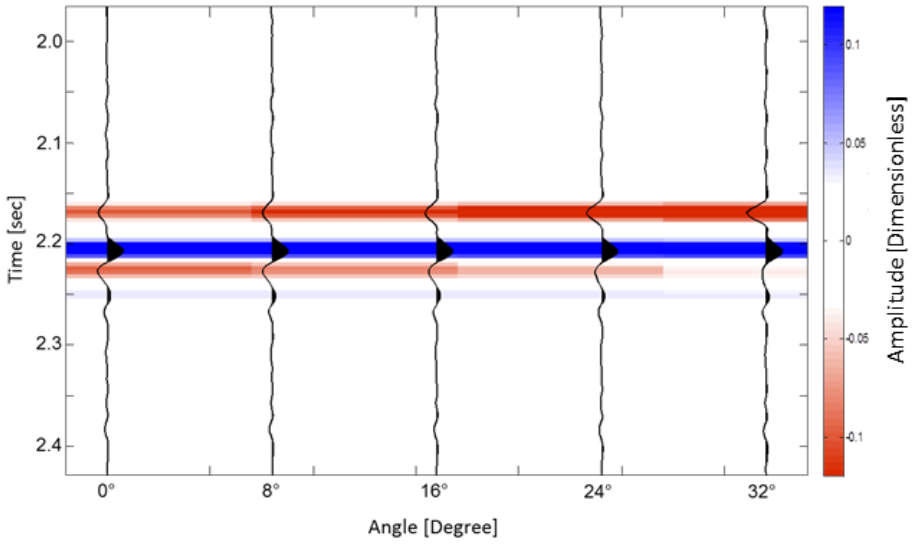

Figure 5.22: Synthetic angle gather generated from synthetic model 2.

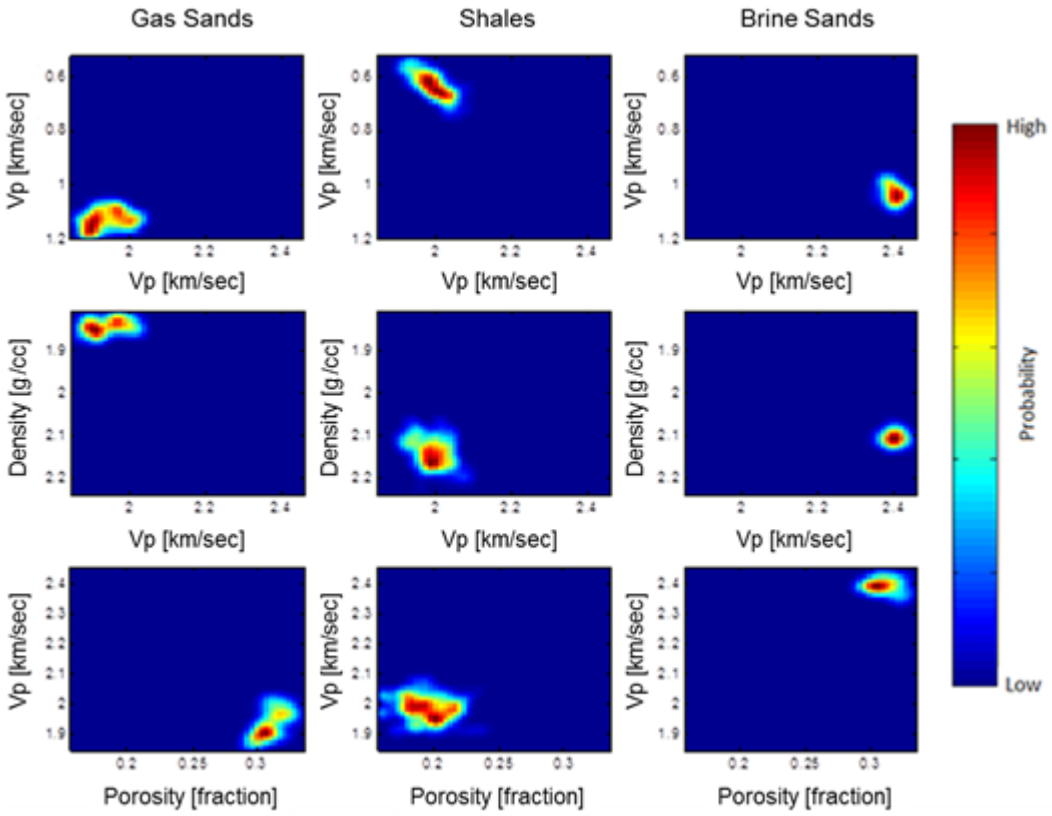

Figure 5.23: 2D Projections of the multivariate probability distribution function for gas sands (left), shales (center) and brine sands (right), calculated from synthetic model 2.

The inversion was five million realizations with the constraint that all brine samples should be above the deeper gas sample. This is important because we assumed a unique fluid contact in the whole interval; the models with L^2-norms smaller than 0.88 were selected as possible solutions for the inversion. The comparison between the synthetic model and the 664 obtained solutions (Figure 5.24) shows a close similarity between the synthetic input data and the inversion results. The waveform comparison for four inverted solutions and the synthetic model (Figure 5.25) demonstrate that the main events are well reproduced by the inversion algorithm.

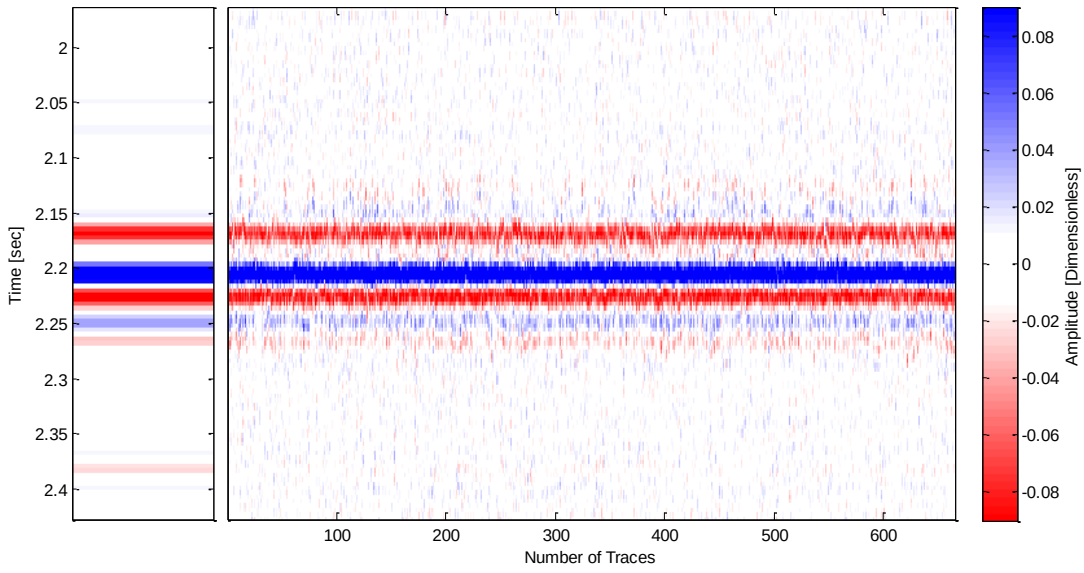

Figure 5.24: Real seismic trace (left) and possible models traces (right) comparison. The selected traces have L^2-norms smaller than 0.88.

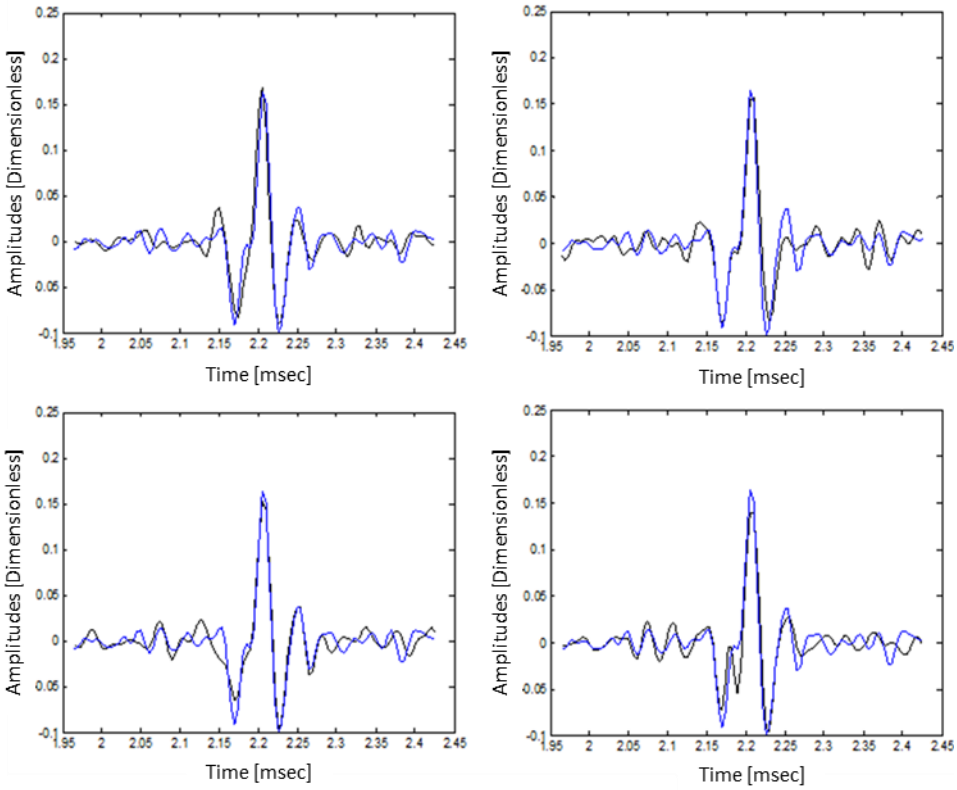

Figure 5.25: Synthetic versus modeled waveform comparison for four possible models with $\alpha<0.88$.

The seismic lithofacies distributions for the 664 solutions are shown in Figure 5.26. A visual inspection of the seismic lithofacies distributions shows a large consistency for the depth of the top of the sand, fluid contact and base of the sand. We generated histograms of the depth of the three seismic lithofacies interfaces to evaluate the accuracy of the proposed inversion scheme (Figure 5.27).

Table 5.1 shows the comparison between the synthetic data and the depths obtained by the inversion; these results demonstrate that the inversion scheme is very accurate.

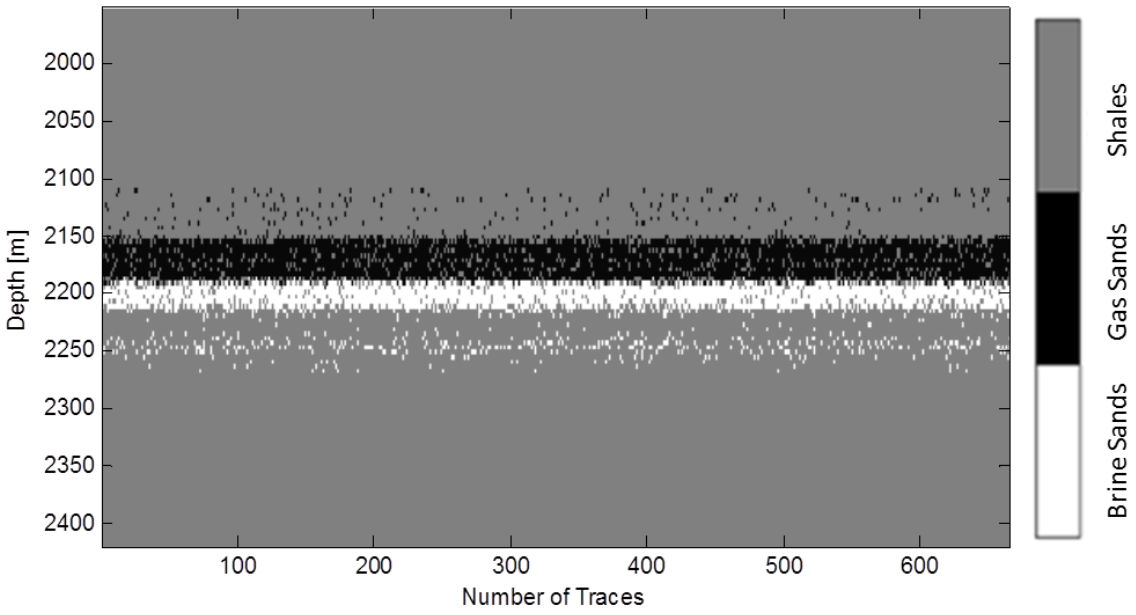

Figure 5.26: Probable models with α<0.88. The green, black and white represent the shales, gas sands and brine sandstone seismic lithofacies, respectively.

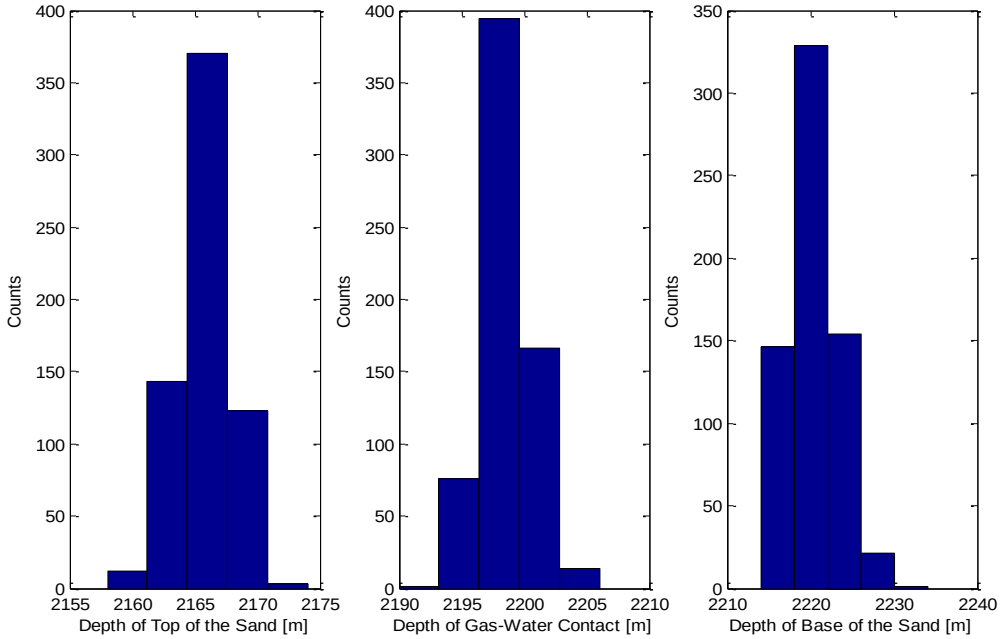

Figure 5.27: Depth of top of the sand (left), gas-water contact (center) and base of the sand (right) histograms.

Table 5.1: Comparison between the synthetic data and the depths obtained by the inversion.

	Top of Sand	Gas-Water Contact	Base of Sand
Synthetic Model Value [m]	2166.00	2202.00	2222.00
Mean [m]	2165.80	2198.70	2222.30
Median [m]	2166.00	2198.00	2222.00
Standard Deviation	2.82	2.63	3.21
Variance	7.97	6.92	10.34

Figures 5.28 to 5.31 show total porosity, shale volume, and effective porosity, respectively. The effective porosity was calculated from the total porosity and volume of shale properties. The elastic property solutions are shown in figure 5.32. The fluid contact is easily observed in all the elastic models.

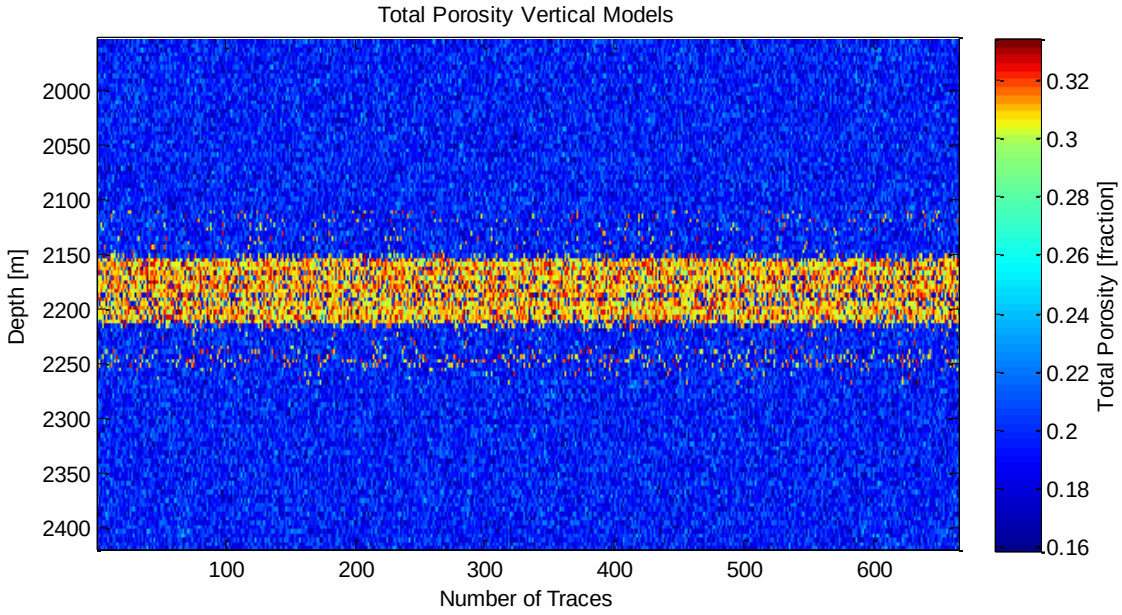

Figure 5.28: Total porosity of the probable models with α<0.88.

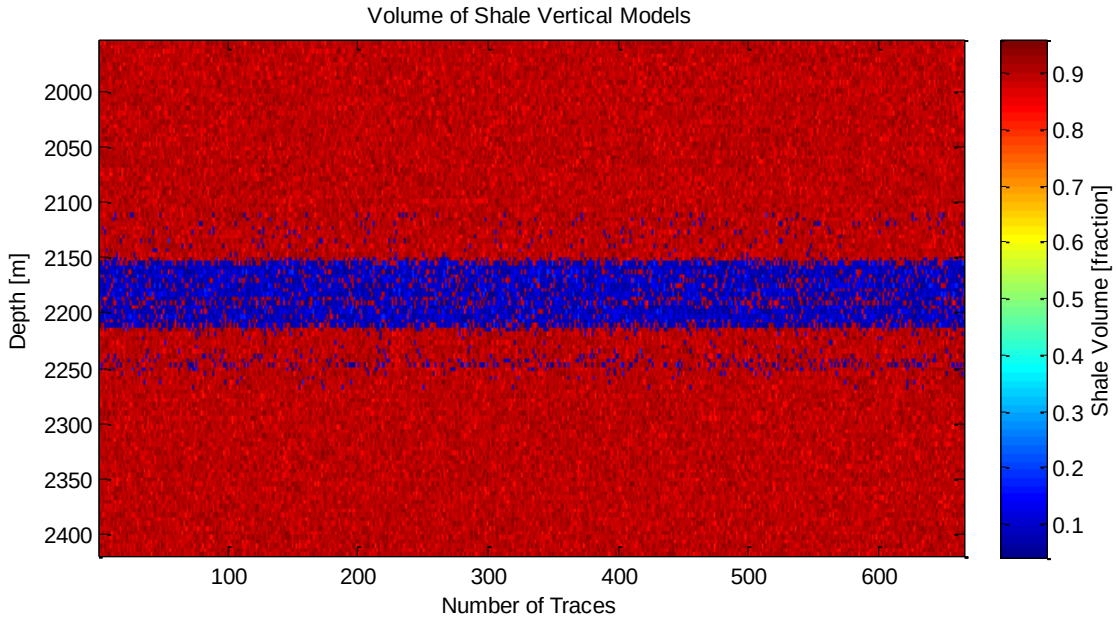

Figure 5.29: Volume of shale probable models with α<0.88.

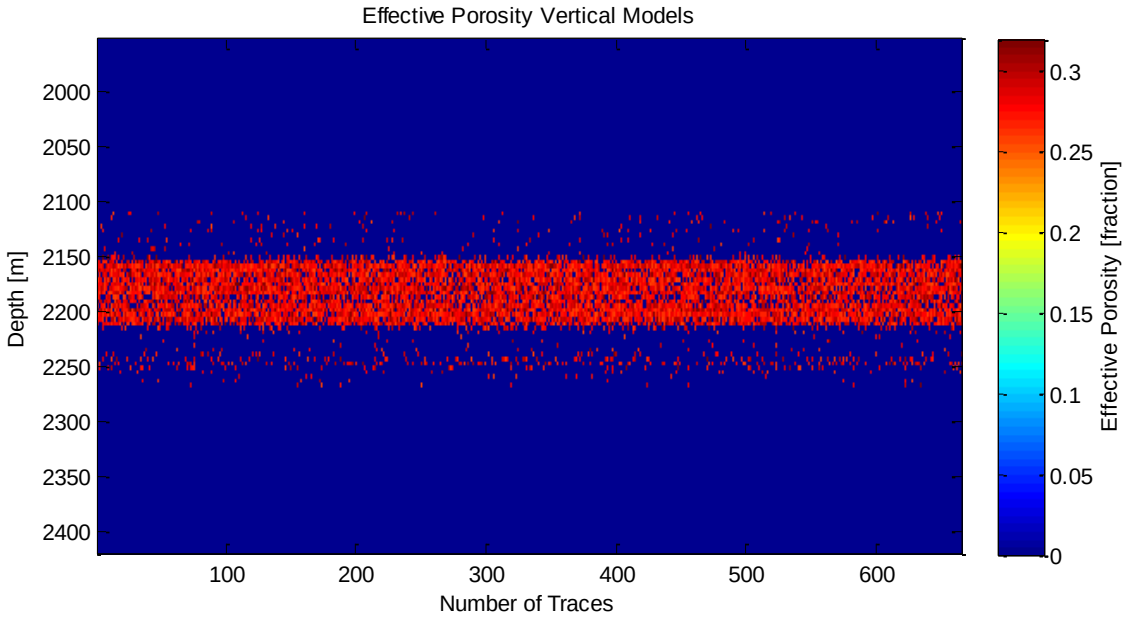

Figure 5.30: Effective porosity probable models with α<0.88 calculated from the total porosity and shale volume properties.

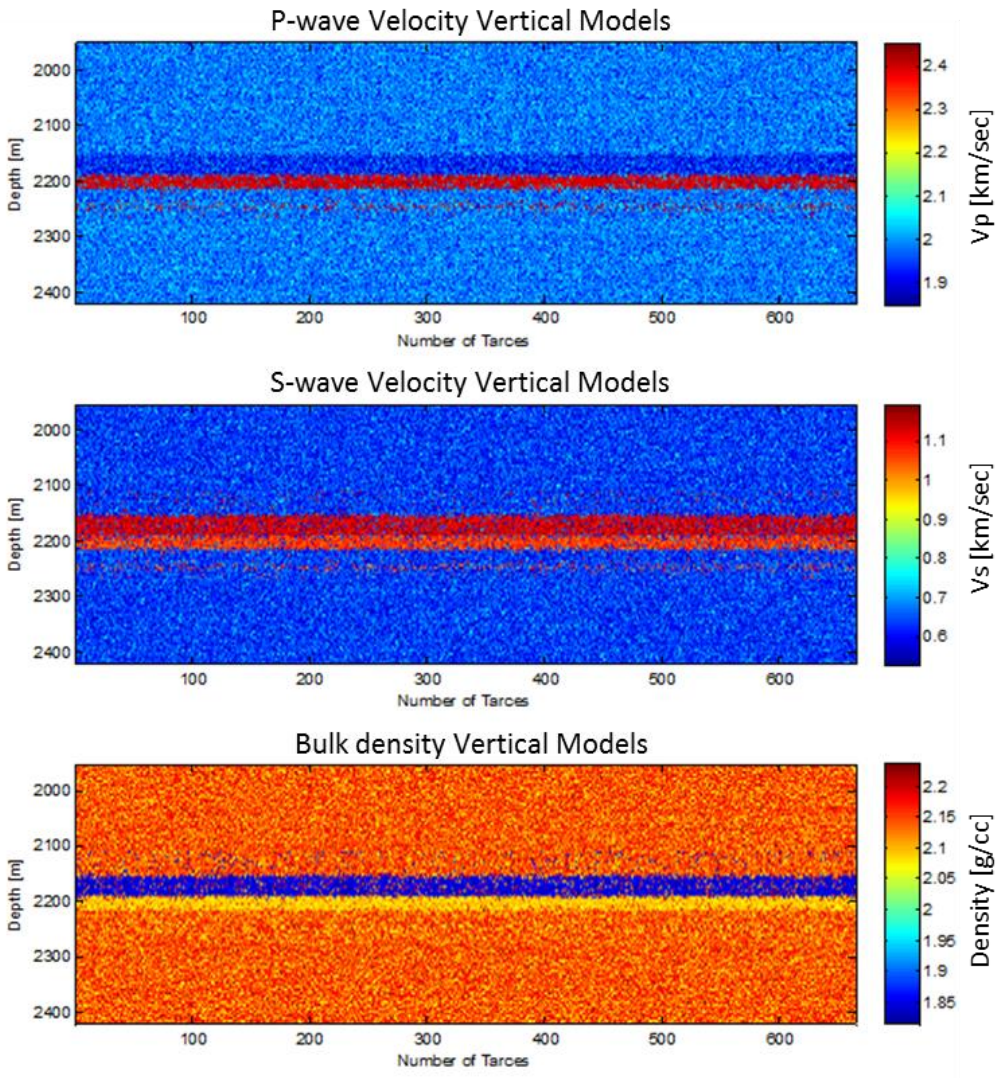

Figure 5.31: Elastic models with α<0.88.

5.4. Conclusions

The synthetic test results presented in this chapter demonstrate the feasibility of the estimation of rock properties by our proposed probabilistic inversion approach. The first example showed the capability of the novel

inversion scheme to estimate two critical rock properties for hydrocarbon exploration: porosity and reservoir fraction.

The second synthetic test included the fluid prediction as an additional rock property to be estimated by the inversion. The outcome demonstrated that the gas-filled sandstone can be easily discriminated from the shales and brine-saturated seismic lithofacies. We also showed the accuracy of the method in the estimation of the depth of the seismic lithofacies interfaces.

In conclusion, the results of these synthetic tests proved the feasibility of using the proposed stochastic inversion technique to calculate the properties of seismic lithofacies based on multivariate probabilistic rock physics models, reflection seismic data, using Markov Chain Monte Carlos Simulation (MCMCS) to sample the model space.

6. 1D REAL DATA APPLICATION

6.1. Introduction

This chapter presents the application of our proposed seismic stochastic inversion algorithm to a real data set. The data set includes a group of well logs and a 2D line of prestack seismic data extracted from a 3D volume crossing the exploratory well. The studied stratigraphic sequence corresponds to tertiary marine sediments deposited on a platform margin. From well-log data and the geological information, we identified two main lithologies: sandstones and shales. The potential reservoirs are unconsolidated sandstones with total porosity that ranges from 35% to 39%.The pore space can be filled by gas, low saturation gas (LSGS) or brine. Each combination of fluid and lithology is considered an independent seismic lithofacies. Therefore, the target interval is made up of four seismic lithofacies: shales, gas-filled sands, low saturation gas sands (LSGS) and brine sands. Figure 6.1 shows the *in situ* saturation logs for the two hundred and twenty meter study interval. The target interval has two sands: the upper sand is interceded with total thickness of twenty meters and a sand fraction of 73%; the lower reservoir is eighty meters of blocky sand with three fluid faces: gas, LSGS and brine.

The seismic data included raw PSTM gathers with a time sampling of 2 msec. The near angle stack generated from 0° to 15° is shown in Figure 6.2; the top of the strong seismic anomaly related to the top of the gas reservoir is

represented by large negative seismic amplitude. The top of the upper and lower sands are located at 72 ms and 104 ms, respectively. The goal of this inversion was to predict total porosity, volume of shale, effective porosity, and fluid type distribution in the study interval.

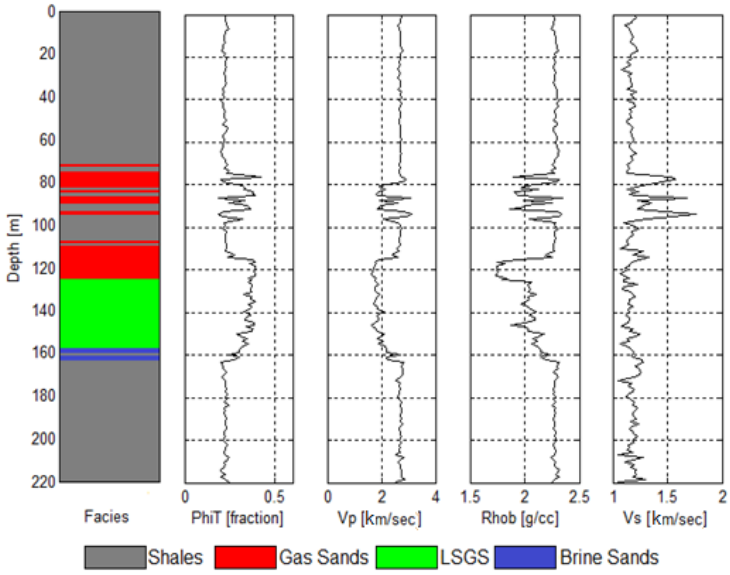

Figure 6.1: Well 1 logs for *in situ* saturation.

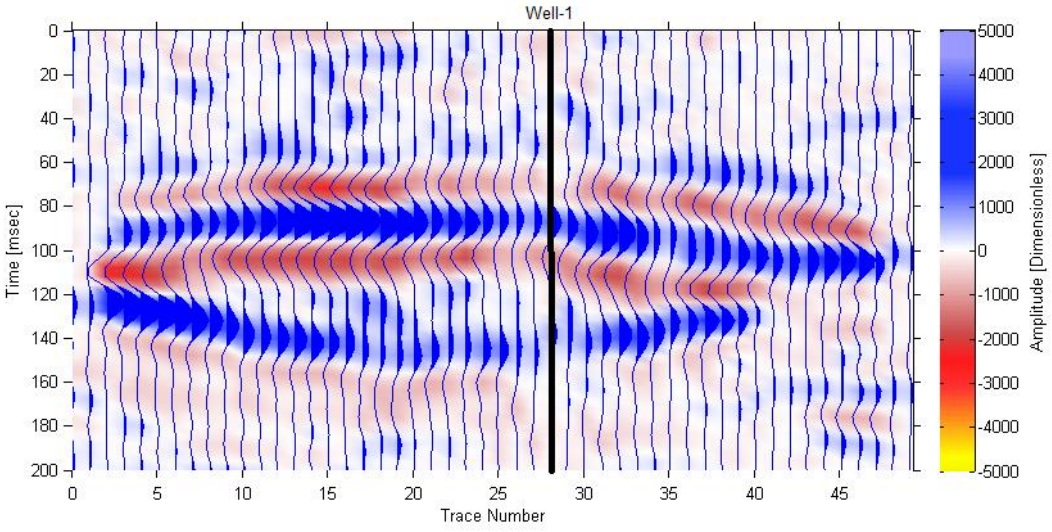

Figure 6.2: Near angle stack; the top of the upper and lower sands are located at 72 ms and 104 ms, respectively.

6.2. Seismic Data Conditioning

The prestack seismic data were conditioned to remove residual coherent noise and to improve the signal-to-noise ratio for the stochastic seismic inversion. This was an important stage, since the forward modeling operator assumed that all the reflections corresponded to primary reflections and random noise, and no coherent noise was present in the seismic data. The seismic data was also resampled to one millisecond to match the time sampling of the synthetic models. The angle gather at Well-1 location is displayed in Figure 6.3; the amplitude extraction at the top of the upper sand shows a strong AVO effect associated with the top of the gas sand.

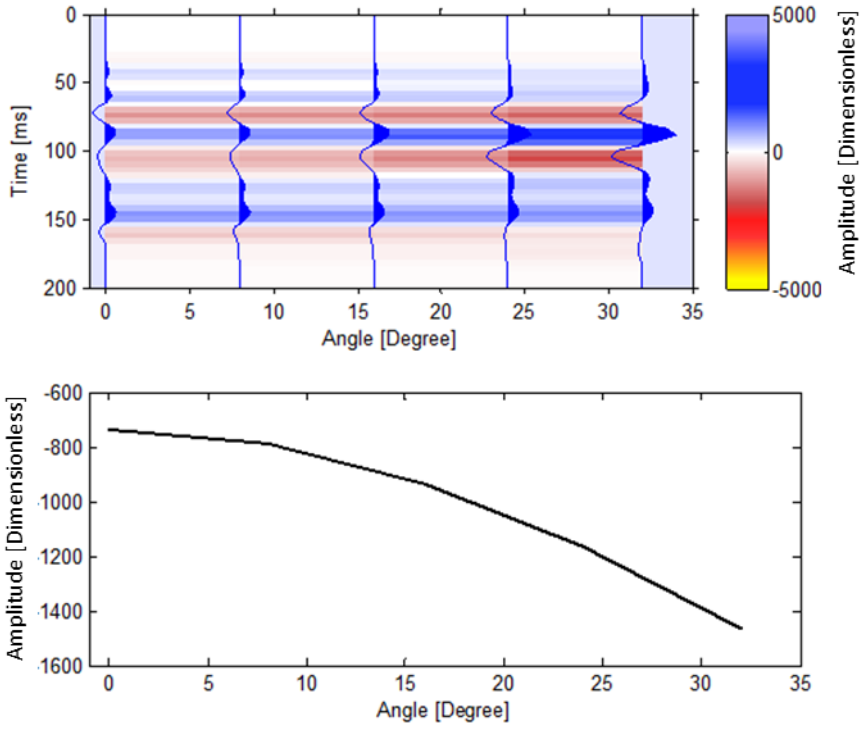

Figure 6.3: Angle gather at the Well-1 location (Upper). The amplitude extraction at the top of the upper sand shows a strong AVO effect (Lower).

After the seismic data was conditioned and converted to angle gathers, the well logs were converted to time and the well-to-seismic tie was performed (Figure 6.4). The well log tie shows close similarity between the zero offset trace and the acoustic synthetic trace (right track). The angle-dependent extracted wavelets are shown in Figure 6.5. The L^2-norm calculated from the real and synthetic traces is $\alpha=0.88$. Therefore, we assumed that any inversion solution with $\alpha \leq 0.88$ was a possible solution to the studied real data application.

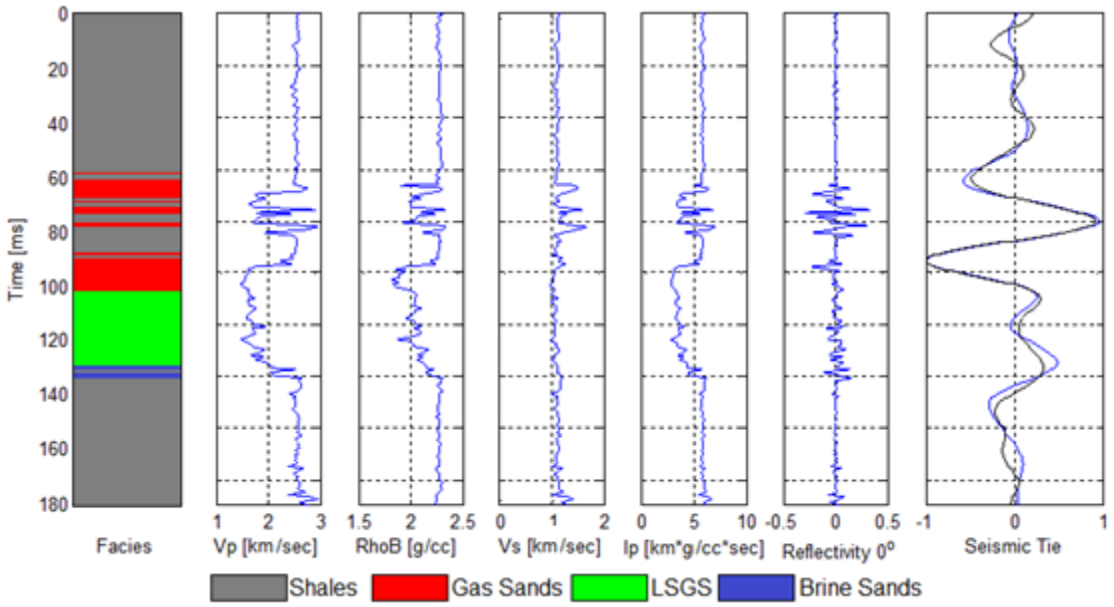

Figure 6.4: Well logs converted to time showing the well to seismic tie (right track); the black line corresponds to the measured seismic trace and blue the synthetic seismogram.

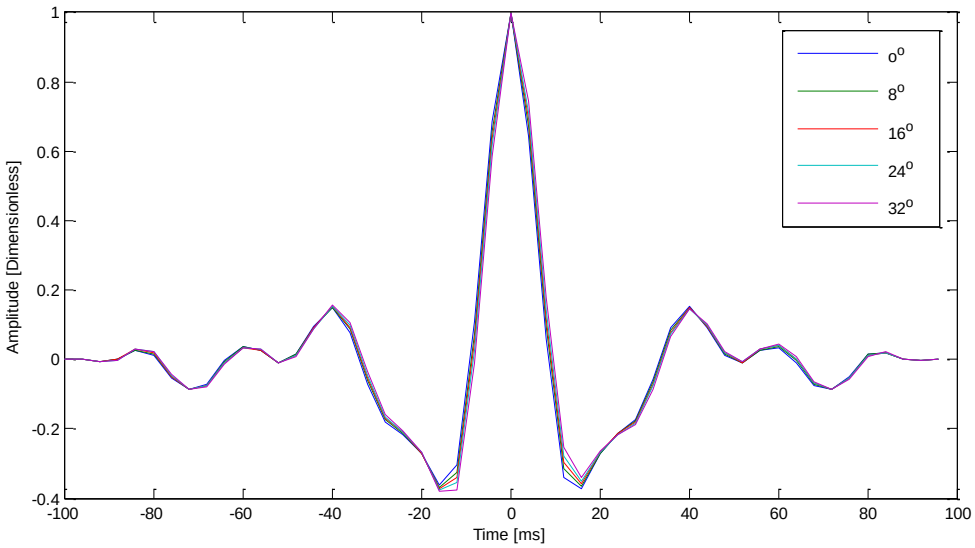

Figure 6.5: Angle-dependent extracted wavelets.

6.3. The Model Space Generation

The available well-log information was used to generate the multivariate PDF for the four observed seismic lithofacies: shale, gas sand, low gas saturation sand and brine sand. Fluid replacement based on Gassmann's relation was performed to better understand the effect of fluid variations in the target reservoir sands. Figure 6.6 shows the well logs for the *in situ*, 90% gas, and 100% brine-saturated sands.

The 2D projections of the multivariate PDF (Figure 6.7) show the feasibility of discriminating most of the seismic lithofacies groups based on their elastic properties. Only the low saturation gas sands cannot be easily discriminated from gas sands.

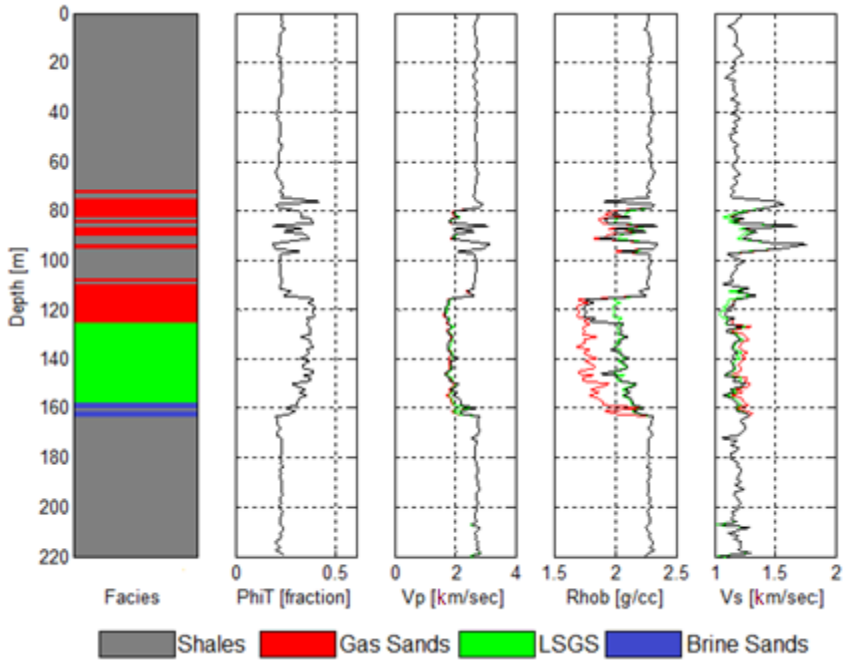

Figure 6.6: Well 1 logs after fluid substitution. Black, red and blue lines correspond to *in situ*, 90% gas and 100% brine-saturated sands.

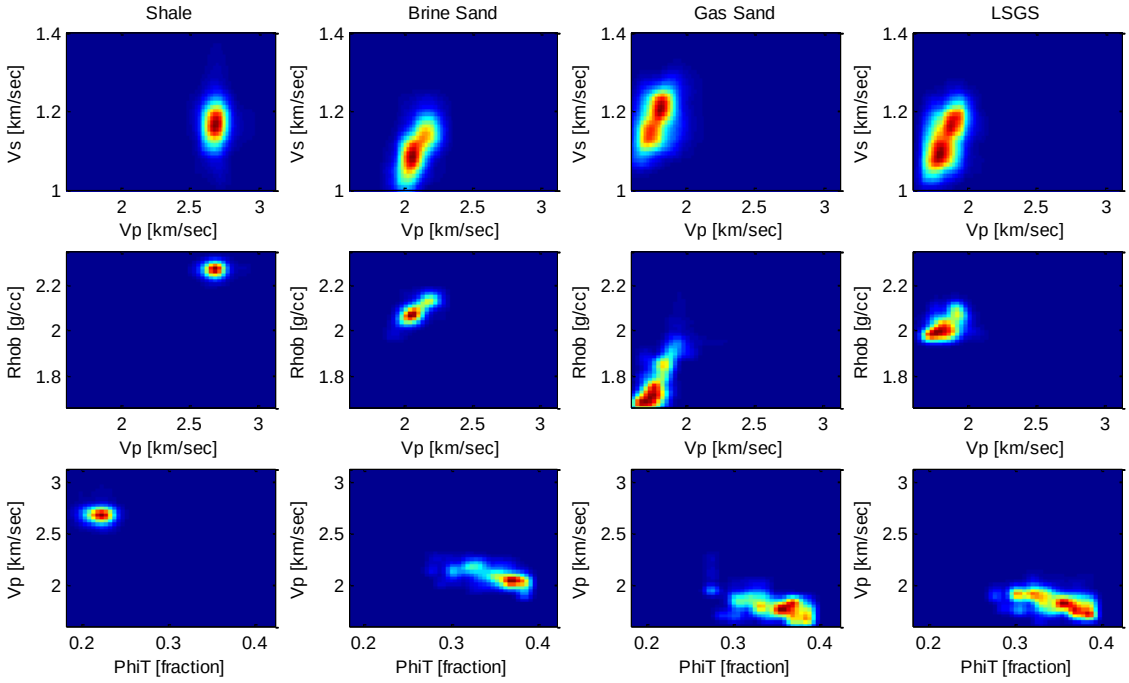

Figure 6.7: 2D Projections of the multivariate probability distribution function generated from Well 1 log data and Gassmann fluid substitution.

6.4. The Seismic Stochastic Inversion

The rock property models were generated assuming that all gas samples were located above the low saturation gas sands and all LSGS were situated above the brine sand. The fluid contacts can be situated at any depth as long as the order of the fluid interfaces is followed. The properties of the seismic lithofacies were assigned from the multivariate PDFs by using the MCMCS engine to sample them. The proposed inversion algorithm generated data in two domains; the first is the rock physics simulation domain that is generated in depth. The second was the forward-modeling domain that was built in two-way travel time. For this real data application, the vertical sampling of the rock physics simulation grid (depth) was fixed to one meter and the two-ways travel time sampling for the forward model grid was set to one millisecond. The depth and time grids were selected to minimize the resampling effect on the well-log data.

Five million realizations were performed and 320 models with normalized $\alpha \leq 0.88$ were selected. The comparison between the real traces and the 320 solutions for 0° and 32° incident angles are shown in Figure 6.8.

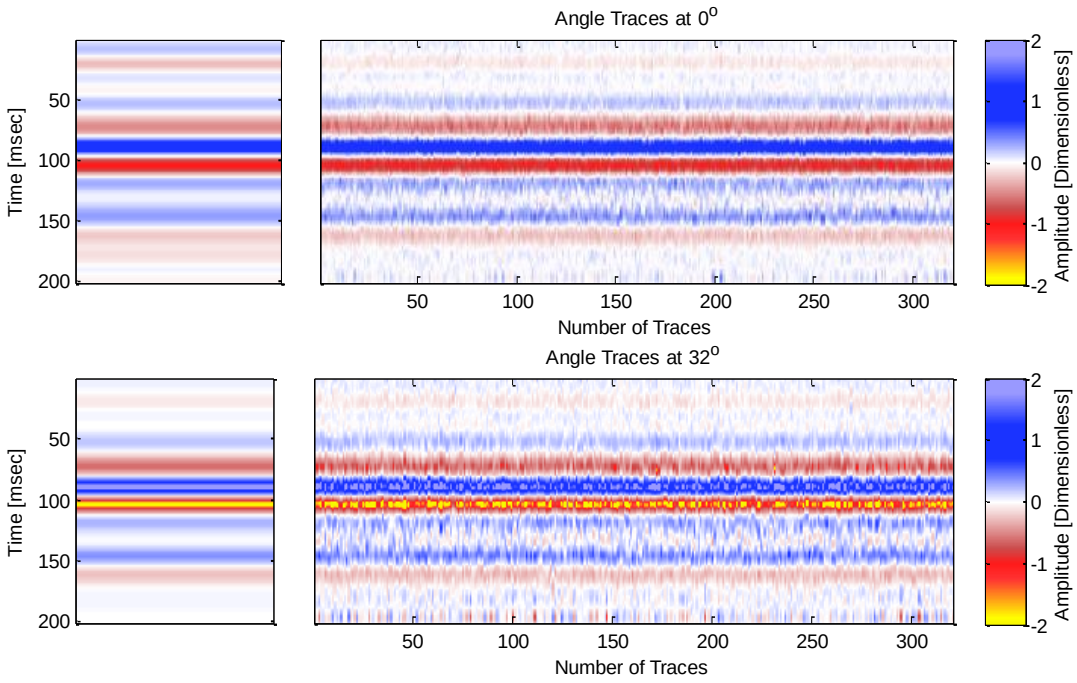

Figure 6.8: Comparison between real angle traces (upper and lower left) and the 320 solutions for 0° (upper right) and 32° (lower right) incident angles.

Figure 6.9 shows that the similarity among the traces is large enough to assume that all of 320 model traces were generated from probable geological models. The upper and lower sands are well-delimited by most of the probable inversion solutions. However, the gas-LSGS fluid contact can be located at any depth because of the impossibility of elastically discriminating between gas and low saturation gas sands. The possible models plot shows that all the possible solutions for the LSGS-brine sand fluid contact have the fluid interface located in the lower sand. In fact, most solutions have the fluid contact situated more than 20 meters below the top of the lower sand.

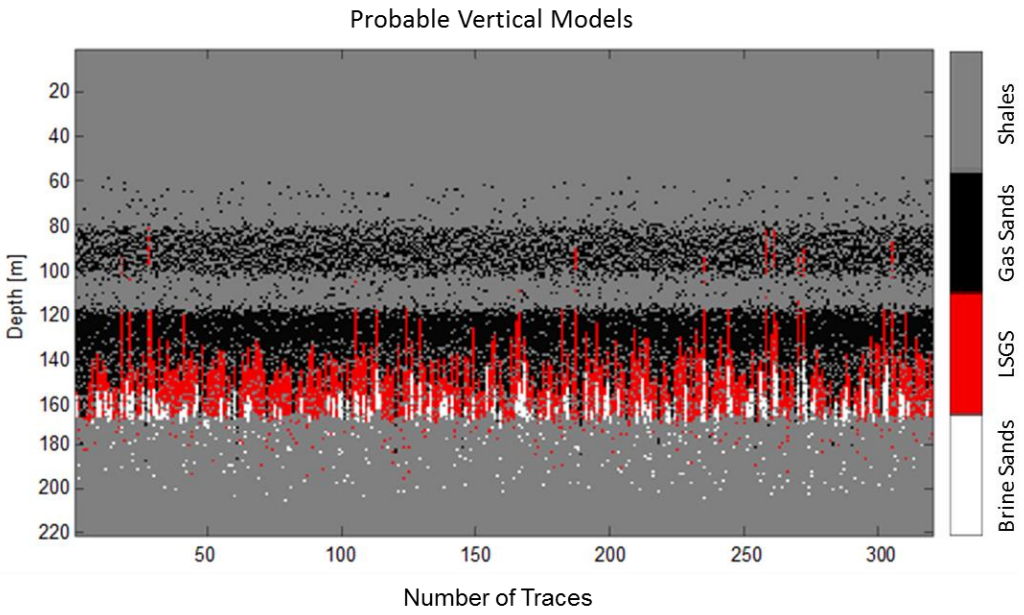

Figure 6.9: Probable models with α≤0.88. Grey, black and white represent shales, gas sands and low saturation gas sands, respectively.

We are interested in the prediction of total porosity, shale volume, and effective porosity prediction from the seismic inversion, as has been mentioned. Figures 6.10, 6.11 and 6.12 show the total porosity, volume of shale, and effective porosity for the 320 solutions. The elastic models shown in Figure 6.13 demonstrate that there are almost no differences in the elastic properties of the gas sands and low saturation gas sands. In fact, the main differences are found in the density rather than in the elastic moduli.

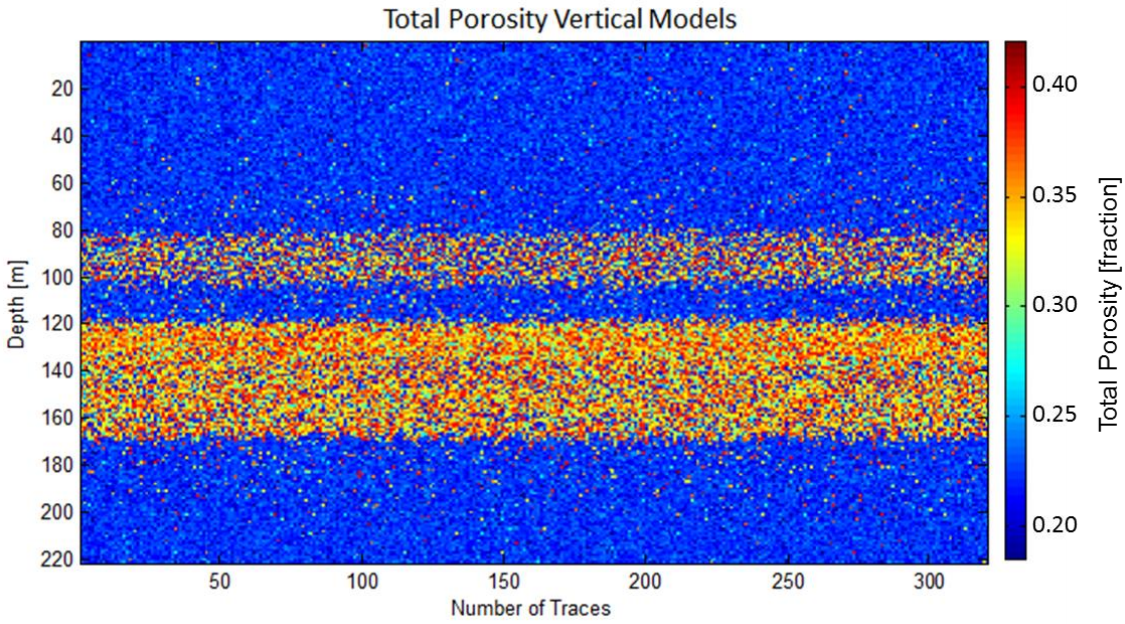

Figure 6.10: Total porosity of the 320 probable models.

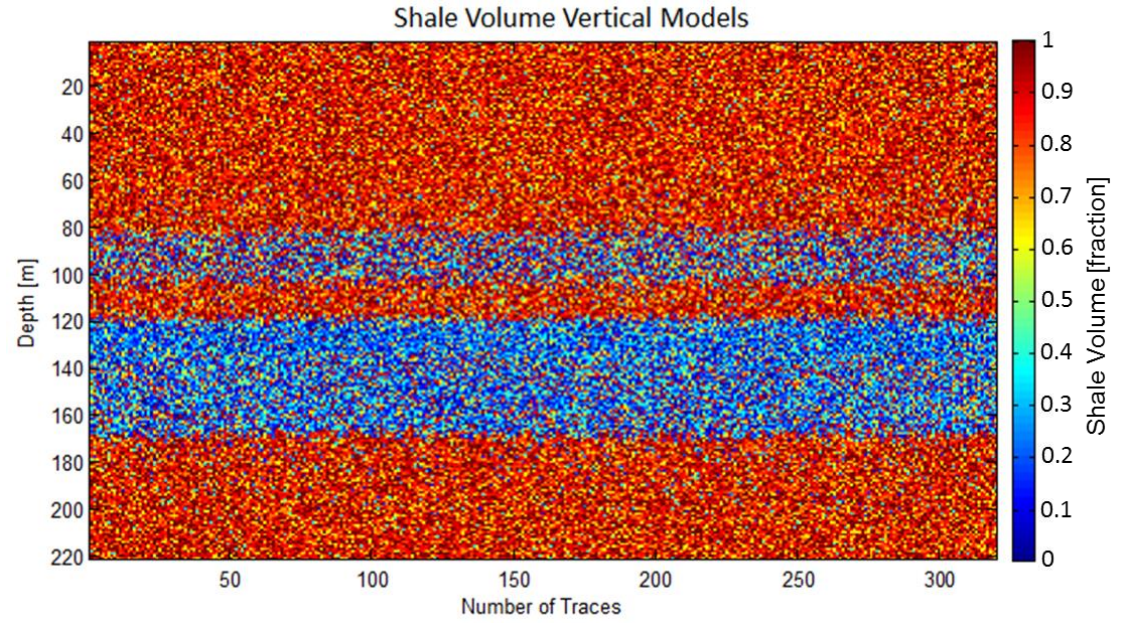

Figure 6.11: Volume of shale of the 320 probable models.

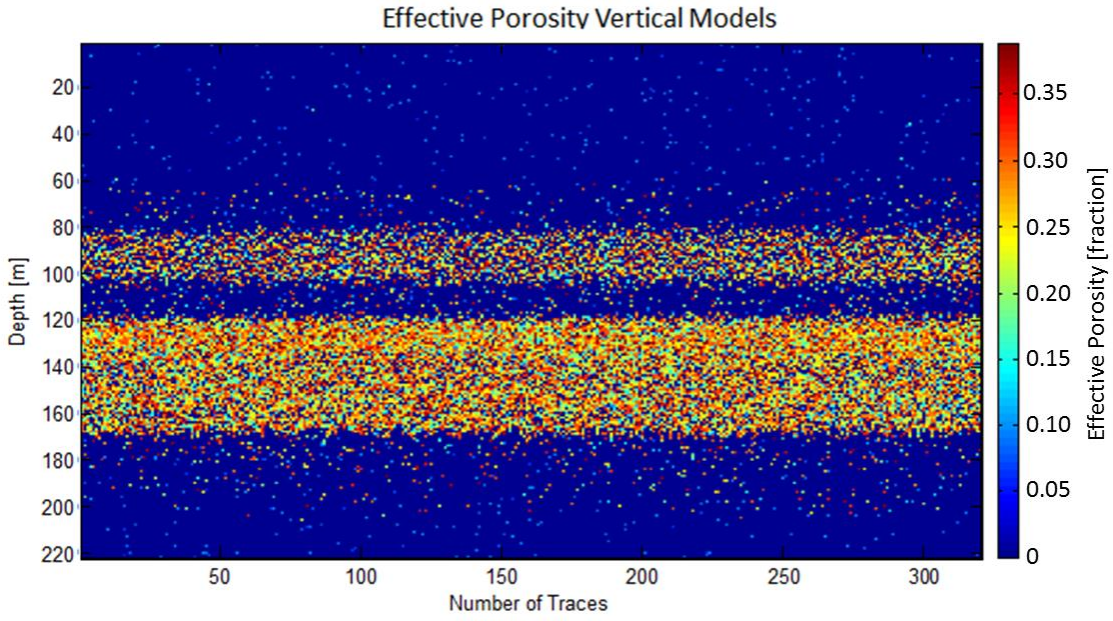

Figure 6.12: Effective porosity of the 320 probable models.

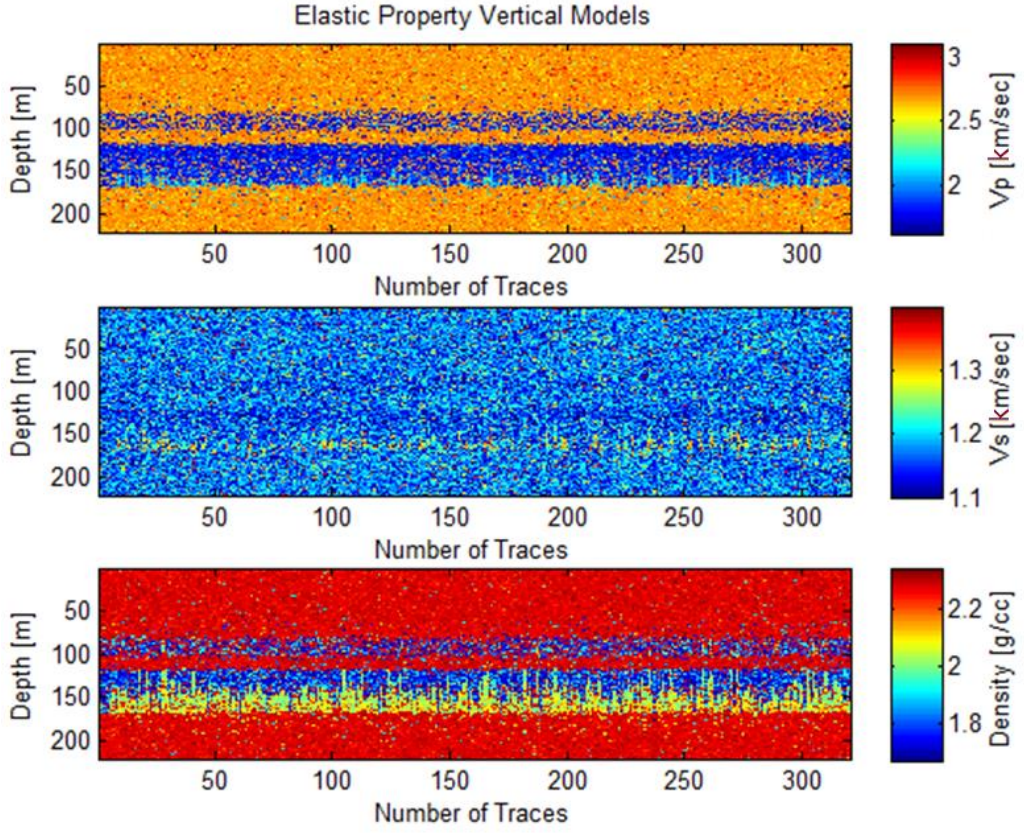

Figure 6.13: Possible elastic models with α≤0.88.

6.5. Analysis

The combination of the probable models for the target zone was used for the analysis of rock properties. Figure 6.14 shows the probability of the sand plot; larger values mean higher possibility of having a sand sample at a given depth. It can be observed that the upper sand has less probability than the lower sand, due to its sand/shale interbedded geometry. We can assume any probability cutoff to define the most probable sand/shale geometry; however, it is important to mention that the larger the cutoff the smaller the sand fraction in the analyzed interval; we chose a conservative value of 0.2 as the threshold for this real data set. The comparison between the real and the estimated top values for probability equal to or larger than 0.2 is shown in table 6.1. The comparison confirms the accuracy of our proposed inversion scheme for lithology prediction.

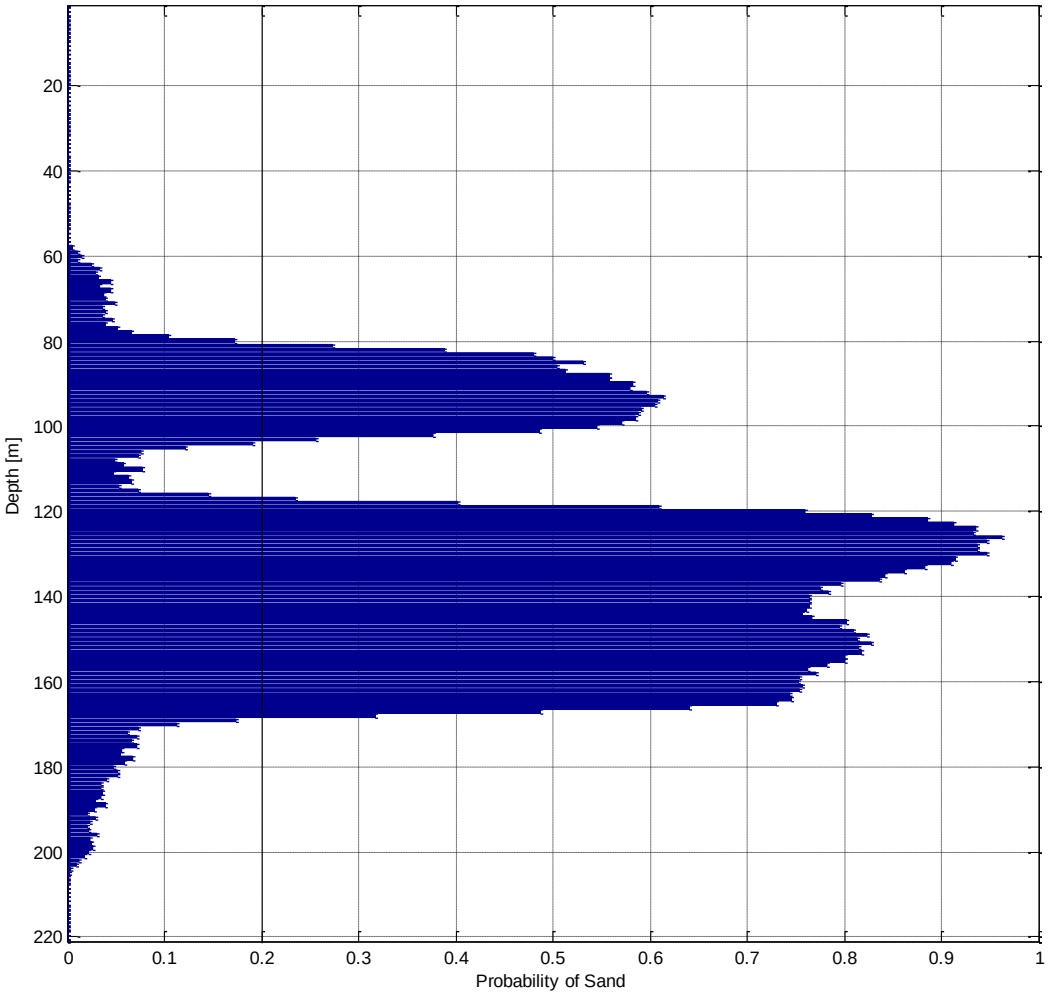

Figure 6.14: Probability of sand vertical plot.

Table 6.1: Comparison between the real and the estimated lithology top values for probability larger than 0.2.

	Inverted Tops [m]	**Real Tops [m]**
Top Upper Sand	80	79
Base of Upper Sand	103	98
Top Lower Sand	116	114
Base of Lower Sand	176	181

Based on the inversion solutions for total porosity and effective porosity, we generated the most probable vertical plot for both rock properties (Figure 6.15). The comparison shows that the inverted porosities underestimated the larger porosity values and overestimated the lower observed well log porosity. This smoothing effect is stronger in the upper sand where extreme property values are further apart.

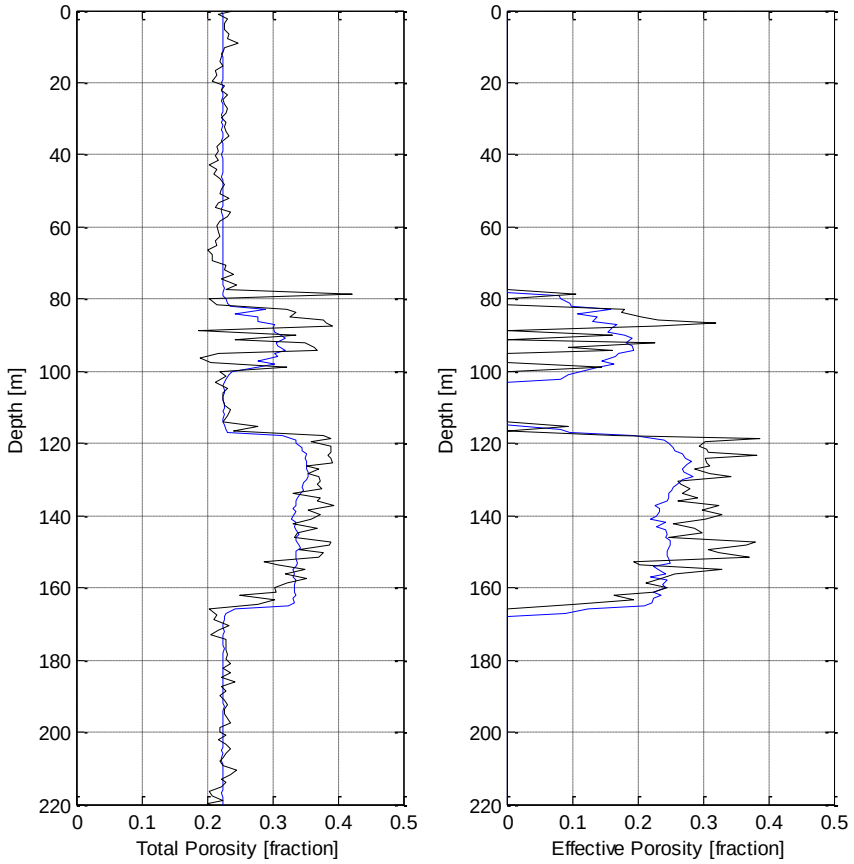

Figure 6.15: Total porosity and effective porosity comparison. The black lines correspond to the well log information and the blue lines to the inverted rock properties.

The most-likely fluid geometry (Figure 6.16) was generated from the 320 probable models section (Figure 6.9) and constrained by the most expected sand profile (Figure 6.14). The comparison between the real fluid interfaces and the inverted fluid contact depths (Table 6.2) shows a surprisingly close agreement with the well data.

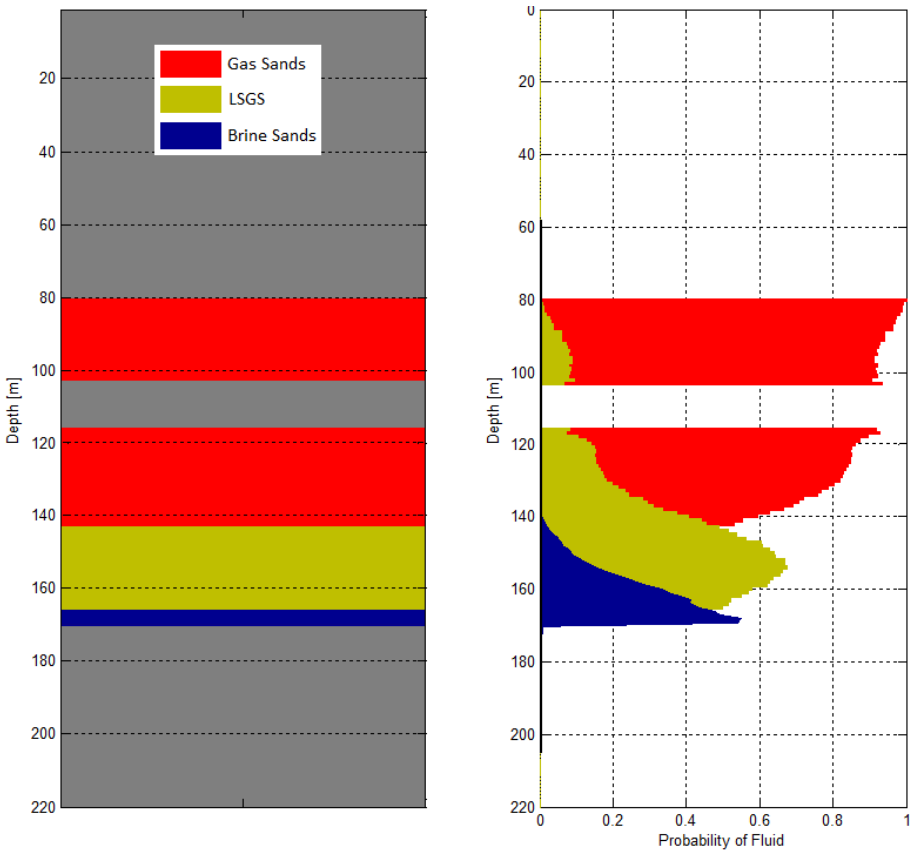

Figure 6.16: Most expected fluid seismic lithofacies (left) and probability of fluid type (right).

Table 6.2: Comparison between the real and the estimated fluid contact depths.

	Inverted Contacts [m]	Real Contacts [m]
Gas - LSGS Contact	143	147
LSGS - Brine	168	176

Finally, the elastic properties probable models generated from the stochastic inversion are compared with the Well-1 elastic logs in Figure 6.17. The results of the inversion are remarkable similar to the well log measured data. However, the S-wave velocity of the interbedded shales within the upper sand section was not well predicted. These shales have a very low Vp/Vs ratio compared to the rest of the shales.

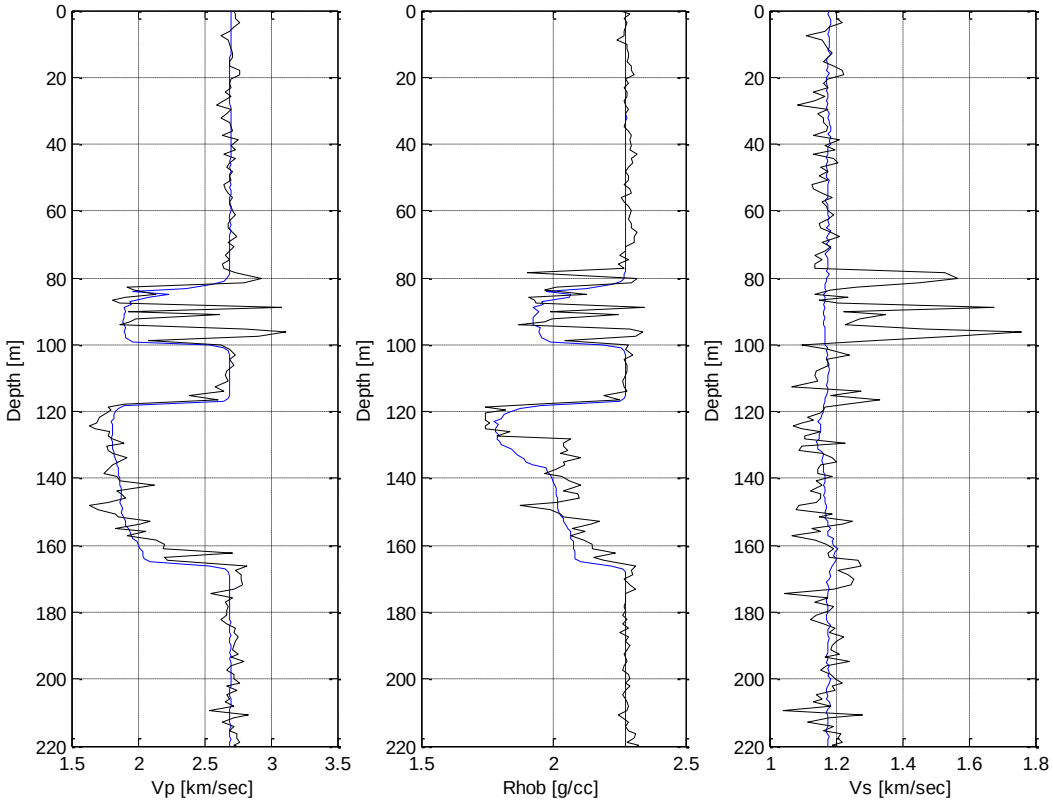

Figure 6.17: Comparison between the most expected elastic models (blue line) against well logs (black lines).

6.6. Conclusions

The outcomes of the 1D real data application of the proposed stochastic inversion are remarkable similar to the available well log measured data. It is important to emphasize that Well-1 was not used to constrain the inversion; it was only used to populate the model space. The mean of the inverted rock properties tends to be smoother than the measured values; in fact, the most expected inverted properties have a tendency to underestimate larger rock property values and overestimate lower property measurements. This 'smoothing' effect is stronger in layers where extreme property values are further apart. This effect is observed in all the estimated rock properties.

The S-wave velocity of the shale member of the interbedded upper sand was underestimated by the inversion; this suggests that an additional seismic lithofacies might be included in the model space. Finally, the proposed inversion approach demonstrates the viability of the integration seismic data, well log information, and rock physics models in a practical workflow to estimate rock properties for hydrocarbon exploration or development.

7. 3D REAL DATA APPLICATION

7.1. Introduction

In this chapter, we introduce the first 3D application of a real data set using the proposed inversion algorithm. The real data seismic inversion is performed using the same data set presented in the Chapter 6. The main difference between the 1D and 3D stochastic inversion algorithms is the use of geostatistics and well log data to constrain the outcomes.

In the first part of the chapter, we introduce some basic concepts of geostatistics that are used to create lateral continuity to the stochastic seismic inversion outcomes. The second part of the chapter shows the application of the proposed 3D stochastic inversion algorithm to the 2D line of prestack seismic data extracted from a 3D volume and supported by the Well-1 information. Finally, we discuss the convergence criteria and the efficiency of the proposed inversion algorithm.

7.2. The Kriging Estimator

Geostatistics is a set of mathematical tools used to describe the lateral continuity of natural phenomena. Geostatistics was originally developed to estimate probability distributions of mineral concentrations for mining prospecting. Classical geostatistics is strongly related to the Kriging interpolation algorithm (Isaaks and Srivastava, 1989). The Kriging algorithm is a family of

linear unbiased estimators that predict the value of a property in any given location by computing a weighted average of the observed values of the studied properties and their spatial distributions. All the Kriging algorithms assume that the observed data are the result of a random process; then the objective of the Kriging estimator is to minimize the error variance $\sigma_E^2(x)$.

The Kriging estimators are defined by the treatment of the trend component (mean). In this particular application, we used the Ordinary Kriging to include lateral continuity to the stochastic inversion. Ordinary Kriging assumes that the local mean may vary greatly over the studied area. In this case, the system of equations is:

$$\begin{cases} \sum_{\beta=1}^{n} \lambda_N^{OK}(u) C_R\left(u_{\alpha-}u_\beta\right) + \mu_{OK}(u) = C_R(u_{\alpha-}u) \\ \sum_{\beta=1}^{n} \lambda_\beta^{OK}(u) = 1 \qquad\qquad \alpha = 1, 2, 3, \dots, n(u) \end{cases}, \tag{7.1}$$

where:

u_α, u_β = Location vectors for known location,

u = Location of the unknown location,

$h = u_\alpha - u_\beta$,

$C_R(h)$ = Covariance function,

$\lambda_\alpha(u)$ = Kriging weight.

In general, the weight of each data point decreases with increasing distance to the location that is being estimated. The weights λ_α are calculated from the covariance function that is generally derived from the semivariogram

model. The semivariogram model is a function that describes the degree of spatial dependence of the target property. It is defined as the variance of the difference between known values at two locations across the target area. The Kriging estimator needs valid semivariogram models to compute the covariance at any distance *h*. In isotropic environments, the correlation between the spatial process at two point pairs p1 and p2 only depends on the separation distance *h* and not on the orientation of the two points. However, real data often show directional effects. Particularly in geologic applications, measurements along a particular direction may be highly correlated, while the perpendicular direction shows little or no correlation. This phenomenon is known as anisotropy.

There are two types of anisotropy. The simplest type occurs when the covariance form is the same in all directions but the range *S* changes. In this case, there is a single sill, but the semivariogram reaches the sill in a shorter lag distance along a certain direction. In anisotropic settings *h* can be estimated using the following relation:

$$h = \begin{pmatrix} cos\alpha & sin\alpha \\ -sin\alpha/R & con\alpha/R \end{pmatrix}, \tag{7.2}$$

where *R* is the ratio of between the larger $r^1$and the lower seal r^2:

$$R = \frac{r^2}{r^1}\,. \tag{7.3}$$

In this real data application we use a spherical semivariogram to estimate the Ordinary Kriging weights. The spherical semivariograms are defined as:

$$\gamma(h) = 1.5\left(\frac{h}{a}\right) - 0.5\left(\frac{h}{a}\right)^3, \quad (7.4)$$

where *h* is the distance vector and *a* is a fitting constant defined from the observed data.

7.3. 3D Real Data Application

As has been mentioned before, the 3D application integrates the 1-D stochastic inversion algorithm with a Kriging engine to produce the lateral constraint rock properties model. Figure 7.1 shows the simplified stochastic inversion algorithm; the inversion scheme includes an additional choice to select between the Markov Chain simulation for rock properties or the geostatistical estimation of rock properties. In this real test we inverted the 50 traces that constitute the 2D seismic line (Figure 6.2) using the Well-1 as initial well data and the statistical rock physics model shown. To estimate the covariance we used an anisotropic spherical semivariogram with a 0.1 nugget, a sill of 0.9 and ranges of 500 meters and 50 meters in horizontal and vertical directions respectively (Figure 7.2). We chose the horizontal range as the maximum distance to accept a trace for the geostastistical estimation of the rock properties.

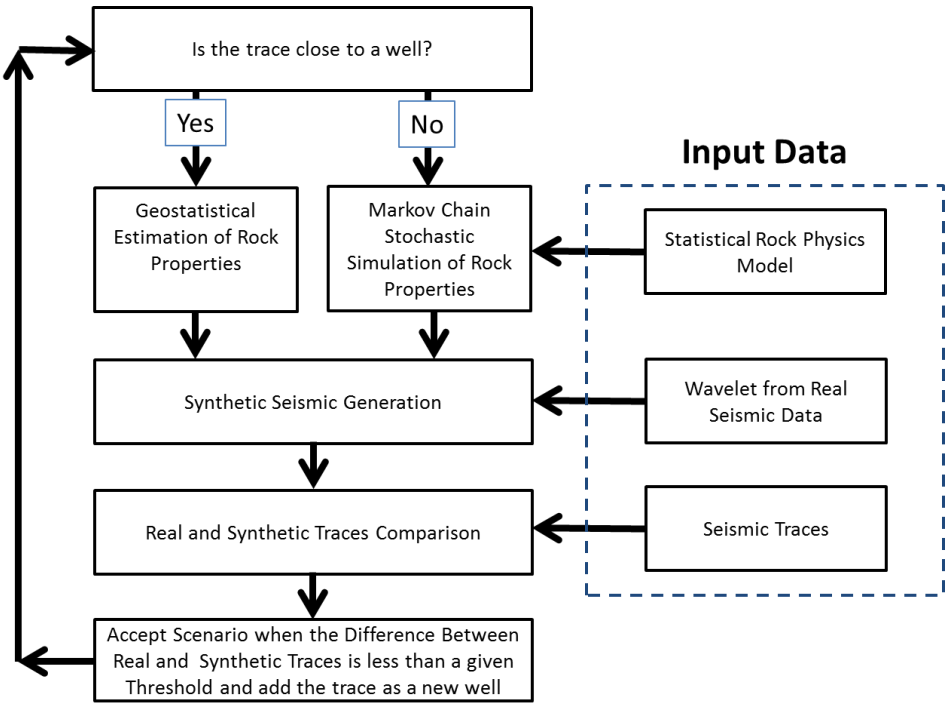

Figure 7.1: Simplified 3D stochastic inversion workflow.

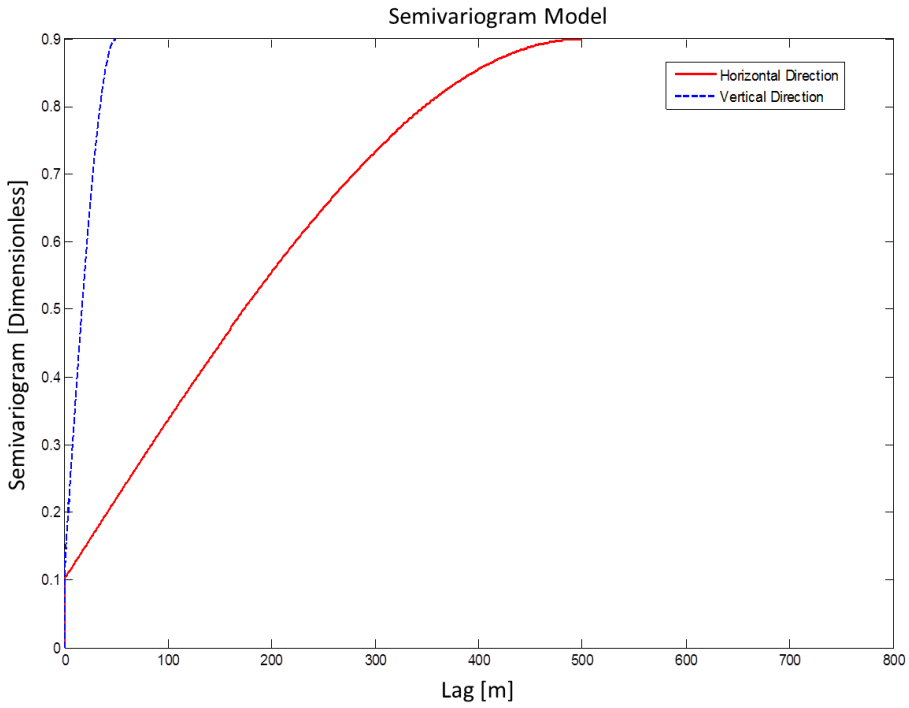

Figure 7.2: Anisotropic semivariogram model with a 0.1 nugget, a sill of 0.9 and ranges of 500 meters and 50 meters.

Figure 7.3 shows the evolution of the variance model for one of the stochastic simulation outcomes. The order selection of the seismic traces plays an important role in the stochastic inversion process. To assure a random selection of the trace's order we implemented the Fisher and Yates shuffle algorithm supported by a Markov Chain for each stochastic realization. Therefore, any trace selection path should be independent from the previous realizations. The upper section of Figure 7.3 shows the initial variance model, it is clear that the closer to the Well-1 the smaller the variance. The lower variance values are situated at the well location where the variance becomes zero. The second, third and fourth sections (from top to bottom) represent three more iterations that produced three new wells. Every new iteration reduced the variance model (reducing the uncertainty) until the variance model was zero at the fiftieth iteration.

The inversion was performed for the four seismic lithofacies defined in Chapter 6: shales, gas sands, LSGS and brine sands. Figure 7.4 shows three possible models generated by the proposed inversion algorithm. The total porosity, volume of shale, P-wave velocity, bulk density and S-wave velocity inversion outcomes are shown in figures 7.5 to 7.9, respectively. All the shown models are probable and similar. However, they have small variations in the depth of the seismic lithofacies interfaces, especially, in the gas sands and LSGS interfaces where the impedance contrast is very small.

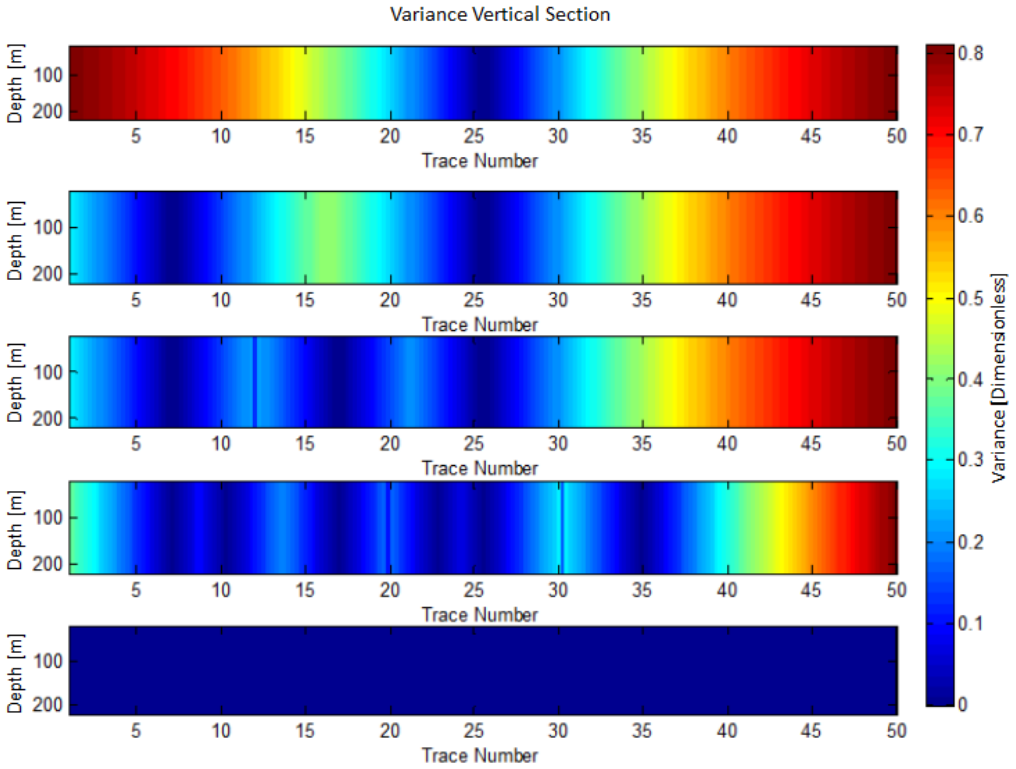

Figure 7.3: Variance model evolution for one of the stochastic simulation outcomes.

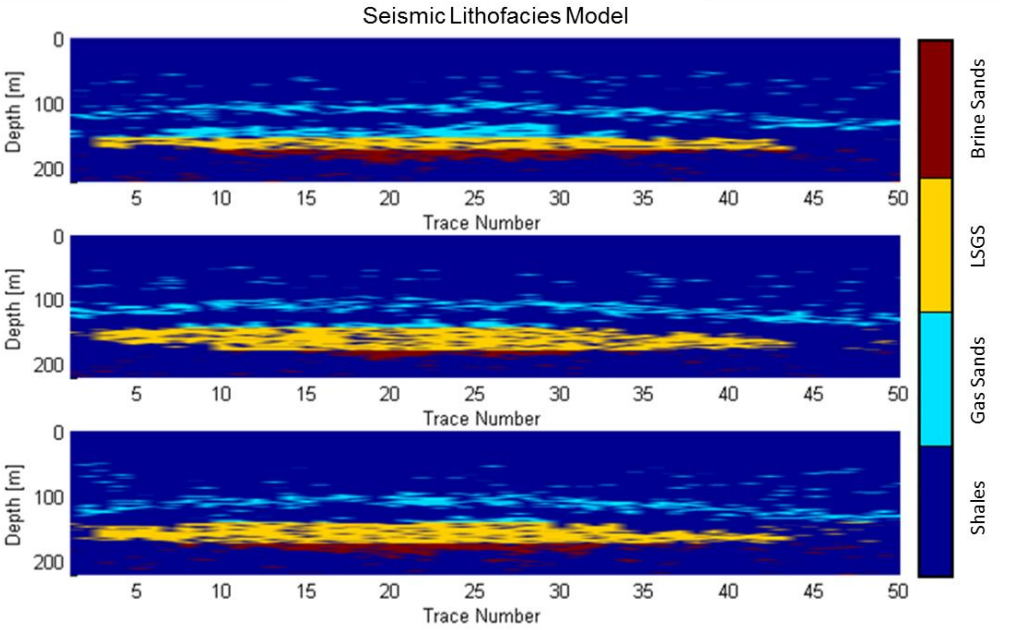

Figure 7.4: Three possible stochastic models. Shales are represented by facies 1, gas sands by facies 2, LSGS by facies 3 and brine sands by facies 4.

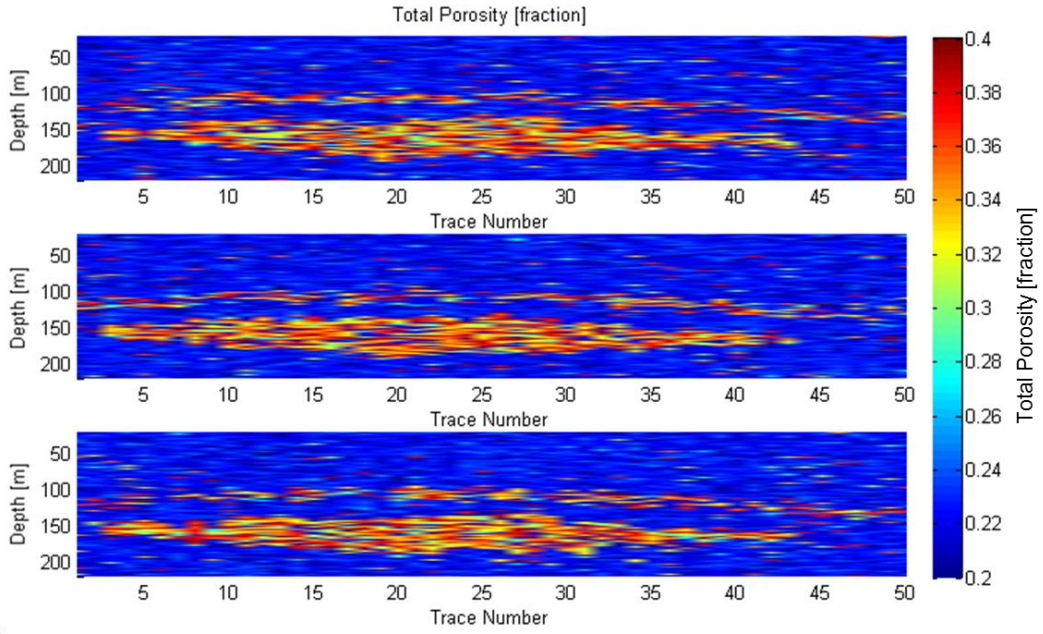

Figure 7.5: Three possible stochastic total porosity models.

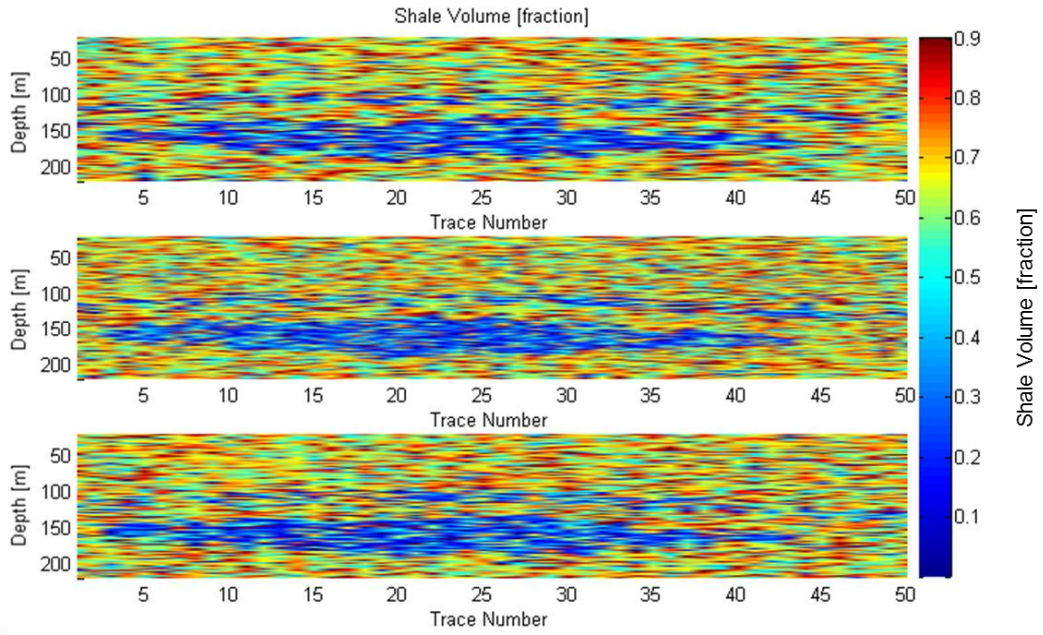

Figure 7.6: Three possible stochastic volume of shale models.

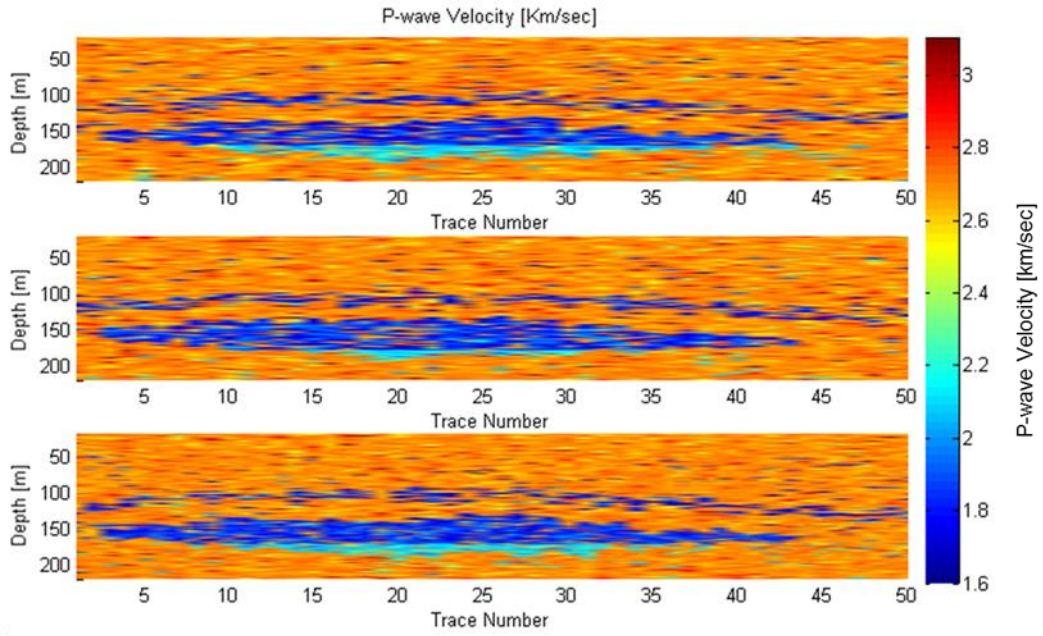

Figure 7.7: Three possible stochastic P-wave impedance models.

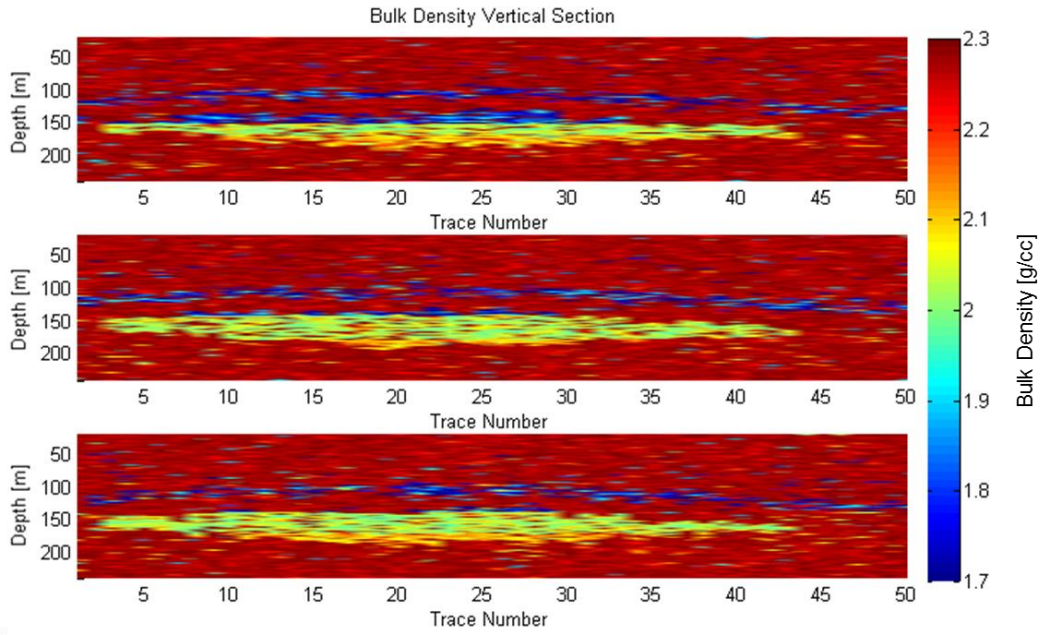

Figure 7.8: Three possible stochastic bulk density models.

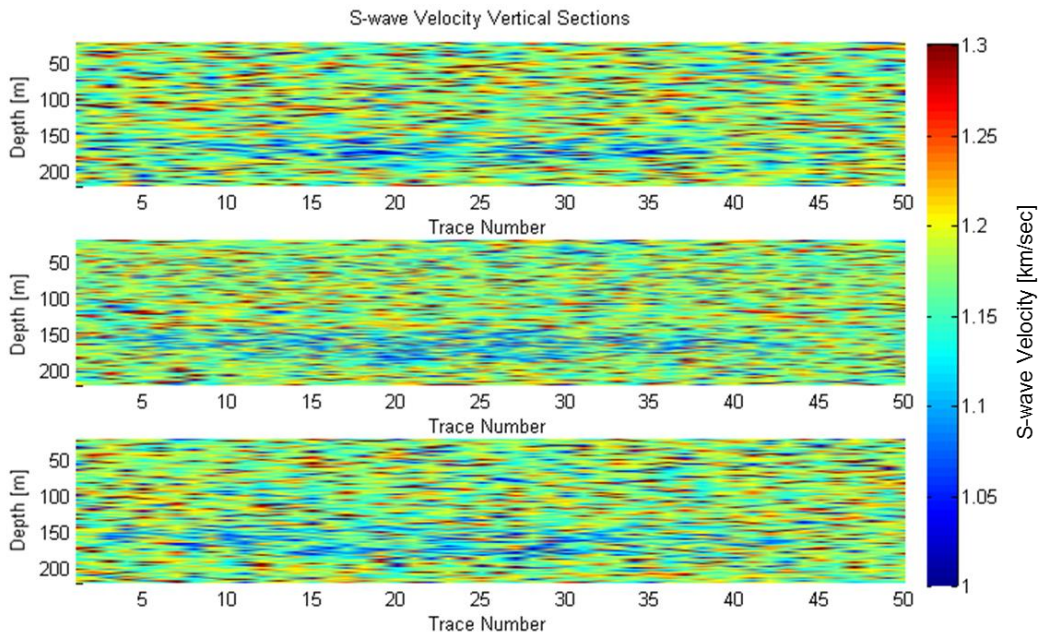

Figure 7.9: Three possible stochastic S-wave velocity models.

A set of four hundred possible outcomes was generated from the seismic section. This set of seismic inversions was used to calculate the most expecting values of the estimated rock properties for each sample of the 2D seismic section. As it is expected, these inverted rock property sections were smoother versions of the original inverted outcomes.

Additionally, we generated the variance section for each rock property inverted vertical section. The variance sections were used to better understand the uncertainty associated with the inversion outcomes. Figure 7.10 shows the most expected section of total porosity (upper section) and its associated variance (lower section). Well-1 measured total porosity log is located in the trace number 37. It can be observed that there is good agreement between the measured data and the inverted section. However, Well-1 has a larger vertical

resolution than the inverted traces. As we observed in Chapter 6, the median of the stochastic inversion outcomes tends to slightly underestimate larger porosity values and overestimate lower porosity values. The variance section shows that the upper gas sand has larger estimation uncertainty. This is due to the interbedded gas-shale geometry of the upper sand. The zero variance trace corresponds to the Well-1 location. The same phenomenon is observed in all the rock property vertical sections; the upper sand has larger estimation errors than the lower sand (Figures 7.11 to 7.14). In the bulk density inverted section (Figure 7.13) the variance of the upper sand and the lower sand gas intervals has larger estimation errors than those of the LSGS and brine sand. This is caused by the low predictability of the gas sands and LSGS fluid contact.

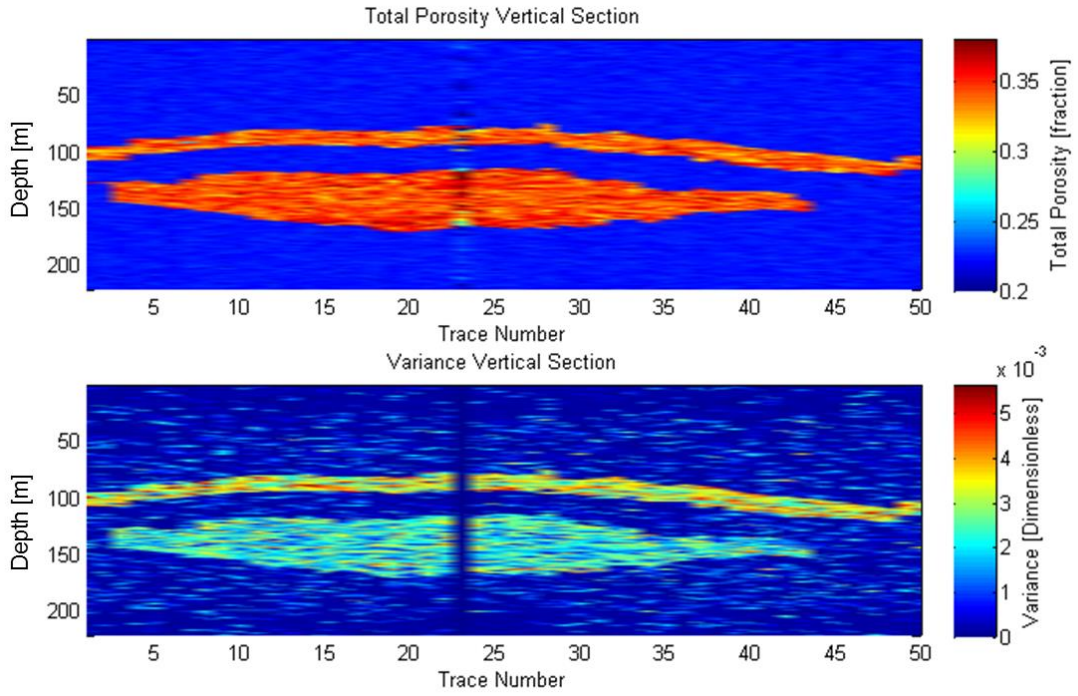

Figure 7.10: Most expected total porosity model generated from 400 stochastic models.

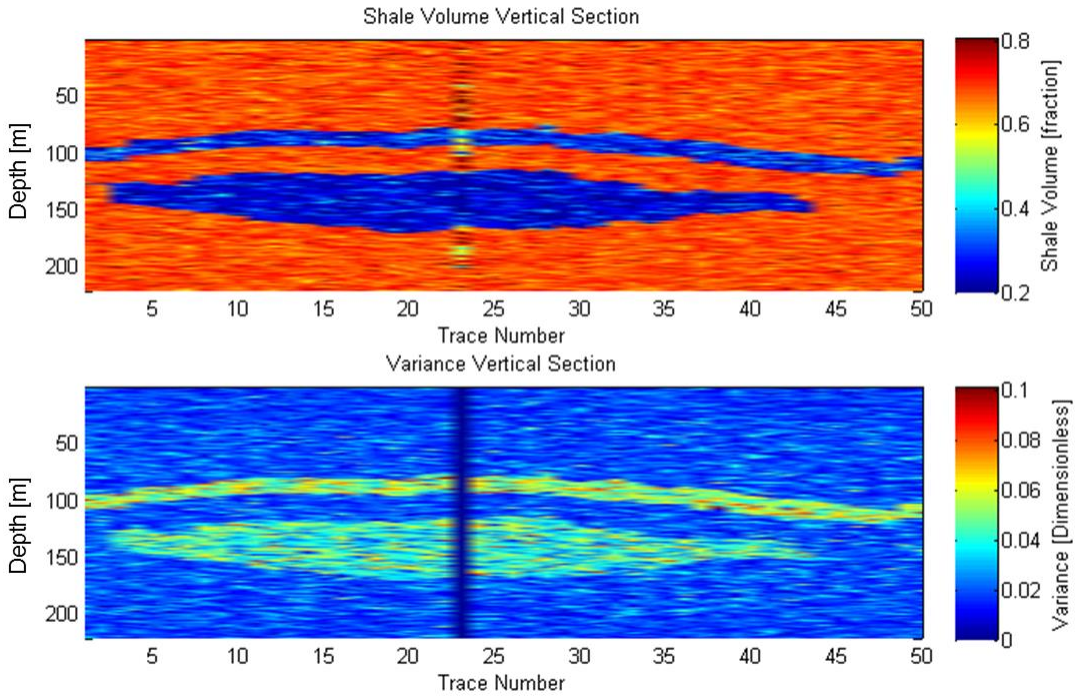

Figure 7.11: Most expected volume of shale model generated from 400 stochastic models.

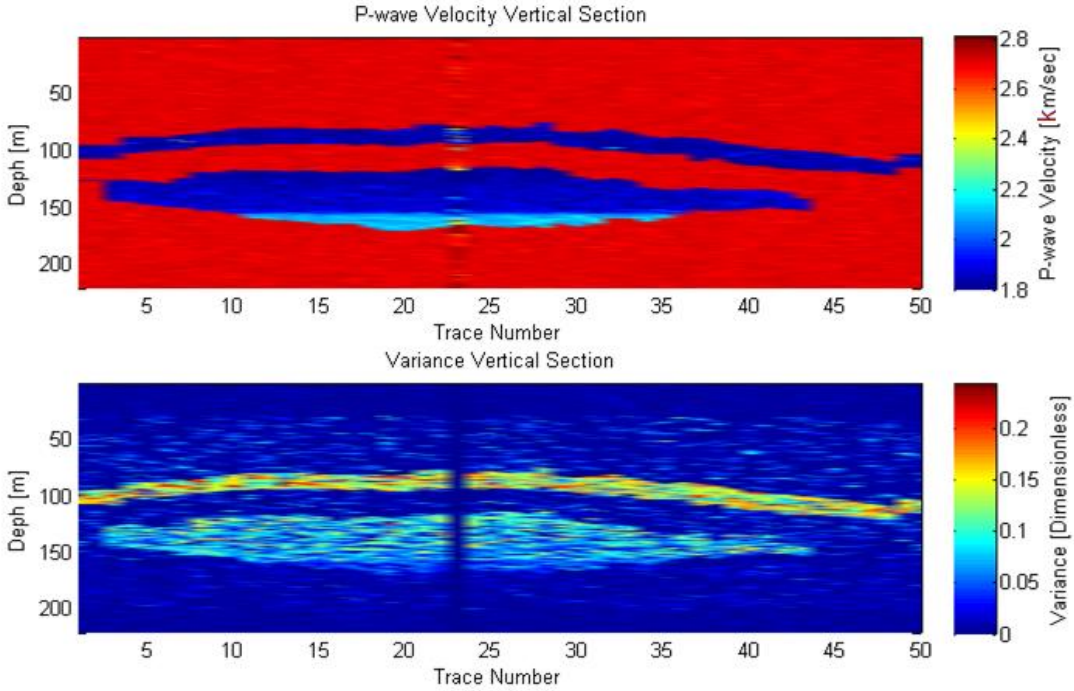

Figure 7.12: Most expected volume of P-wave velocity generated from 400 stochastic models.

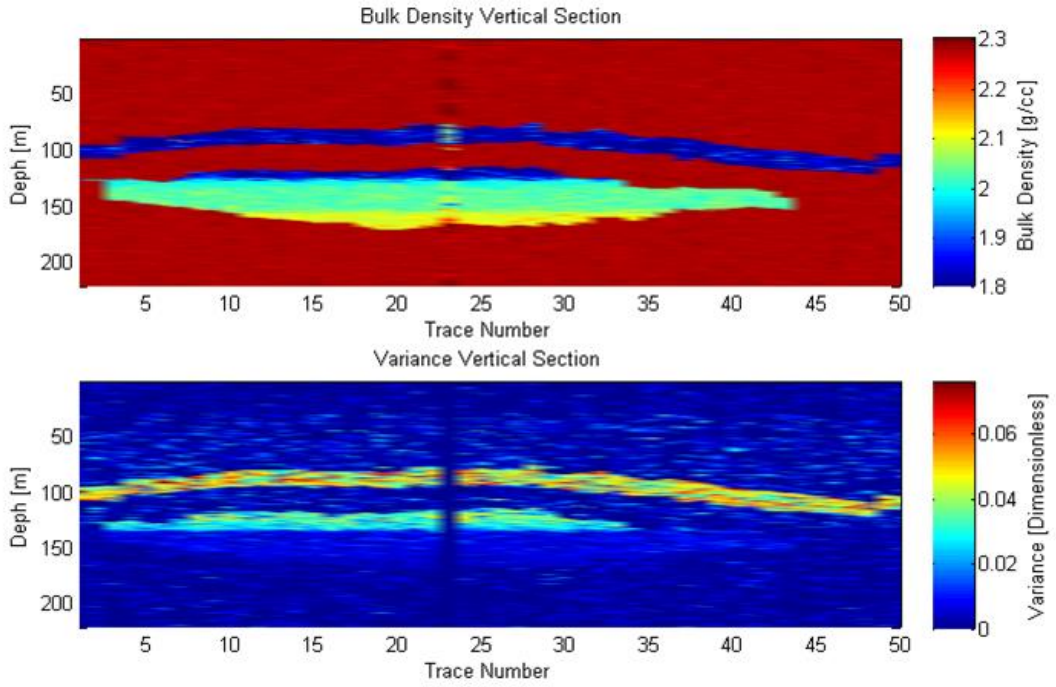

Figure 7.13: Most expected volume of density generated from 400 stochastic models.

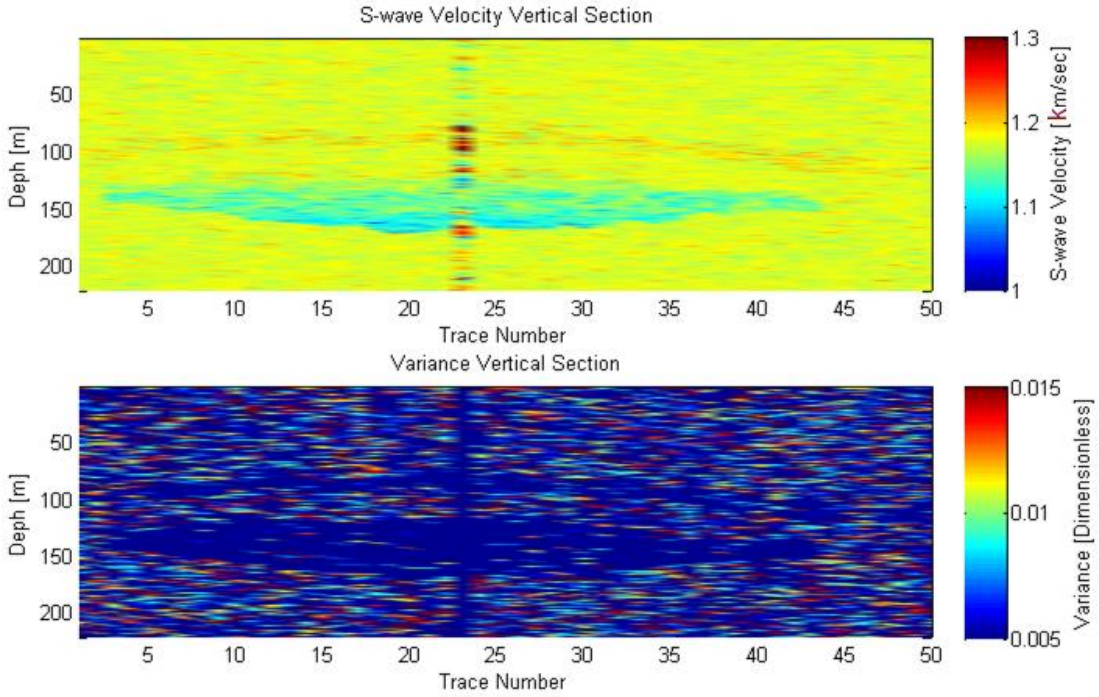

Figure 7.14: Most expected volume of S-wave velocity generated from 400 stochastic models.

7.4. Convergence Criteria

A critical parameter for the proposed stochastic inversion execution is the misfit threshold α. For this real data application we chose the L^2-norm value obtained from the synthetic tie as value of α. This selection was based on the idea that the forward model operator is imperfect and cannot perfectly reproduce real seismic data. Other sources of misfits, besides the forward modeling operator, come from imperfections in the seismic data acquisition/processing and deficiencies in the time-to-depth conversion model. It is important to point out that the smaller α becomes, the more realizations are needed to obtain a statistically significant number of probable models. Figure 7.15 shows 150,000 models randomly selected from the five million realizations performed for the real example inversion. It can be observed that only a few hundreds models look like the studied real data set inverted.

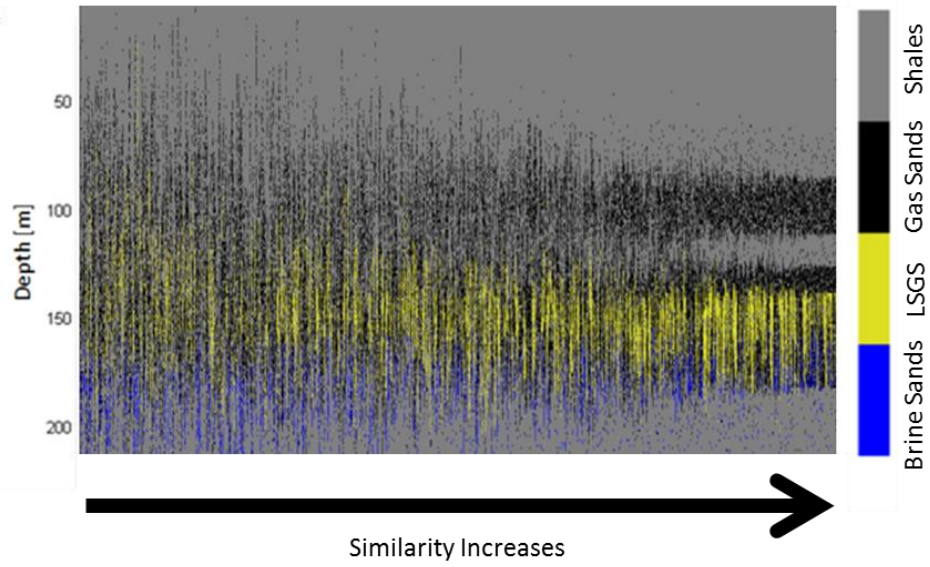

Figure 7.15: Models randomly selected from the real dataset inversion.

The synthetic traces generated from the models shown in Figure 7.15 are shown in Figure 7.16. For other shown models, the calculated seismic traces are very noisy, without recognizable seismic interfaces. For the 150,000 traces shown in Figure 7.16, only nine were selected as probable solutions. The selection of α value smaller than the similarity obtained from the well log tie would have deteriorated the inversion outcome, because the possible solutions would have been generated from a partially sampled model space.

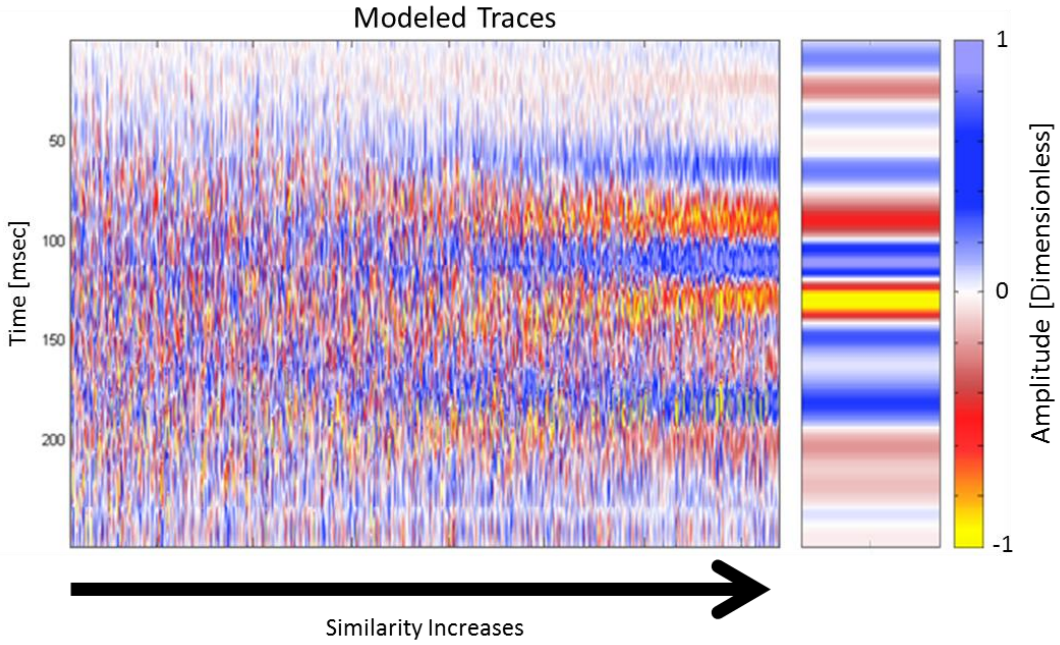

Figure 7.16: Comparison between real angle trace (right) and 150,000 solutions (left) randomly selected from the five million realizations performed for the real example inversion.

7.5. Algorithm Efficiency

The proposed algorithm was extensively tested in a Windows based personal computer with two processors and eight cores. The results showed that the amount of resources (computing time) needed by the our proposed algorithm increase linearly (O(n)) with the number of tested models. The average running time is 269 models/sec.

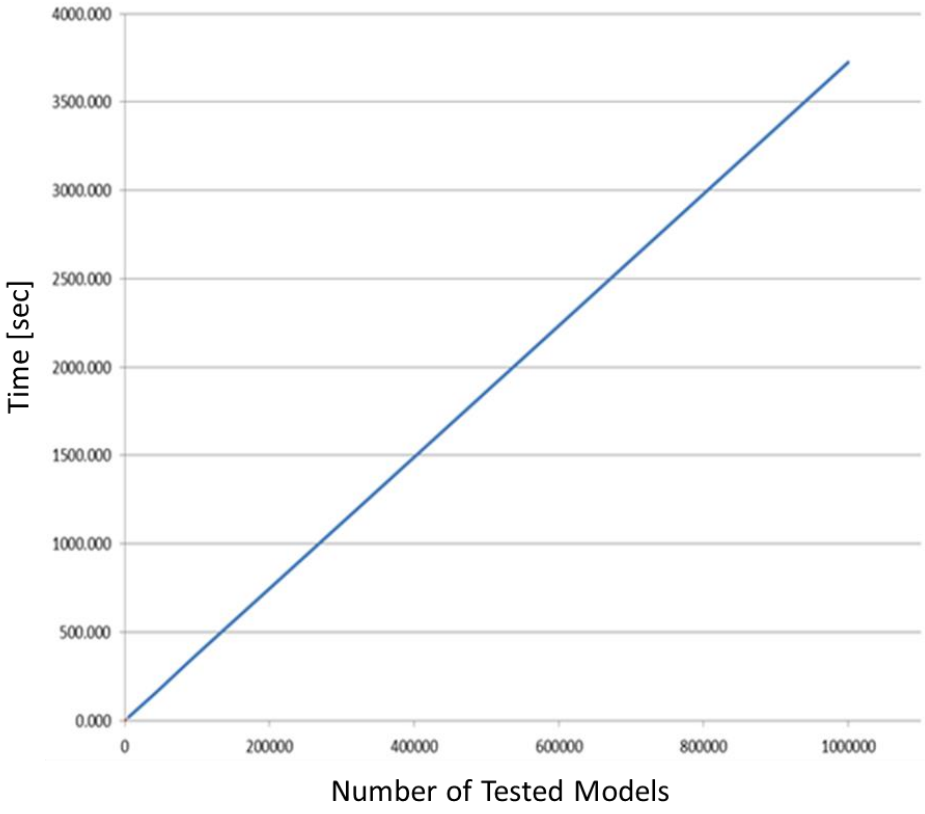

Figure 7.17: Algorithm efficiency, the proposed algorithm increase linearly with the number of tested models.

6.7. Conclusions

The applicability of our proposed 3D stochastic inversion algorithm to real case studies was demonstrated. The outcome of the inversion was a set of key rock property sections that can be directly used for the evaluation of the hydrocarbon potential of a given the inverted subsurface interval. Moreover, the inversion solutions were generated directly in the depth domain. Therefore, with our solutions, no time-to-depth is needed during the inversion process.

Results of the 3D inversion showed good vertical resolution and adequate lateral continuity. As we observed in the 1D real data application, the real data test of the 3D stochastic inversion shows a remarkable similarity to the available well log data. However, the median of the inverted traces has lower vertical variability than the Well-1 logs. Larger estimation errors were found in the upper gas sand, due to its interbedded geometry.

The real-data tests showed that the similarity factor α is the most sensible parameter in the proposed inversion algorithm. The selection of α value smaller than the similarity obtained from the well log tie will deteriorate the inversion outcome, since the possible solutions will be generated from a partially sampled model space.

REFERENCES

Aki, K., and Richards, P. G., 1980, Quantitative seismology: theory and methods: W. N. Treeman & Co. pp. 119-149.

Arpat, B. G., 2005, Sequential simulation with patterns: Ph.D. dissertation, Stanford Univ. pp. 7-11.

Avseth, P., 2000, Combining rock physics and sedimentology for seismic reservoir characterization in North Sea turbidite systems: Ph.D. dissertation, Stanford Univ. pp. 14-49.

Avseth, P., Mukerji, T., and Mavko, G., 2005, Quantitative seismic interpretation: applying rock physics tools to reduce interpretation risk: Cambridge University Press. pp. 42-47.

Backus, G. E., 1962, Long-wave elastic anisotropy produced by horizontal layering: J. Geophys. Res., 67, 4427-4440.

Balch, A. H., 1971, Color sonagrams - A new dimension in seismic data interpretation: Geophysics, 36, 1074-1098.

Banchs, R. and Michelena, R., 2000, Well log estimates and confidence intervals by using artificial neural networks: 70th Ann. Internat. Mtg,. Soc. of Expl. Geophys., Expanded Abstracts, 1430-1432.

Batzle, M., and Wang., Z., 1992, Seismic properties of pore fluids: Geophysics, 57, 1396-1408.

Berryman, J. G., Berge, P. A., Bonner, B. P., 2002, Estimating rock porosity and fluid saturation using only seismic velocities: Geophysics, 67, 391-404.

Bortoli, L. J., Alabert, F. A., Haas, A., and Journel, A. G., 1993, Constraining Stochastic Images to Seismic Data, in A. Soares ed., Geostatistics Tróia 1992, proc. 4th Inter. Geostat. Congr., Kluwer Academic Publ., 325-337.

Bosch, M., 1999, Lithologic tomography: From plural geophysical data to lithology estimation: Journal of Geophysical Research, 104, 749–766.

Castagna, J. P., Batzle, M. L., and Eastwood, R. L., 1985, Relationships between compressional-wave and shear-wave velocities in clastic silicate rocks: Geophysics, 50, 571-581.

Castagna, J. P., Batzle, M. L., and Kan, T. K., 1993, Rock physics – The link between rock properties and AVO response, in J. P. Castagna and M. Backus, eds., Offset-dependent reflectivity – Theory and practice of AVO analysis: Soc. of Expl. Geophys., 135-171.

Connolly, P., 1998, Calibration and inversion of non-zero offset seismic: 68th Ann. Internat. Mtg,. Soc. of Expl. Geophys., Expanded Abstracts, 182-184.

Connolly, P., 1999, Elastic impedance: The Leading Edge, 18, 438-452.

Deutsch C., and Journel, A., 1998, GSLIB: Geostatistical Software Library: Oxford University Press, 2nd edition.

Domenico, S. N., 1976, Effect of brine-gas mixture on velocity in an unconsolidated sand reservoir: Geophysics, 41, 882-894.

Dvorkin, J., and Nur, A., 1996, Elasticity of High-Porosity Sandstones: Theory for Two North Sea Datasets, Geophysics, 61, 1363-1370.

Dvorkin, J., Nur, A., and Yin, H., 1994, Effective Properties of Cemented Granular Materials, Mechanics of Materials, 18, 351-366.

Fisher, A., Yates, F., 1948, Statistical tables for biological, agricultural and medical research: Oliver & Boyd. Pp. 26-27.

Florez, J., 2005, Integrating geology, rock physics, and seismology for reservoir quality prediction: Ph.D. dissertation, Stanford Univ. pp. 13-44.

Gardner, G., Gardner, L., and Gregory, A., 1974, Formation velocity and density – The diagnostic basic for stratigraphic traps: Geophysics, 39, 770-780.

Gassmann, F., 1951, Über die elastizität poröser medien: Veirteljahrsschrift der Naturforschenden Gesellschaft in Zürich, 96, 1-23.

Gonzalez, E. F., Mukerji, T. and Mavko, G., 2000, Facies identification using P-to-P and P-to-S AVO attributes: 70th Ann. Internat. Mtg,. Soc. of Expl. Geophys., Expanded Abstracts, 98-101.

Gonzalez, E., 2006, Physical and quantitative Interpretation of seismic attributes for rock and fluid interpretation: Ph.D. dissertation, Stanford Univ. pp. 49-78.

Goodway, B., Chen, T. and Downton, J., 1997, Improved AVO fluid detection and lithology discrimination using Lame petrophysical parameters; “λρ”, “μρ”, & “λ/μ

fluid stack", from P and S inversions: 67th Ann. Internat. Mtg,. Soc. of Expl. Geophys., Expanded Abstracts, 183-186.

Grechka, V., 2008, Fluid substitution in porous and fractured solids: The non-interaction approximation and Gassmann theory: International Journal of Fracture, 148, 103-107.

Gray, D., 2002, Elastic inversion for Lamé parameters: 72th Ann. Internat. Mtg,. Soc. of Expl. Geophys., Expanded Abstracts, 213-216.

Greenberg, M. L., and Castagna, J.P., 1992, Shear-wave velocity estimation in porous rocks: Theoretical formulation, preliminary verification and applications, Geophys. Prospect., 40, 195-209.

Guardiano, F., and Srivastava, R., 1993, Multivariate geostatistics: Beyond bivariate moments, in A. Soares ed., Geostatistics Tróia 1992, proc. 4th Inter. Geostat.Congr., Kluwer Academic Publ., 133-144.

Gutierrez, M., 2001, Rock physics and 3-D seismic characterization of reservoir heterogeneities to improve recovery efficiency: Ph.D. dissertation, Stanford Univ.

Haas, A. and Dubrule, O., 1994, Geostatistical inversion - A sequential method of stochastic reservoir modeling constrained by seismic data: First Break, 12, 561-569.

Han, D., 1986, Effects of porosity and clay content on acoustic properties of sandstones and unconsolidated sediments: Ph.D. thesis, Stanford University.

Harris, D. A., Lewis, J. J. M., and Wallace, D. J., 1993, The identification of lithofacies types in geological imagery using neural networks, Conf. papers vol., EUROCAIPEP 93, Aberdeen.

Hashin, Z., and Shtrikman, S., 1963, A variational approach to the elastic behavior of multiphase materials: J. Mech. Phys. Solids, 11, 127-140.

Hastings, W.K., 1970, Monte Carlo sampling methods using Markov Chains and their applications: Biometrika, 57, 97–109.

Hearst, J. R., Nelson, P. H., Pailet, F. L., 2000, Well logging for physical properties: McGraw-Hill, 2nd edition.

Hirsche, K., Boerner, S., Kalkomey, C. and Gastaldi, C., 1998, Avoiding pitfalls in geostatistical reservoir characterization: A survival guide: The Leading Edge, 17, 493-504.

Isaaks, E., and Srivastava, R., 1989, An introduction to applied geostatistics: Oxford University Press. pp. 278-322.

Kalkomey, C. T., 1997, Potential risks when using seismic attributes as predictors of reservoir properties: The Leading Edge, 16, 247-251.

Landrø, M., 1999, Discrimination between pressure and fluid saturation changes from time lapse seismic data, 69th Ann. Int. Meet., Soc. Expl. Geophys., Expanded Abstracts, 1651-1654.

Mallick, S., 2001, Hybrid inversion, elastic impedance inversion, and prestack waveform inversion; 71st Ann. Internat. Mtg: Soc. of Expl. Geophys., 706-709. Marion, D., 1990, Acoustical, mechanical and transport properties of sediments and granular materials: Ph.D. thesis, Stanford University.

Matteucci, G., 1996, Seismic attribute analysis and calibration: A general procedure and a case study: 66th Ann. Internat. Mtg,. Soc. of Expl. Geophys., Expanded Abstracts, 373-376.

Mavko, G., and Jizba, D., 1991, Estimation grain-scale fluid effects on velocity dispersion in rocks: Geophysics, 56, 1940-1949.

Mavko, G., Mukerji, T., and Dvorkin, J., 1998, The rock physics handbook: Cambridge University Press.

Metropolis, N., Rosenbluth, A.W., Rosenbluth, M.N., Teller, A.H., Teller, E., 1953, Equations of state calculations by fast computing machines: Journal of Chemical Physics, 21, 6, 1087–1092.

Mukerji, T., Jørstad, A., Mavko, G., and Granli, J., 1998, Near and far offset impedances: Seismic attributes for identifying lithofacies and pore fluids: Geophysical Research Letter, 25, 4557-4560.

Mukerji, T., Avseth, P., Mavko, G, Takahashi, I., and Gonzalez, E. F., 2001, Statistical rock physics: Combining rock physics, information theory, and geostatistics to reduce uncertainty in seismic reservoir characterization: The Leading Edge, 20, 313-319.

Oldenburg, D. W., Scheuer, T., and Levy, S., 1983, Recovery of the acoustic impedance from reflection seismograms: Geophysics, 48, 1318-1337.

Ostrander, W. J., 1984, Plane-wave reflection coefficients for gas sands at non-normal angles of incidence: Geophysics, 49, 1637-1648.

Papoulis, A., 1984, Probability, random variables, and stochastic processes: McGraw-Hill.

Possato, S., Saito, M., Curtis, M. P., and Martinez, R. D., 1983, Interpretation of three-dimensional seismic attributes contributes to stratigraphic analysis of Pampo oil field: 53rd Ann. Internat. Mtg,. Soc. of Expl. Geophys., Expanded Abstracts, session: S16.2.

Raymer, L. L., E. R. Hunt, and J. S. Gardner, 1980, An improved sonic transit time-to-porosity transform: 21st Annual Logging Symposium Transaction, Society of Professional Well Log Analysts, Paper P.

Ruiz, F., 2009, Porous grain model and equivalent elastic medium approach for predicting effective elastic properties of sedimentary rocks: Ph.D. dissertation, Stanford Univ.

Russell, B. H., 1988, Introduction to seismic inversion methods: Soc. of Expl. Geophys. Course notes from SEG Continuing Education course.

Sengupta, M., 2000, Integrating rock physics and flow simulation to reduce uncertainties in seismic reservoir monitoring: Ph.D. dissertation, Stanford Univ.

Shuey, R. T., 1985, A simplification of the Zoeppritz equations: Geophysics, 50, 609-614.

Sheriff, R., 1989, Geophysical Methods: Prentice Hall.

Takahashi, I., 2000, Quantifying information and uncertainty of rock property estimation from seismic data: Ph.D. dissertation, Stanford Univ.

Taner, M. T., Koehler, F., and Sheriff, R. E., 1979, Complex seismic trace analysis: Geophysics, 44, 1041-1063.

Tarantola, A., 2005, Inverse problem theory and methods for model parameter estimation: Society for Industrial and Applied Mathematics.

Thomsen, L., 1985, Biot-consistent elastic moduli of porous rocks: Low-frequency limit: Geophysics, 50, 2797-2807.

Tonn, R., 1992, Statistical approach to correlate reservoir parameters and 3-D seismic attributes, 62nd Ann. Internat. Mtg,. Soc. of Expl. Geophys., Expanded Abstracts, 272-274.

Wu, Y., 2000, Estimation of gas saturation using P-to-S converted waves; 70th Ann. Internat. Mtg,. Soc. of Expl. Geophys., Expanded Abstracts, 158-161.

Wyllie, M. R., Gregory, A. R., and Gardner, L. W., 1956: Elastic wave velocities in heterogeneous and porous media, Geophysics, 21, 41-70.

Yin, H., Mavko, G., and Nur, A., 1993, Critical porosity; a physical boundary in poroelasticity: 34th U. S. symposium on Rock mechanics, in Haimson, B. C., ed., Rock mechanics in the 1990s, Oxford-New York, International Journal of Rock Mechanics and Mining Sciences & Geomechanics, Abstracts, 30, 805-808.

Zeng, H., Backus, M. M., Barrow, K. T. and Tyler, N., 1996, Facies mapping from three-dimensional seismic data: Potential and guidelines from a Tertiary sandstone-shale sequence model, Powderhorn Field, Calhoun County, Texas: AAPG Bull., 80, 16-46.